

DESIGN OF A WIDEBAND BEAM SCANNING ROTMAN LENS ARRAY

A THESIS SUBMITTED TO
THE GRADUATE SCHOOL OF NATURAL AND APPLIED SCIENCES
OF
MIDDLE EAST TECHNICAL UNIVERSITY

BY

DAMLA DUYGU TEKBAŞ

IN PARTIAL FULFILLMENT OF THE REQUIREMENTS
FOR
THE DEGREE OF MASTER OF SCIENCE
IN
ELECTRICAL AND ELECTRONICS ENGINEERING

DECEMBER 2012

Approval of the thesis:

DESIGN OF A WIDEBAND BEAM SCANNING ROTMAN LENS ARRAY

submitted by **DAMLA DUYGU TEKBAS** in partial fulfillment of the requirements for the degree of **Master of Science in Electrical and Electronics Engineering Department, Middle East Technical University** by,

Prof. Dr. Canan Özgen
Dean, Graduate School of **Natural and Applied Sciences**

Prof. Dr. İsmet Erkmen
Head of Department, **Electrical and Electronics Engineering**

Prof. Dr. M. Tuncay Birand
Supervisor, **Electrical and Electronics Engineering Dept., METU**

Examining Committee Members:

Prof. Dr. Gülbilin Dural
Electrical and Electronics Engineering Dept., METU

Prof. Dr. M. Tuncay Birand
Electrical and Electronics Engineering Dept., METU

Assoc. Prof. Dr. Şimşek Demir
Electrical and Electronics Engineering Dept., METU

Assoc. Prof. Dr. Lale Alatan
Electrical and Electronics Engineering Dept., METU

M. Erim İnal, M. Sc.
Manager, ASELSAN

Date: 11/12/2012

I hereby declare that all information in this document has been obtained and presented in accordance with academic rules and ethical conduct. I also declare that, as required by these rules and conduct, I have fully cited and referenced all material and results that are not original to this work.

Name, Last name : Damla Duygu TEKBAS

Signature :

ABSTRACT

DESIGN OF A WIDEBAND BEAM SCANNING ROTMAN LENS ARRAY

Tekbaş, Damla Duygu

M. Sc., Department of Electrical and Electronics Engineering

Supervisor: Prof. Dr. M. Tuncay Birand

December 2012, 106 pages

The design, manufacturing techniques and measurements for wideband Rotman lens are presented. Different design approaches are explained in detail. A step-by-step procedure followed through the design process of a Rotman lens is given. The design equations are derived for both the parallel-plate/waveguide and microstrip/stripline Rotman lens versions. Effects of the design parameters on the lens shape and performance are investigated. A microstrip Rotman lens operating in 8 GHz – 16 GHz frequency band is designed and manufactured. To this end, related theoretical and simulation studies are carried out. The measurement results are compared with the results of the simulation studies.

Keywords: Rotman lens, microstrip Rotman lens, beamforming network, phased array.

ÖZ

GENİŞ BANTLI ROTMAN LENS DİZİSİ TASARIMI

Tekbaş, Damla Duygu

Yüksek Lisans, Elektrik ve Elektronik Mühendisliği Bölümü

Tez Yöneticisi: Prof. Dr. M. Tuncay Birand

Aralık 2012, 106 sayfa

Geniş bantlı Rotman lens tasarımı, üretimi ve ölçümleri sunulmaktadır. Farklı tasarım yaklaşımları detaylı bir şekilde açıklanmaktadır. Rotman lens tasarımda izlenmesi gereken adımlar anlatılmaktadır. Hem paralel-plaka/dalga kılavuzu hem de mikroşerit/şerit hat Rotman lens tasarımı için tasarım denklemleri çıkartılmaktadır. Tasarım değişkenlerinin, lens şekline ve performansına etkileri incelenmektedir. 8 GHz – 16 GHz bandında çalışan mikroşerit Rotman lens tasarlanmakta ve gerçeklenen yapının üzerinde ilgili teorik ve benzetim çalışmaları yapılmaktadır. Son olarak, tasarlanan lens yapısı üretilmekte, ölçülmemekte ve ölçüm sonuçları benzetim sonuçlarıyla karşılaştırılmaktadır.

Anahtar kelimeler: Rotman lens, mikroşerit Rotman lens, huzme oluşturan devre, faz taramalı dizi.

To My Mother, Sister and Orhy

ACKNOWLEDGEMENTS

I would like to express my sincere gratitude to my supervisor Prof. Dr. M. Tuncay Birand for his guidance, patience and help. I would also like to thank Prof Dr. Gülbün Dural, Assoc. Prof Dr. Şimşek Demir, Assoc. Prof. Dr. Lale Alatan and M. Erim İnal for being in my jury and expressing their very useful comments and suggestions.

Firstly, I would like to express my greatest thanks to my mother, Selma Tekbaş and my sister, Umay Tekbaş for their care, support and patience throughout my studies. Besides, I would like to express my sincere gratitude to my fiancé, Orhan Geçen for being in my life with his never-ending love, support and understanding.

At the writing period of the thesis, I could not deny the support of my colleagues. I want to thank them all for encouraging me to complete this thesis. Firstly, I want to thank Egemen Yıldırım and Kadir İşeri for their helpful behaviors and for sharing their point of views with me. Also, I would like to thank Görkem Akgül and Ozan Gerger for their help.

Finally, I wish to express my appreciation to ASELSAN Inc. for all facilities provided. Especially, I am very grateful for the support during the manufacture and measurement stages in this thesis.

TABLE OF CONTENTS

ABSTRACT	iv
ÖZ	v
ACKNOWLEDGEMENTS	vii
TABLE OF CONTENTS	viii
LIST OF TABLES	xi
TABLES	xi
LIST OF FIGURES	xii
FIGURES	xii
1. INTRODUCTION	1
1.1 Beamformers	1
1.1.1 Network Beamformers	2
1.1.1 Digital Beamformers	3
1.1.3 Microwave Lens Beamformers	4
1.2 Rotman Lens	5
1.2.1 Rotman Lens Applications	7
1.3 Objective of the Thesis	9
1.4 Thesis Outline	9
2. ROTMAN LENS DESIGN PROCEDURE	11
2.1 Design Approaches	11

2.1.1 Rotman's Approach (The Conventional Design)	11
2.1.2 Shelton's Approach (Symmetrical Lens)	12
2.1.3 Katagi's Approach (An Improved Design Method)	13
2.1.4 Gagnon's Approach (Refocusing)	14
2.1.5 Hansen's Approach (Design Trades).....	14
2.2 Derivation of the Design Equations	14
2.2.1 Design Equations for Parallel-Plate/Waveguide Rotman Lenses.....	15
2.2.2 Design Equations for Microstrip/Stripline Rotman Lenses.....	21
2.3 Optical Aberrations.....	26
2.3.1 Path Length Error for Parallel-Plate/Waveguide Rotman Lens	27
2.3.2 Path Length Error for Microstrip/Stripline Rotman Lens	28
2.4 MATLAB [®] Script	28
3. PARAMETRIC STUDY ON DESIGN PARAMETERS	30
3.1 Focal Ratio – g	31
3.2 Normalized Array Aperture – $2 \times n_{max}$	33
3.3 Eccentricity Parameter – e	36
3.4 Relative Dielectric Constant of the Substrate – ϵ_r	39
3.5 Maximum Scan Angle (Off-Center Focal Angle) – α	42
3.6 Off-Axis Focal Length – F	45
4. IMPLEMENTATION AND SIMULATION RESULTS	48
4.1 Microstrip Rotman Lens Implementation.....	48
4.1.1 Selection of the Dielectric Substrate	49
4.1.2 Choice of Design Parameters	51
4.1.3 Microstrip Matching	52
4.1.4 Port Pointing.....	55
4.1.5 Sidewall Design.....	55

4.1.6 Transmission Line Length Arrangement	56
4.1.7 Implemented Model.....	57
4.2 Simulation Results	58
4.2.1 Return Loss Performance	59
4.2.2 Coupling between Ports.....	60
4.2.3 Amplitude and Phase Distributions over the Array Elements.....	63
4.2.4 Array Factor Calculations.....	67
5. PRODUCTION AND MEASUREMENT RESULTS	72
5.1 Production Process.....	72
5.2 Measurements	73
5.2.1 Network Analyzer Measurements	73
5.2.2 Antenna Measurements	91
6. CONCLUSIONS.....	99
REFERENCES	101
APPENDIX.....	105
A. CALCULATION OF THE EFFECTIVE DIELECTRIC CONSTANT OF A MICROSTRIP TRANSMISSION LINE	105

LIST OF TABLES

TABLES

Table 2 - 1: Description of the Design Parameters	16
Table 3 - 1: Chosen Design Parameters to Observe "g" Effects	32
Table 3 - 2: Chosen Design Parameters to Observe " n_{max} " Effects	33
Table 3 - 3: Optimum g & dlmax for Different " n_{max} "	34
Table 3 - 4: Optimum g & e Pair and dl for Different " n_{max} "	37
Table 3 - 5: Values of " ϵ_r " & " ϵ_{re} " for the Chosen Substrates	40
Table 3 - 6: Optimum g&e Pair and dl for Different " ϵ_r "	40
Table 3 - 7: Optimum g&e Pair and dl for Different " α "	43
Table 3 - 8: Optimum g Calculated from the Ruze's [5] Equation (3.1).....	43
Table 4 - 1: Design Requirements	49
Table 4 - 2: Properties of Several Dielectric Materials.....	50
Table 4 - 3: Chosen Design Parameters	52
Table 4 - 4: Calculated Beam Peak Angles of the Array Factor.....	70
Table 4 - 5: Calculated 3dB Beamwidths of the Array Factor	71
Table 4 - 6: Calculated First Sidelobe Levels of the Array Factor	71
Table 5 - 1: Peak Angles of the Simulated and Measured Array Factors.....	88
Table 5 - 2: 3 dB Beamwidths of the Simulated and Measured Array Factors	89
Table 5 - 3: First Sidelobe Levels of the Simulated and Measured Array Factors...	90
Table 5 - 4: Peak Angles of the Simulated and Measured Patterns	97
Table 5 - 5: 3 dB Beamwidths of the Simulated and Measured Patterns	98
Table 5 - 6: Fist Sidelobe Levels of the Simulated and Measured Patterns	98

LIST OF FIGURES

FIGURES

Figure 1 - 1: Beamformer Schematic.....	2
Figure 1 - 2: Digital Beamformer Topology.....	3
Figure 1 - 3: Microwave Lens BFN.....	4
Figure 1 - 4: Reduced Lens Size by Dielectric Loading (From [6]).....	6
Figure 1 - 5: First 2D Rotman Lens Stack Feeding Planar (From [6]).....	6
Figure 1 - 6: Rotman Lens Used Marine & Airborne Radars by Raytheon (From [9]): (a) AN/SLQ-32(V); (b) AN/ALQ-184	7
Figure 1 - 7: (a) Rotman Lens used as a Phase Processor; (b) Example Image [11]..	8
Figure 2 - 1: Microwave Lens Parameters (From [3]).....	11
Figure 2 - 2: Symmetrical Lens Configuration (From [15])	12
Figure 2 - 3: Katagi's Model for Rotman Lens Design (From [16])	13
Figure 2 - 4: Rotman Lens Design Parameters	15
Figure 2 - 5: Elliptic Beam Contour Parameters.....	20
Figure 2 - 6: Microstrip/Stripline Rotman Lens Design Parameters	22
Figure 3 - 1: Lens & Beam Contour Variations with g.....	31
Figure 3 - 2: Phase-Error Variation with g	33
Figure 3 - 3: Optimum g vs. n_{max} Plot.....	35
Figure 3 - 4: Phase-Error Variation with n_{max} for Optimum g.....	35
Figure 3 - 5: Lens & Beam Contour Variations with n_{max} for optimum g.....	36
Figure 3 - 6: Optimum g & e Pair vs. n_{max} Plot	37
Figure 3 - 7: Phase-Error Variation with g & e for $n_{max}=0.5$	38

Figure 3 - 8: Phase-Error Variation with e for Different g	38
Figure 3 - 9: Optimum g & e Pair vs. ϵ_r Plot	40
Figure 3 - 10: Phase-Error Variation with ϵ_r for Optimum g & e	41
Figure 3 - 11: Lens & Beam Contour Variations with ϵ_r for Optimum g & e	42
Figure 3 - 12: Optimum g vs. α Plot	44
Figure 3 - 13: Phase-Error Variation with α for optimum g & e	44
Figure 3 - 14: Lens & Beam Contour Variations with α for Optimum g & e	45
Figure 3 - 15: Sketch of the Antenna Array.....	46
Figure 4 - 1: Frequency Response of Different Dielectric Materials (From [20])....	50
Figure 4 - 2: Matching Section with Microstrip Linear Taper.....	53
Figure 4 - 3: $S_{11\max}$ vs. Taper Angle Plot for the Microstrip Linear Taper.....	53
Figure 4 - 4: Locations of the Phase Centers	54
Figure 4 - 5: Beam & Array Ports' Allocation	55
Figure 4 - 6: Sidewall Interference	56
Figure 4 - 7: Line Bendings Implemented in ADS	57
Figure 4 - 8: Implemented Microstrip Rotman Lens Model.....	58
Figure 4 - 9: Return Loss of the Beam Ports	59
Figure 4 - 10: Return Loss of the Array Ports	59
Figure 4 - 11: Coupling between the Beam Ports	60
Figure 4 - 12: Coupling between the Two Adjacent Beam Ports	60
Figure 4 - 13: Coupling between the Array Ports	61
Figure 4 - 14: Coupling between the Two Adjacent Array Ports	62
Figure 4 - 15: Coupling between B0 and the Dummy Ports.....	62
Figure 4 - 16: Coupling between A6 and the Dummy Ports.....	63
Figure 4 - 17: Amplitude Distribution over Antennas excited from B0	64
Figure 4 - 18: Amplitude Distribution over Antennas excited from B15	64
Figure 4 - 19: Amplitude Distribution over Antennas excited from B30	65
Figure 4 - 20: Phase Distribution over Antennas excited from B0	66
Figure 4 - 21: Phase Distribution over Antennas excited from B15	66

Figure 4 - 22: Phase Distribution over Antennas excited from B30.....	67
Figure 4 - 23: Array Placement According to the Coordinate Systems.....	67
Figure 4 - 24: Normalized Array Factors of All Beams at 8 GHz.....	68
Figure 4 - 25: Normalized Array Factors of All Beams at 12 GHz.....	69
Figure 4 - 26: Normalized Array Factors of All Beams at 16 GHz	69
Figure 5 - 1: Fabricated Rotman lens: (a) After printed circuit production; (b) After SMA connectors are installed.	73
Figure 5 - 2: Network Analyzer Measurement Setup for the Rotman lens	74
Figure 5 - 3: Measured Return Loss of the Beam Ports.....	75
Figure 5 - 4: Measured Return Loss of the Array Ports.....	75
Figure 5 - 5: Measured Coupling between the Beam Ports	76
Figure 5 - 6: Measured Coupling between the Two Adjacent Beam Ports	77
Figure 5 - 7: Measured Coupling between the Array Ports	78
Figure 5 - 8: Measured Coupling between the Two Adjacent Array Ports	78
Figure 5 - 9: Measured Coupling between B0 and the Dummy Ports	79
Figure 5 - 10: Measured Coupling between A6 and Dummy Ports.....	79
Figure 5 - 11: Amplitude Distribution over Antennas excited from B0	81
Figure 5 - 12: Amplitude Distribution over Antennas excited from B15	81
Figure 5 - 13: Amplitude Distribution over Antennas excited from B30	82
Figure 5 - 14: Phase Distribution over Antennas excited from B0.....	83
Figure 5 - 15: Phase Distribution over Antennas excited from B15	83
Figure 5 - 16: Phase Distribution over Antennas excited from B30.....	84
Figure 5 - 17: Measured and Simulated Array Factors of All Beams at 8 GHz.....	85
Figure 5 - 18: Measured and Simulated Array Factors of All Beams at 12 GHz.....	86
Figure 5 - 19: Measured and Simulated Array Factors of All Beams at 16 GHz.....	86
Figure 5 - 20: Printed Circuit Product of the Implemented Patch Array	92
Figure 5 - 21: The Probe-Fed Patch Array after Connector Installation: (a) Front View, (b) Back View	92
Figure 5 - 22: The Cable Connection between the Antenna and the Lens	93

Figure 5 - 23: Setup for Antenna Measurements: (a) Right View, (b) Left View....	94
Figure 5 - 24: Final Setup used in Antenna Measurements	95
Figure 5 - 25: Measured Radiation Patterns for all Beam Ports at 12 GHz.....	96
Figure A - 1: Schematic for a Microstrip Transmission Line.....	106

CHAPTER 1

INTRODUCTION

In many antenna applications, beam scanning antenna arrays are required to form multiple beams. Especially, in satellite communications and in multiple-target radar systems, multiple-beam systems are utilized.

In multiple-beam antenna systems, beams are directed into desired directions by changing the phase distribution of the antenna array and this is called the phased array antenna phenomena. Beamformers are used in order to provide the required phase distribution on the array elements.

1.1 Beamformers

Beamformers produce the required amplitude and phase distributions over the array elements in order to direct the beam into the desired direction. A typical beamformer consists of multiple input and output ports as given in Figure 1 - 1. Although the location of the output ports can change regarding the application, according to the case in Figure 1 - 1, the beamformer works as a transmitter. Therefore, the array elements are connected to the output of the beamformer and with the corresponding input configurations, beam-scanning phased array is constructed.

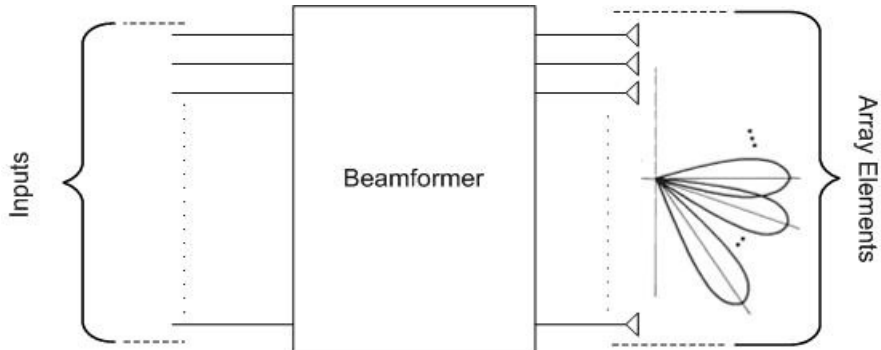


Figure 1 - 1: Beamformer Schematic

Depending on the requirements on the array aperture, beamformer can be formed as planar (2-D) or three dimensional (3-D). The 2-D beamformers produce steerable fan beams while 3-D beamformers produce steerable pencil beams.

Beamformers can be categorized in many ways; however in this thesis, the categorization that Hansen used in [1] will be used. Hansen splits the beamformers into three main categories: network beamformers, digital beamformers and microwave lens beamformers.

In the following sections of this chapter, beamformers will be abbreviated by BFN (beam-forming network) in general.

1.1.1 Network Beamformers

Network beamformers are the earliest beamformer types. With network BFNs, beam crossover levels remains unchanged, although the beamwidths and the beam angles change with frequency. Hence, if the application requires the constant beamwidths over the frequency band, network beamformers are disadvantageous.

The simplest one of network beamformers is the power divider BFN which consists of power dividers to split the input signal into N outputs to feed array elements. In

In addition, phase shifters are used to produce the desired phase distribution across the antenna array aperture.

Butler matrix is probably the most widely known network BFN. It consists of alternative rows of hybrid junctions and fixed phase shifters. Butler matrix is the analog circuit equivalent of Fast Fourier Transform (FFT). It is a simple network that can be easily implemented in stripline/microstrip; however conductor crossovers are required [1].

There are also other types of matrices such as Blass and Nolen matrices. In Blass matrix, array element transmission lines and beam port lines are intersected with a directional coupler at each intersection. However, these arrays are difficult to construct. In addition, the Nolen matrix is a generalization of both Blass and Butler matrices. Nevertheless, due to the high parts count and the difficulties connected with network adjustments, the Nolen BFN is rarely used [1].

1.1.2 Digital Beamformers

Digital BFNs use a computer or chip processor to control electronic components in order to produce exact amplitude and phase distributions for the array elements. Pre-amplifiers (LNAs), Analog-to-Digital (A/D) and Digital-to-Analog (D/A) converters are used in the digital beamformer topology as shown in Figure 1 - 2.

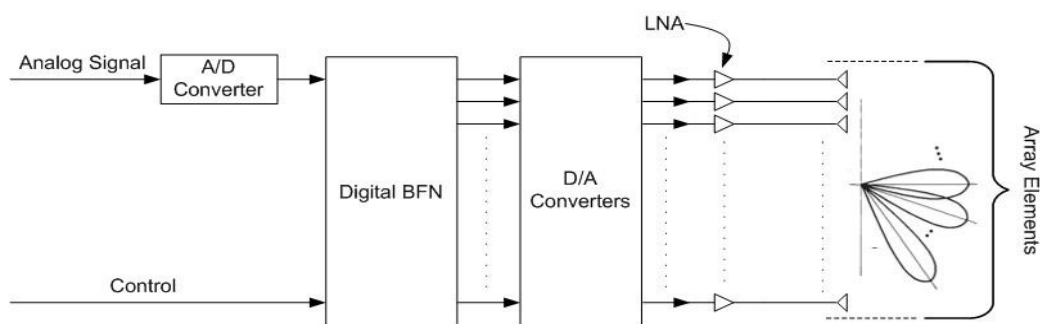


Figure 1 - 2: Digital Beamformer Topology

Digital beamformers can produce any number of multiple beams with zero phase error and flexible amplitude tapering. However, digital BFNs are limited to low microwave frequencies due to the limited bit-bandwidth product of the current A/D converter technologies [1]. Besides, very fast processors are required to handle the digitized RF data.

1.1.3 Microwave Lens Beamformers

Microwave lens beamformers use path length mechanism to introduce desired phase distributions on the array elements. As a microwave lens BFN, constrained lenses are used where the rays are guided by metal plates. A typical microwave lens beamformer structure is given in Figure 1 - 3. Input ports are connected to the beam ports that radiate a signal within the lens cavity and then the receiving ports receive the signal and transmit it to the antenna array. Positions of the beam and receiving ports and transmission line lengths are arranged so that the desired phase and amplitude distributions are obtained across the array aperture.

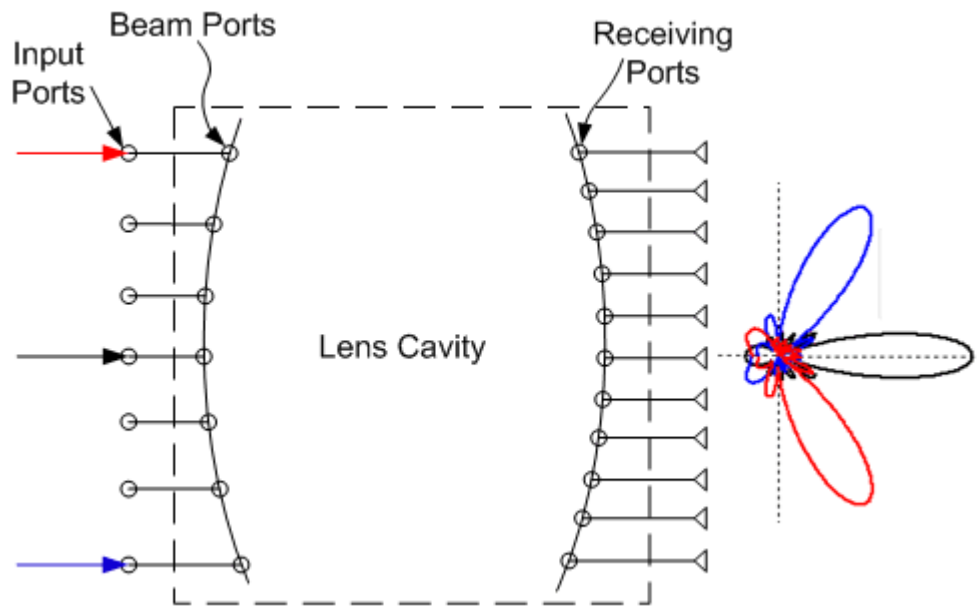


Figure 1 - 3: Microwave Lens BFN

In order to illustrate how the microwave lens beamformers work, different excitations and corresponding example patterns are plotted in Figure 1 - 3. The colored arrows correspond to the excitations of different beam ports; and with each excitation, a pattern shown with the same color is obtained at the output. In other words, when the lens is excited from the port pointed with the black arrow, the resultant beam is directed to the boresight and similarly when the ports pointed with the red and blue arrows are excited, the resultant beams are directed to the directions as shown in the figure.

Microwave lenses are especially used in wideband applications since the path-length design used in the design of microwave lenses is independent of frequency. Besides, microwave lenses can be implemented using waveguides, microstrip and stripline technologies; hence high power or low profile beamformers can be acquired according to the requirements.

The earliest constrained lens is the R-2R lens where the inner and outer lens surfaces are circular arcs with outer radius twice the inner. This shape provides perfect collimation for the feed points on the focal arc. However, due to the amplitude asymmetry between beams, sidelobe levels increase [1]. Therefore, this design has a limited use.

Gent [2] obtained generalized design equations for arbitrary lens shapes and by using these equations, Rotman and Turner [3] introduced Rotman lens phenomena. In the following section of this chapter, historical developments and usage areas of Rotman lens will be given in detail.

1.2 Rotman Lens

Rotman lens was introduced by Rotman and Turner [3] in 1960s. They designed the lens with 3 focal points and hence they improved the phase error performance and

design freedoms of the constrained lenses that Ruze [5] investigated. After the invention of Rotman lens, in Raytheon Electronic Warfare division, systems based on Rotman lens were applied in 1967 [6]. They worked on reducing the Rotman lens size by loading the parallel plate region by dielectric material and the result can be seen in Figure 1 - 4. In 1970, 2-dimensional Rotman lens stack was demonstrated which can be seen in Figure 1 - 5. After Archer (1973) [7] proposed the idea of implementing Rotman lens using printed technologies to have low-profile lens, studies on microstrip/stripline Rotman lens increased.

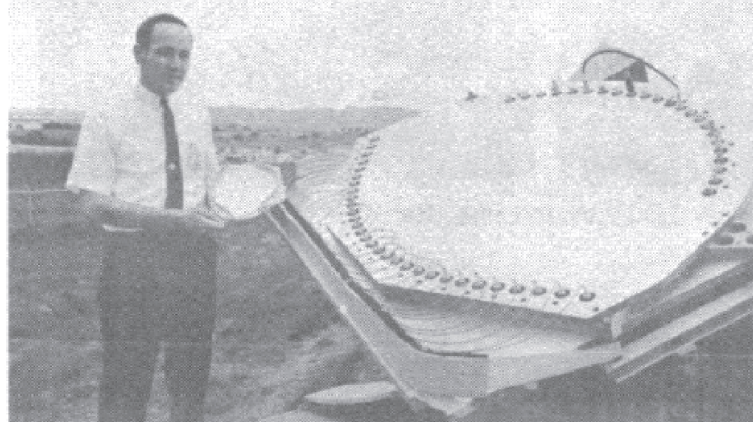


Figure 1 - 4: Reduced Lens Size by Dielectric Loading (From [6])

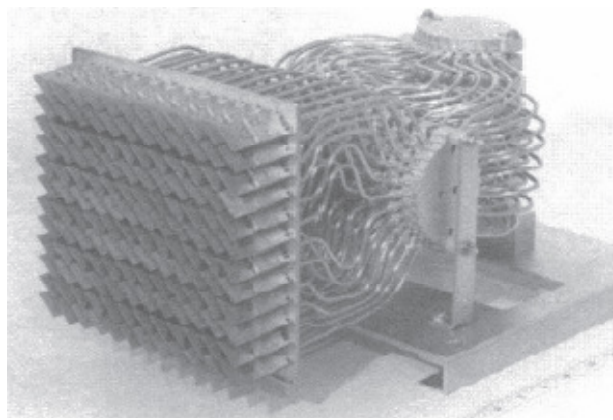


Figure 1 - 5: First 2D Rotman Lens Stack Feeding Planar (From [6])

In Rotman lens design, various design approaches can be used. Modified versions of the conventional design approach [3] and non-focal lens design were suggested. Several design approaches will be given in Chapter 2 while explaining the design procedure of Rotman lens.

1.2.1 Rotman Lens Applications

Microwave lenses are used in airborne and marine radars. Raytheon [6] used Rotman lens in marine radar, AN/SLQ-32(V) given in Figure 1 - 6 (a), in 1972 and in airborne electronic warfare pod, AN/ALQ-184 given in Figure 1 - 6 (b), in 1986.

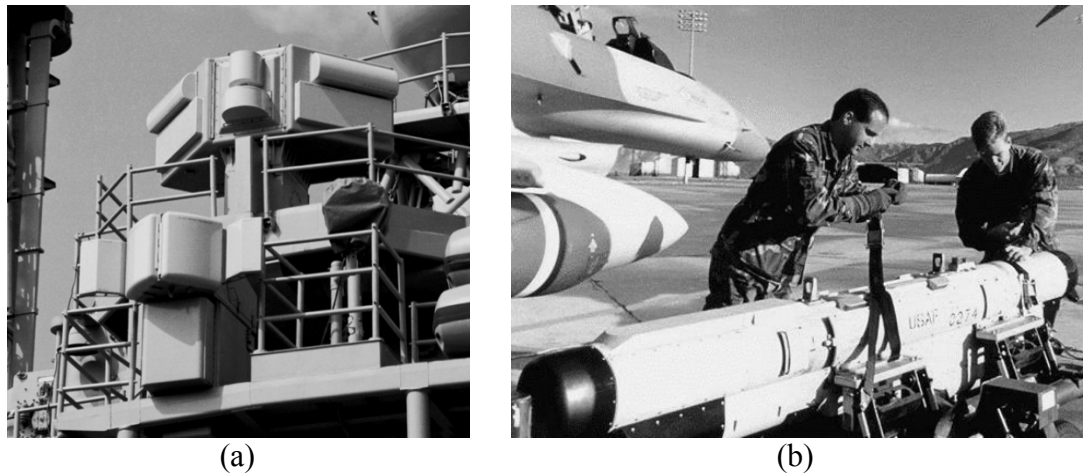


Figure 1 - 6: Rotman Lens Used Marine & Airborne Radars by Raytheon (From [9]): (a) AN/SLQ-32(V); (b) AN/ALQ-184

For applications that require three dimensional scanning, stacked Rotman lens can be used, an example of stacked Rotman lens was shown in Figure 1 - 5. Typical planar Rotman lens produces fan beams capable of two dimensional scans while the stacked Rotman lens forms three dimensional pencil beams. Pencil beams are required in space communication and imaging system applications. Therefore,

stacked Rotman lens structure can also be used in these applications. Chan [8] used stacked Rotman lenses to obtain a feed network with columns and rows to feed a hexagonal shape planar horn array to be used in satellite communication antenna system.

Using Rotman lens for photonic beam forming was proposed by Steyskal [10]. Microwave lens beamformers are good candidate for photonic imaging systems because they are passive, frequency invariant (true-time-delay) and have wide-angle scanning capabilities. In [11], passive imaging system was designed using Rotman lens as a phase processor. The imaging system was designed in the frequency band 75.5 – 93.5 GHz and photonic Rotman lens used in the system is given in Figure 1 - 7 together with the resulting example image. In the example image, the subject wearing a shirt over a concealed pistol was successfully detected.

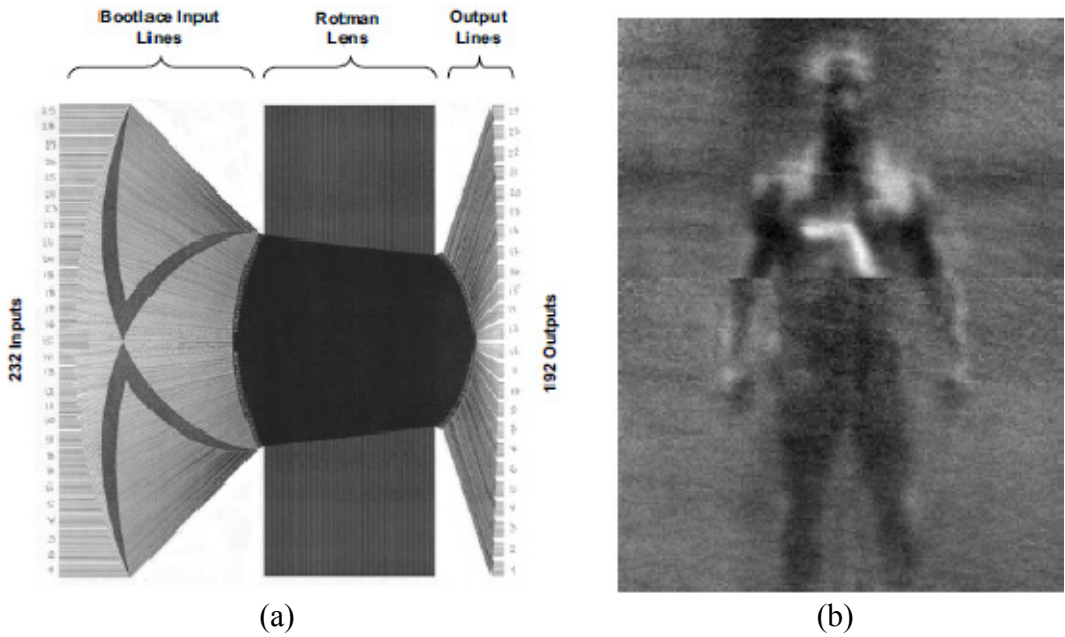


Figure 1 - 7: (a) Rotman Lens used as a Phase Processor; (b) Example Image [11]

Microwave lens beamformers are also used in automobile collision avoidance systems, for instance, in the papers [12-13] Rotman lens is used as a vehicle sensor.

In addition to the mentioned applications, there are also various potential applications of Rotman lens: autonomous aircraft landing systems, synthetic vision for ground vehicles, missile seekers, and commercial communications like building-to-building wireless communications [14].

1.3 Objective of the Thesis

In this thesis, Rotman lens design procedures and recent developments are reviewed, design procedures using different approaches are investigated and in order to verify the related research, a wide-band microstrip Rotman lens was designed and constructed. Hence, the thesis focuses on the design and manufacturing of a wide-band microstrip Rotman lens and verifying the related theoretical studies by accompanying measurements.

1.4 Thesis Outline

The thesis is organized in 6 chapters. Conducted research and the practical design issues are presented.

The 1st chapter includes general information on beamformers and Rotman lens. Also, historical developments and application areas of Rotman lens are explained.

In the 2nd chapter, different Rotman lens design approaches are mentioned and the Rotman lens design equations are derived.

In the 3rd chapter, the effects of the design parameters are investigated and the Rotman lens performance analysis is presented.

The implementation procedure of the designed wide-band microstrip Rotman lens is explained in detail in the 4th chapter. Also, the simulation results of the designed lens are given.

In the 5th chapter, manufacturing process for the implemented lens is explained. The main subject of this chapter is to present several measurement results of the manufactured lens structure. The measurement results are presented along with a comparison with the simulation results of the 4th chapter.

Conclusions related to the theoretical and experimental studies are given in the 6th chapter. Suggestions concerning further studies are also presented.

CHAPTER 2

ROTMAN LENS DESIGN PROCEDURE

In this chapter, different design approaches of the Rotman lens are given and the design equations of Rotman's [3] design are derived. Design equations for both parallel-plate/waveguide and microstrip/stripline Rotman lenses are presented.

2.1 Design Approaches

2.1.1 Rotman's Approach (The Conventional Design)

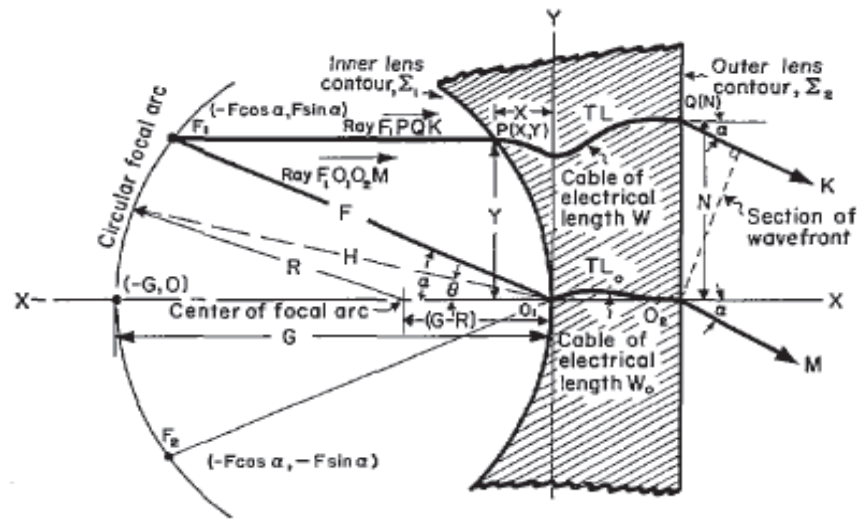


Figure 2 - 1: Microwave Lens Parameters (From [3])

In the conventional design of Rotman lens, the generalized equations obtained by Gent [2] for lenses of arbitrary shape are used [3]. The lens parameters are defined as shown in Figure 2 - 1. The focal arc locates the feeding elements and it is also called as the beam contour. Besides, the inner lens contour locates the receiving elements where the outer lens contour locates the radiating array elements. In the inner lens contour design three focal points are used: two symmetrical off-axis focal points (F_1 & F_2) and one on-axis focal point (G). The shape of the focal arc is chosen as a circle containing the three focal points. Unlike the other types of lenses, including the Ruze [5] model for which the parameters Y (the y-coordinate of an arbitrary point on the inner lens contour) and N (the coordinate of a radiating array element connected to the receiving element locating at $P(X,Y)$) equal to each other; Rotman lens allows Y and N to be different. So, this provides more degrees of freedom in the design.

In order to derive design equations for the lens contour, optical path-length equality and the lens geometry are used. The detailed derivation will be given in the latter sections of this chapter.

2.1.2 Shelton's Approach (Symmetrical Lens)

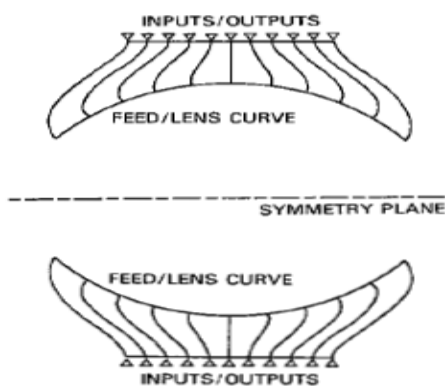


Figure 2 - 2: Symmetrical Lens Configuration (From [15])

Shelton [16] developed a symmetrical lens configuration as a modification to the Rotman lens. The beam and the inner lens contours are identical and symmetrical with respect to a symmetry plane as seen in Figure 2 - 2. This design is useful for comparable number of input and output ports.

The design equations of this type of lens are more complicated than that of Rotman's. Derivation of the design equations are explained in [15].

2.1.3 Katagi's Approach (An Improved Design Method)

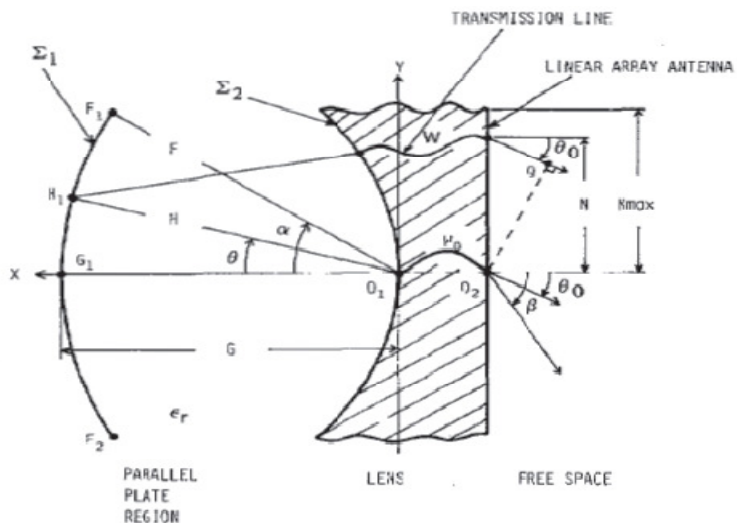


Figure 2 - 3: Katagi's Model for Rotman Lens Design (From [16])

Katagi [16] suggested an improved design method of Rotman lens in which a new design variable is introduced and the phase error on the aperture is minimized. As it can be seen in Figure 2 - 3, Katagi defined a subtended angle (α) corresponding to one of the off-axis focal points as it is defined in Rotman's model. However, the scan angle (β) corresponding to the excitation from F_1 is assumed to be different from the subtended angle (α) though scan angles were assumed to be equal to the corresponding subtended angles in Rotman's design model. Hence, Katagi [16]

introduced a new design variable consisting of the ratio of the scan angle and the subtended angle corresponding to one of the off-axis focal points.. Therefore, this variable provides a new degree of freedom compared to the conventional design. Katagi [16] also suggested that the shape of the beam contour is not necessarily a circular arc.

2.1.4 Gagnon's Approach (Refocusing)

Gagnon [17] introduced refocusing procedure for dielectric-filled Rotman lens according to Snell's law. Therefore, applying Snell's law yields a ratio of $\sqrt{\epsilon_r}$ between the sines of the scan angle and the subtended angle of the beam contour. This approach provides beam and array port positions which give improved coupling to the outermost beam ports, especially for printed lenses used with small arrays.

2.1.5 Hansen's Approach (Design Trades)

Hansen [18] used six basic design parameters: focal angle, focal ratio, beam angle to ray angle ratio, maximum beam angle, focal length and array element spacing. A seventh parameter, ellipticity, allows the beam contour to be elliptical instead of circular. The parameters beam angle (subtended angle) to ray angle (scan angle) ratio and ellipticity are additions to the parameters of the conventional design. Hansen explained the effects of the seven design parameters on the shape, and on the geometric phase and amplitude errors of a Rotman lens in detail [18].

2.2 Derivation of the Design Equations

In this section, the design equations will be derived for parallel-plate/waveguide and microstrip/stripline Rotman lenses. Rotman's [3] conventional design approach will be used in the derivation with the addition of an elliptical beam contour.

For the Rotman lenses implemented in parallel-plate or waveguide structures, design equations of Rotman [3] can be adopted with the change of the elliptical beam contour design. However, for microstrip/stripline Rotman lenses, derivation should be modified to include the dielectric properties.

2.2.1 Design Equations for Parallel-Plate/Waveguide Rotman Lenses

The conventional design procedure is used to derive the equations. To begin with, Rotman lens design parameters that will be used in the derivation are shown in Figure 2 - 4.

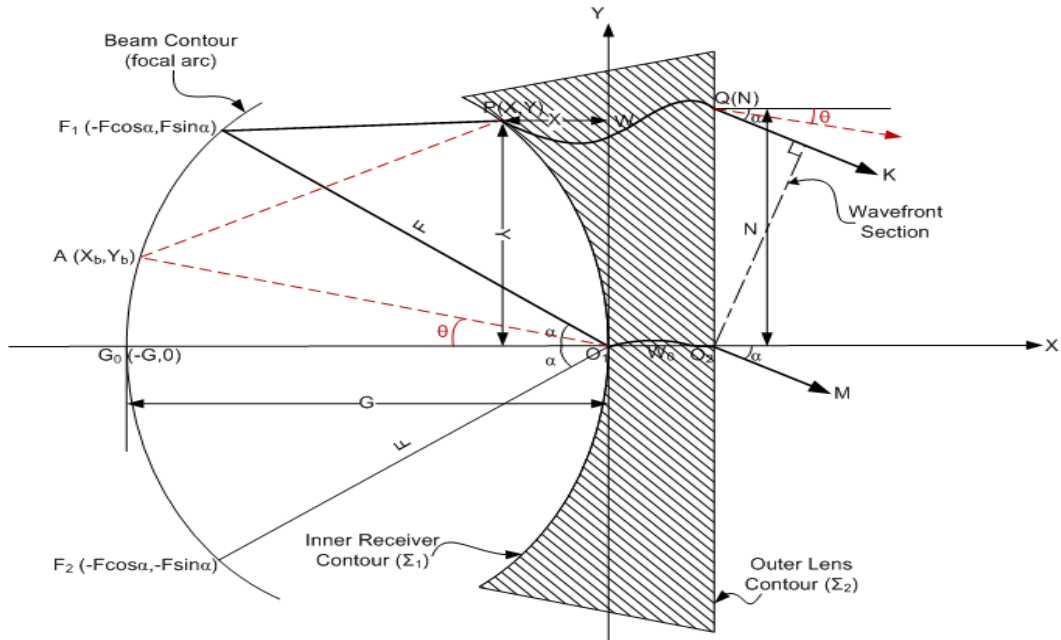


Figure 2 - 4: Rotman Lens Design Parameters

Before the derivation, parameters given in Figure 2 - 4 are described in Table 2 - 1. F , G , N and α are the design parameters where X , Y , W , X_b and Y_b are the parameters to be calculated in order to construct the lens structure.

Table 2 - 1: Description of the Design Parameters

F	Off-axis focal length
G	On-axis focal length
α	Off-center focal angle
θ	Subtended angle for beam port phase centers / Scan angle
F_1, F_2	Symmetrical off-axis focal points
G_0	On-axis focal point
W_0	Electrical length of the transmission line between receivers and array elements through the origin
W	Electrical length of the transmission line between typical receivers and array elements
X, Y	Coordinates of the receiver port phase centers
N	Coordinate for the array elements
X_b, Y_b	Coordinates of the typical beam port phase centers

In the design procedure, design equations for the inner receiver contour (Σ_1) and the beam contour will be derived individually. First, inner receiver contour design will be introduced and then the beam contour coordinates will be calculated.

Inner Receiver Contour Design

The inner contour (Σ_1) locates the phase centers of the receivers and the outer contour (Σ_2) which is chosen to be a straight front face defines the positions of the radiating array elements.

The contour Σ_1 is defined by the two coordinates (X, Y) where the point P(X, Y) is a typical point on Σ_1 . The contour Σ_2 is defined by the single coordinate N where the point Q(N) is a typical point on Σ_2 . Locations of the array elements define the parameter N, so N is a design parameter defined previously. Σ_1 and Σ_2 are connected by transmission lines, namely, the point P(X, Y) is connected to the point Q(N) by a

transmission line of electrical length W. Therefore, in the inner receiver contour design, the parameters X, Y and W should be computed in terms of design parameters.

In the inner contour (Σ_1) design, three focal points are used: one on-axis focal point (G_0) and two symmetrical off-axis focal points (F_1 & F_2).

In order to derive the design equations, optical path-length equality and the relationships coming from the geometry are written.

Optical path-length equality between a general ray ($\overrightarrow{F_1PQK}$) and the ray through the origin ($\overrightarrow{F_1O_1O_2M}$) give:

$$\overrightarrow{(F_1P)} + W + N \sin \alpha = F + W_0 \quad (2.1)$$

$$\overrightarrow{(F_2P)} + W - N \sin \alpha = F + W_0 \quad (2.2)$$

$$\overrightarrow{(G_0P)} + W = G + W_0 \quad (2.3)$$

From the geometry:

$$\overrightarrow{(F_1P)}^2 = F^2 + X^2 + Y^2 + 2FX \cos \alpha - 2FY \sin \alpha \quad (2.4)$$

$$\overrightarrow{(F_2P)}^2 = F^2 + X^2 + Y^2 + 2FX \cos \alpha + 2FY \sin \alpha \quad (2.5)$$

$$\overrightarrow{(G_0P)}^2 = (G + X)^2 + Y^2 \quad (2.6)$$

For the simplicity, all variables and all equations are normalized with respect to the focal length F.

The normalized parameters are:

$$\eta = N/F, \quad x = X/F, \quad y = Y/F, \quad w = (W - W_0)/F, \quad g = G/F$$

Also, define intermediate parameters:

$$a_0 = \cos \alpha , b_0 = \sin \alpha$$

Normalize the equations (2.1) to (2.6) by the focal length F:

$$\frac{\overrightarrow{F_1 P}}{F} = 1 - w - \eta b_0 \quad (2.1a)$$

$$\frac{\overrightarrow{F_2 P}}{F} = 1 - w + \eta b_0 \quad (2.2a)$$

$$\frac{\overrightarrow{G_0 P}}{F} = g - w \quad (2.3a)$$

$$\frac{\overrightarrow{F_1 P}^2}{F^2} = 1 + x^2 + y^2 + 2a_0x - 2b_0y \quad (2.4a)$$

$$\frac{\overrightarrow{F_2 P}^2}{F^2} = 1 + x^2 + y^2 + 2a_0x + 2b_0y \quad (2.5a)$$

$$\frac{\overrightarrow{G_0 P}^2}{F^2} = (g + x)^2 + y^2 \quad (2.6a)$$

Square the equations (2.1a) to (2.3a) and equate them to the equations (2.4a) to (2.6a):

$$(1 - w - \eta b_0)^2 = 1 + x^2 + y^2 + 2a_0x - 2b_0y \quad (2.7)$$

$$(1 - w + \eta b_0)^2 = 1 + x^2 + y^2 + 2a_0x + 2b_0y \quad (2.8)$$

$$(g - w)^2 = (g + x)^2 + y^2 \quad (2.9)$$

Rewrite the equations (2.7), (2.8) and (2.9) implicitly:

$$w^2 - 2w + 2b_0\eta w + b_0^2\eta^2 - 2b_0\eta = x^2 + y^2 + 2a_0x - 2b_0y \quad (2.7a)$$

$$w^2 - 2w - 2b_0\eta w + b_0^2\eta^2 + 2b_0\eta = x^2 + y^2 + 2a_0x + 2b_0y \quad (2.8a)$$

$$w^2 - 2gw = x^2 + y^2 + 2gx \quad (2.9a)$$

After manipulating (2.7a) and (2.8a):

$$y = \eta(1 - w) \quad (2.10)$$

$$w^2 - 2w + b_0^2\eta^2 = x^2 + y^2 + 2a_0x \quad (2.11)$$

By substituting (2.10) in (2.9a):

$$x = -\frac{(g-1)}{(g-a_0)}w - \frac{(b_0^2\eta^2)}{2(g-a_0)} \quad (2.12)$$

Manipulation of (2.9a) and (2.11) gives the relation between w and η :

$$aw^2 + bw + c = 0 \quad (2.13)$$

where

$$\begin{aligned} a &= \left[1 - \eta^2 - \left(\frac{(g-1)}{(g-a_0)} \right)^2 \right], \\ b &= \left[2g \left(\frac{(g-1)}{(g-a_0)} \right) - \left(\frac{(g-1)}{(g-a_0)^2} \right) b_0^2\eta^2 + 2\eta^2 \right] - 2g, \\ c &= \left[\left(\frac{(gb_0^2\eta^2)}{(g-a_0)} \right) - \left(\frac{(b_0^4\eta^4)}{4(g-a_0)^2} \right) - \eta^2 \right]. \end{aligned}$$

From (2.13), w can be computed as a function of η for fixed values of design parameters α and g . By substituting w and η values into (2.10) & (2.12), y and x can be determined respectively.

Beam Contour Design

The beam contour is assumed to have an ellipse shape that passes through all three focal points. To be able to define the ellipse, design parameters shown in Figure 2 - 5 need to be introduced.

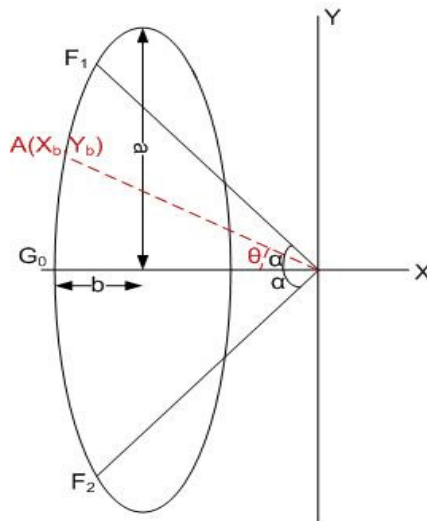


Figure 2 - 5: Elliptic Beam Contour Parameters

In order to derive the equations for the beam contour, the equation of the ellipse should be derived. So, for the ellipse equation, eccentricity parameter (e) is defined and given as (2.14).

$$e = \sqrt{\frac{(a^2 - b^2)}{(a^2)}} \quad (2.14)$$

The function of the ellipse shown in Figure 2 - 5 can be written as:

$$\frac{(x + g - b)^2}{b^2} + \frac{y^2}{a^2} = 1 \quad (2.15)$$

By using (2.14), b can be written in terms of a and e:

$$b^2 = a^2(1 - e^2) \quad (2.16)$$

By substituting (2.16) in (2.15):

$$(x + g - a\sqrt{(1 - e^2)})^2 + y^2(1 - e^2) = a^2(1 - e^2) \quad (2.17)$$

Since all focus points are on the beam contour, a can be calculated by substituting the coordinates of the known off-axis foci:

$$a = \frac{(e \sin \alpha)^2 + 2g \cos \alpha - g^2 - 1}{\sqrt{(1 - e^2)}(2 \cos \alpha - 2g)} \quad (2.18)$$

In order to find (x_b, y_b) coordinates for a given e and θ ; y_b is substituted with $y_b = -\tan \theta x_b$. Then, with the manipulation of (2.17), x_b and y_b can be computed from the equations (2.19) & (2.20) where the parameter, a is calculated from (2.18).

$$[1 + (1 - e^2) \tan \theta^2]x_b^2 + (2g - 2a\sqrt{1 - e^2})x_b + g^2 - 2ag\sqrt{1 - e^2} = 0 \quad (2.19)$$

$$y_b = -\tan \theta x_b \quad (2.20)$$

2.2.2 Design Equations for Microstrip/Stripline Rotman Lenses

In microstrip/stripline Rotman lens design, the dielectric constant of the substrate which is used to fill the lens cavity should be taken into account. With the transmission lines implemented in microstrip/stripline, the effective dielectric constant of the transmission lines should also be included in the design equations.

Design parameters for microstrip/stripline Rotman lenses are shown in Figure 2 - 6. As seen in the figure, the only parameters different from the parallel-plate/waveguide Rotman lens are ϵ_r and ϵ_{re} where ϵ_r is the dielectric constant of the substrate and ϵ_{re} is the effective dielectric constant of the transmission lines connecting the receivers to the array elements.

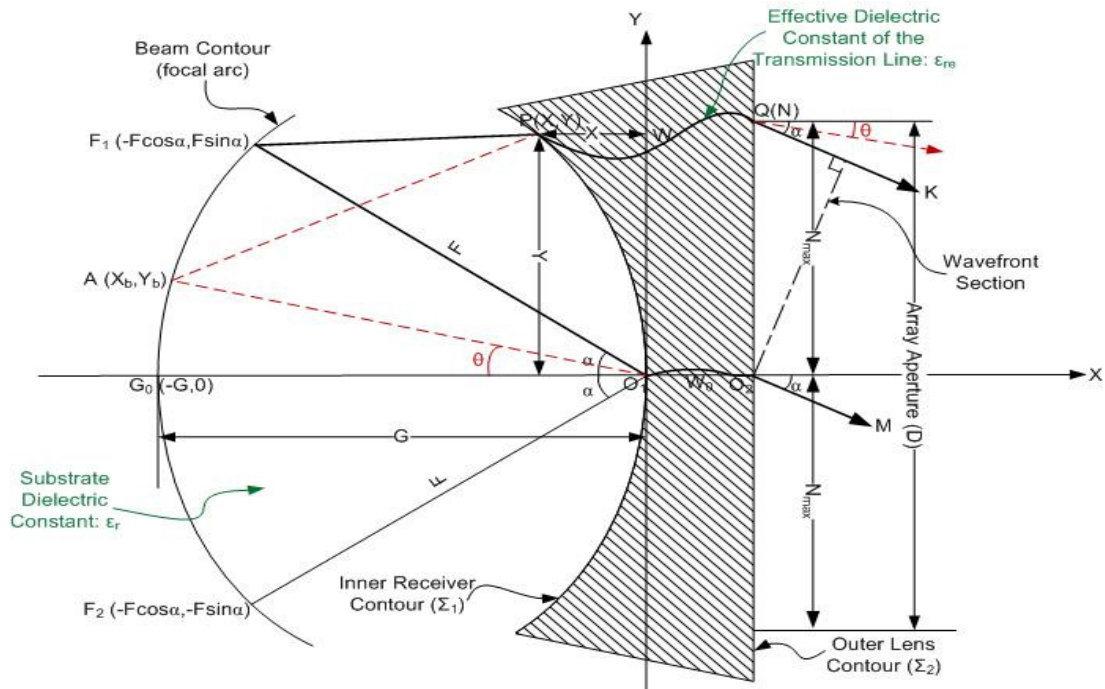


Figure 2 - 6: Microstrip/Stripline Rotman Lens Design Parameters

For microstrip/stripline Rotman lens, design equations of the inner contour Σ_1 and corresponding transmission line lengths should be modified in order to take the substrate parameters into account. However, since the beam contour is independent of the dielectric substrate, the beam contour equations (2.19) & (2.20) derived in the previous section could be used also for microstrip/stripline case.

Inner Receiver Contour Design

In the derivation of the inner receiver contour design equations, the conventional design approach is used with the optical path-length equality modified considering the dielectric substrate. The procedure for derivation is similar to the procedure for the parallel-plate/waveguide Rotman lenses.

Optical path-length equality between a general ray ($\overrightarrow{F_1PQK}$) and the ray through the origin ($\overrightarrow{F_1O_1O_2M}$) for microstrip/stripline case become:

$$\sqrt{\epsilon_r(F_1P)} + \sqrt{\epsilon_{re}}W + N \sin \alpha = \sqrt{\epsilon_r}F + \sqrt{\epsilon_{re}}W_0 \quad (2.21)$$

$$\sqrt{\epsilon_r(F_2P)} + \sqrt{\epsilon_{re}}W - N \sin \alpha = \sqrt{\epsilon_r}F + \sqrt{\epsilon_{re}}W_0 \quad (2.22)$$

$$\sqrt{\epsilon_r(G_0P)} + \sqrt{\epsilon_{re}}W = \sqrt{\epsilon_r}G + \sqrt{\epsilon_{re}}W_0 \quad (2.23)$$

From the geometry:

$$(\overrightarrow{F_1P})^2 = F^2 + X^2 + Y^2 + 2FX \cos \alpha - 2FY \sin \alpha \quad (2.24)$$

$$(\overrightarrow{F_2P})^2 = F^2 + X^2 + Y^2 + 2FX \cos \alpha + 2FY \sin \alpha \quad (2.25)$$

$$(\overrightarrow{G_0P})^2 = (G + X)^2 + Y^2 \quad (2.26)$$

Normalizing the parameters by the focal length F , the normalized parameters are:

$$\eta = N/F, \quad x = X/F, \quad y = Y/F, \quad w = (W - W_0)/F, \quad g = G/F$$

For simplicity of the equations, define the intermediate parameters:

$$a_0 = \cos \alpha, \quad b_0 = \sin \alpha$$

Normalize the equations (2.21) to (2.26) by F:

$$\sqrt{\varepsilon_r} \frac{\overrightarrow{(F_1 P)}}{F} = \sqrt{\varepsilon_r} - \sqrt{\varepsilon_{re}} w - \eta b_0 \quad (2.21a)$$

$$\sqrt{\varepsilon_r} \frac{\overrightarrow{(F_2 P)}}{F} = \sqrt{\varepsilon_r} - \sqrt{\varepsilon_{re}} w + \eta b_0 \quad (2.22a)$$

$$\sqrt{\varepsilon_r} \frac{\overrightarrow{(G_0 P)}}{F} = \sqrt{\varepsilon_r} g - \sqrt{\varepsilon_{re}} w \quad (2.23a)$$

$$\frac{\overrightarrow{(F_1 P)}^2}{F^2} = 1 + x^2 + y^2 + 2a_0x - 2b_0y \quad (2.24a)$$

$$\frac{\overrightarrow{(F_2 P)}^2}{F^2} = 1 + x^2 + y^2 + 2a_0x + 2b_0y \quad (2.25a)$$

$$\frac{\overrightarrow{(G_0 P)}^2}{F^2} = (g + x)^2 + y^2 \quad (2.26a)$$

Square the equations (2.21a) to (2.23a) and equate them to the equations (2.24a) to (2.26a):

$$(1 - \frac{\sqrt{\varepsilon_{re}}}{\sqrt{\varepsilon_r}} w - \frac{\eta b_0}{\sqrt{\varepsilon_r}})^2 = 1 + x^2 + y^2 + 2a_0x - 2b_0y \quad (2.27)$$

$$\left(1 - \frac{\sqrt{\varepsilon_{re}}}{\sqrt{\varepsilon_r}} w + \frac{\eta b_0}{\sqrt{\varepsilon_r}}\right)^2 = 1 + x^2 + y^2 + 2a_0x + 2b_0y \quad (2.28)$$

$$(g - \frac{\sqrt{\varepsilon_{re}}}{\sqrt{\varepsilon_r}} w)^2 = (g + x)^2 + y^2 \quad (2.29)$$

Rewrite the equations (2.27), (2.28) and (2.29) implicitly:

$$\begin{aligned} \frac{\sqrt{\varepsilon_{re}}}{\sqrt{\varepsilon_r}} w^2 - 2 \frac{\sqrt{\varepsilon_{re}}}{\sqrt{\varepsilon_r}} w + 2 \frac{\sqrt{\varepsilon_{re}}}{\sqrt{\varepsilon_r}} b_0 \eta w + \frac{b_0^2 \eta^2}{\varepsilon_r} - 2 \frac{b_0 \eta}{\sqrt{\varepsilon_r}} \\ = x^2 + y^2 + 2a_0 x - 2b_0 y \end{aligned} \quad (2.27a)$$

$$\begin{aligned} \frac{\sqrt{\varepsilon_{re}}}{\sqrt{\varepsilon_r}} w^2 - 2 \frac{\sqrt{\varepsilon_{re}}}{\sqrt{\varepsilon_r}} w - 2 \frac{\sqrt{\varepsilon_{re}}}{\sqrt{\varepsilon_r}} b_0 \eta w + \frac{b_0^2 \eta^2}{\varepsilon_r} + 2 \frac{b_0 \eta}{\sqrt{\varepsilon_r}} \\ = x^2 + y^2 + 2a_0 x + 2b_0 y \end{aligned} \quad (2.28a)$$

$$\frac{\varepsilon_{re}}{\varepsilon_r} w^2 - 2g \frac{\sqrt{\varepsilon_{re}}}{\sqrt{\varepsilon_r}} w = x^2 + y^2 + 2gx \quad (2.29a)$$

After manipulating (2.27a) and (2.28a):

$$y = \frac{\eta}{\sqrt{\varepsilon_r}} \left(1 - \frac{\sqrt{\varepsilon_{re}}}{\sqrt{\varepsilon_r}} w \right) \quad (2.30)$$

$$\frac{\varepsilon_{re}}{\varepsilon_r} w^2 - 2 \frac{\sqrt{\varepsilon_{re}}}{\sqrt{\varepsilon_r}} w + \frac{\eta^2 b_0^2}{\varepsilon_r} = x^2 + y^2 + 2a_0 x \quad (2.31)$$

By substituting (2.30) in (2.29a):

$$x = \frac{\sqrt{\varepsilon_{re}}}{\sqrt{\varepsilon_r}} \frac{(1-g)}{(g-a_0)} w - \frac{\eta^2 b_0^2}{2(g-a_0)\varepsilon_r} \quad (2.32)$$

Manipulation of (2.29a) and (2.31) give the relation between w and η :

$$aw^2 + bw + c = 0 \quad (2.33)$$

where

$$a = \left[\frac{\varepsilon_{re}}{\varepsilon_r} \left(1 - \left(\frac{g-1}{g-a_0} \right)^2 - \frac{\eta^2}{\varepsilon_r} \right) \right]$$

$$b = \left[\frac{\sqrt{\epsilon_{re}}}{\sqrt{\epsilon_r}} \left(2g \left(\frac{g-1}{g-a_0} - 1 \right) - \frac{(g-1)}{(g-a_0)^2} b_0^2 \frac{\eta^2}{\epsilon_r} + 2 \frac{\eta^2}{\epsilon_r} \right) \right]$$

$$c = \left[\frac{gb_0^2\eta^2}{(g-a_0)\epsilon_r} - \frac{b_0^4\eta^4}{4\epsilon_r^2(g-a_0)^2} - \frac{\eta^2}{\epsilon_r} \right]$$

From (2.33), w can be computed as a function of η for fixed values of design parameters α and g . By substituting these w and η values into (2.30), y can be determined. Then, x can be computed by substituting the calculated w into (2.32).

Derived equations are verified by comparing the equations derived by Kim [19]. As a shortcut, one can obtain the equations for the microstrip/stripline Rotman lens by simply substituting the variables w and η in the equations for parallel-plate/waveguide case with $\frac{\sqrt{\epsilon_{re}}}{\sqrt{\epsilon_r}}w$ and $\frac{1}{\sqrt{\epsilon_r}}\eta$, respectively.

2.3 Optical Aberrations

The design parameters α, g and e should be chosen to minimize the optical aberrations. The optical aberration of the lens is the path-length error which is defined as the difference between the path lengths of the central ray through the origin and any other ray. Both of the rays are traced from an arbitrary point on the beam contour through the lens and terminated at the emitted wavefront normal.

Path-length error (ΔL) is in the form of length and its unit is meters. In order to convert the path-length error to the phase error in degrees, (2.33) can be used where λ is the wavelength at the frequency at which the phase error is calculated.

$$\text{Phase Error} = \frac{\Delta L \times 360^\circ}{\lambda} \quad (2.33)$$

2.3.1 Path Length Error for Parallel-Plate/Waveguide Rotman Lens

For the parallel-plate/waveguide Rotman lenses, path-length error can be written in terms of the parameters shown in Figure 2 - 4.

To begin with, by definition, path-length error can be written as:

$$\Delta L = [(\overrightarrow{AP}) + W + N \sin \theta] - [(\overrightarrow{AO_1}) + W_0] \quad (2.34)$$

Normalizing the path-length error formulation by F:

$$\Delta l = \left[\frac{(\overrightarrow{AP}) - (\overrightarrow{AO_1})}{F} \right] + w + \eta \sin \theta \quad (2.35)$$

Rewrite the equation in terms of beam and lens contour coordinates:

$$\Delta l = \sqrt{(x - x_b)^2 + (y - y_b)^2} - \sqrt{x_b^2 + y_b^2} + w + \eta \sin \theta \quad (2.36)$$

Normalized path-length error can be calculated from (2.36) by using the normalized coordinates of the beam and lens contours.

In [5], Ruze gives a detailed phase-error optimization for several types of lenses. It is stated that for straight front face lenses, the amount of refocusing required to minimize the phase error is $\frac{1}{2}(\alpha^2 - \theta^2)F$ where θ is the angle at which correction is required. Therefore, using his refocusing formula, for $\theta=0^\circ$ the optimum value of g becomes:

$$g = 1 + \frac{\alpha^2}{2} \quad (2.37)$$

2.3.2 Path Length Error for Microstrip/Stripline Rotman Lens

For the microstrip/ stripline Rotman lenses, path-length error can be written in terms of the parameters shown in Figure 2 - 6. In this case, the ray through the medium is affected by the corresponding dielectric parameters. Therefore, path-length error can be written as:

$$\Delta L = [\sqrt{\epsilon_r}(\vec{AP}) + \sqrt{\epsilon_{re}}W + N \sin \theta] - [\sqrt{\epsilon_r}(\vec{AO_1}) + \sqrt{\epsilon_{re}}W_0] \quad (2.38)$$

Normalized path length error becomes:

$$\Delta l = \sqrt{\epsilon_r} \left[\frac{(\vec{AP}) - (\vec{AO_1})}{F} \right] + \sqrt{\epsilon_{re}}w + \eta \sin \theta \quad (2.39)$$

Rewrite the equation in terms of beam contour and lens contour coordinates:

$$\Delta l = \sqrt{\epsilon_r} \left(\sqrt{(x - x_b)^2 + (y - y_b)^2} - \sqrt{x_b^2 + y_b^2} \right) + \sqrt{\epsilon_{re}}w + \eta \sin \theta \quad (2.40)$$

Normalized path-length error for the microstrip/ stripline Rotman lenses can be calculated from (2.40) by using the normalized coordinates of the beam and lens contours.

2.4 MATLAB® Script

In order to calculate the coordinates of the lens and beam contours, a simple script is written in MATLAB® [28] program. The script consists of the functions to calculate the coordinates according to given design parameters. Two functions are written in order to calculate the beam contour and inner receiver contour coordinates, individually. Besides, in order to find the optimum design parameters to minimize the path-length error, a script is also written to calculate the path-length error from the calculated coordinates.

The inputs of the function to calculate the beam contour coordinates are the parameters α , θ , g and e . Hence, using these parameters, the function calculates the normalized beam contour coordinates and outputs x_b and y_b values.

The function that calculates the coordinates of the inner receiver contour uses the parameters α , g , η , ϵ_r and ϵ_{re} as inputs. Therefore, the function outputs the normalized coordinates of the points on the receiver contour (x,y) and the electrical length (w) of the transmission line connecting the receiver probes to the antennas.

After calculating the coordinates of the beam and receiver contours, using the calculated values, path-length error is calculated with a function for each point on the contour. The inputs of the function are the calculated coordinates x_b , y_b , x , y , w and the parameters θ , η , ϵ_r and ϵ_{re} .

By using these functions, parametric study on the design parameters is accomplished and the results of this study will be given in the following chapter.

CHAPTER 3

PARAMETRIC STUDY ON DESIGN PARAMETERS

In this chapter, the effects of the design parameters introduced in Chapter 2 (shown in Figure 2 - 6) will be investigated. Each design parameter will be examined independently in order to see how they affect the lens shape and the lens performance. Namely, the effects on the lens geometry and lens size will be inspected together with the effects on the phase error performance and the frequency bandwidth.

All of the design parameters affect the phase error performance of the lens. However the parameters g , e , n_{max} and α affect the lens coordinates directly. The parameter ε_r affects the lens size by scaling the coordinates. Since the focal length F is the normalization factor, overall geometrical size of the lens depends on F . Also, the choice of the focal length, F together with the parameter n_{max} specifies the distance between the antenna elements and this distance affects the operating frequency bandwidth of the lens.

In order to investigate the phase-error performance, path-length errors are examined. For each design parameter, path-length errors are calculated for different values of the parameter by scanning the pre-determined values using the developed MATLAB[®] [28] program mentioned in the previous chapter.

3.1 Focal Ratio – g

The parameter focal ratio, as mentioned in Chapter 2, is defined as the ratio of on-axis focal length (G) to off-axis focal length (F).

The focal ratio (g) affects both beam contour and inner lens contour coordinates. Beam and lens contour variations with changing values of g can be observed in Figure 3 - 1 (other design parameters are fixed and chosen as tabulated in Table 3 - 1). Effects of g on lens shape can be summarized as:

- With decreasing g , beam contour flattens
- With increasing g , lens contour flattens

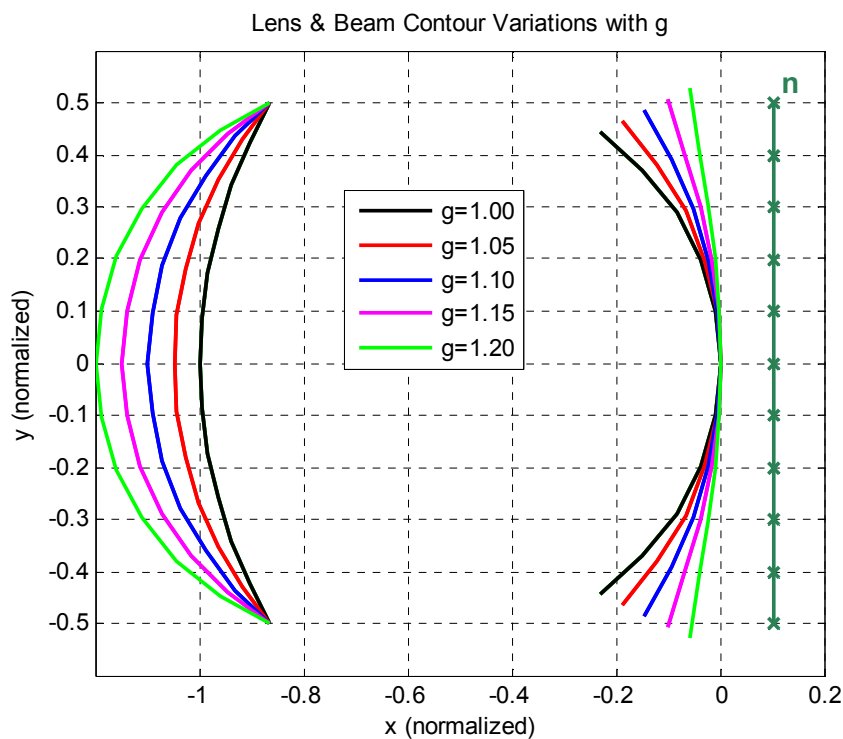


Figure 3 - 1: Lens & Beam Contour Variations with g

In rotman lens design, the choice of g is important. In [5], Ruze investigated phase-error optimization for many lens types including straight front face lenses. Ruze showed that for F/D ratio greater than 0.8 and for a circular beam contour, the phase deviation is minimized by moving the feed inward to the inner lens contour by the amount of $\left[\frac{1}{2}(\theta^2 - \alpha^2)F\right]$ where θ is the beam angle (subtended angle) and α is the maximum scan angle defined previously. The condition for F/D corresponds to $n_{max} < 0.625$ for our case since D is equal to $2n_{max}$. By applying this refocusing at $\theta=0^\circ$ optimum g corresponds to;

$$g = 1 + \frac{\alpha^2}{2} \quad (3.1)$$

In order to observe how the focal ratio, g affects the phase-error performance of the Rotman lens, other design parameters are chosen as tabulated in Table 3 - 1.

Table 3 - 1: Chosen Design Parameters to Observe "g" Effects

n_{max}	0.5
e	0 (circular arc)
ϵ_r	1 (air-filled)
α	30°

For the given design parameters, optimum g is calculated as 1.137 from (3.1). Maximum normalized path-length error over antenna elements for all scan angles is plotted in Figure 3 - 2 for different “ g ” and according to the figure, the phase error is minimized when g is equal to 1.137.

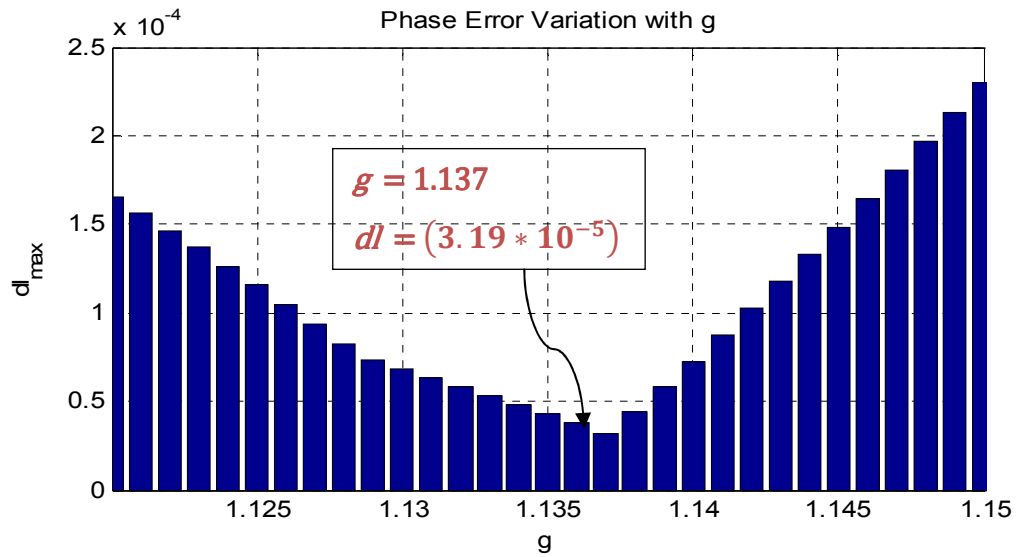


Figure 3 - 2: Phase-Error Variation with g

For the condition Ruze [5] gave, (3.1) gives the optimum g value for air-filled parallel-plate rotman lens structure. Effects of the other parameters on optimum g and the phase error will be discussed in the following sections in this chapter.

3.2 Normalized Array Aperture – $2 \times n_{max}$

The parameter N_{max} is the distance between the furthest antenna element in the array and the midpoint of the array, namely it equals to the half of the array aperture. Besides, the parameter n_{max} is the normalized version of N_{max} with the focal length, F .

Table 3 - 2: Chosen Design Parameters to Observe " n_{max} " Effects

e	0 (circular arc)
ϵ_r	1 (air-filled)
α	30°

In order to investigate the effects of n_{max} on the phase-error performance of the rotman lens, first, the optimum g values need to be found. Optimum g values for different n_{max} are computed by scanning g values for the other design parameters given in Table 3 - 2 and optimum g and the corresponding maximum normalized path-length errors are given in Table 3 - 3. Moreover, for the visualization, plots of “Optimum g vs. n_{max} ” and “ dl_{max} vs. n_{max} ” are also given in Figure 3 - 3 and Figure 3 - 4, respectively. Therefore, the results can be summarized as:

- Optimum g value decreases with increasing n_{max}
- Maximum normalized path-length error increases with increasing

n_{max}

Table 3 - 3: Optimum g & dl_{max} for Different “ n_{max} ”

n_{max}	0.4	0.5	0.6	0.7	0.8
Optimum g	1.144	1.137	1.128	1.116	1.099
dl_{max}	1.07 $\times 10^{-5}$	3.19 $\times 10^{-5}$	8.86 $\times 10^{-5}$	2.23 $\times 10^{-4}$	5.34 $\times 10^{-4}$

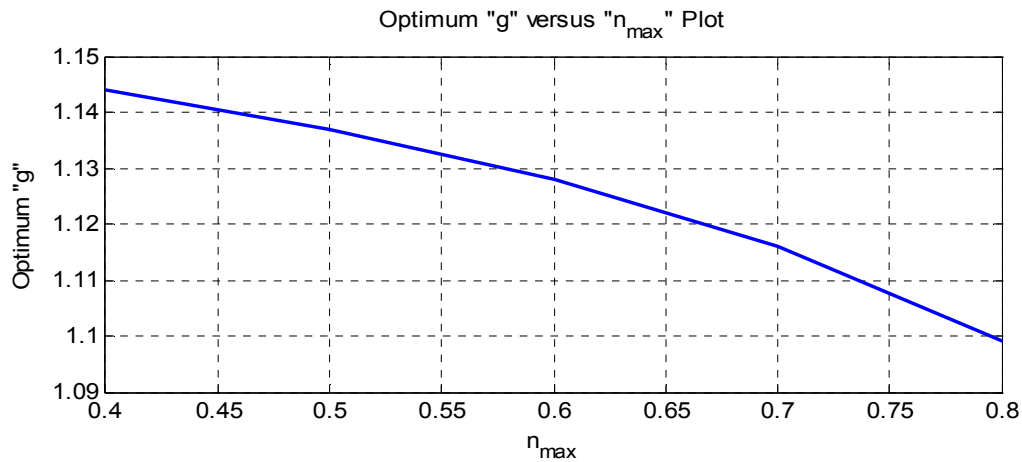


Figure 3 - 3: Optimum g vs. n_{max} Plot

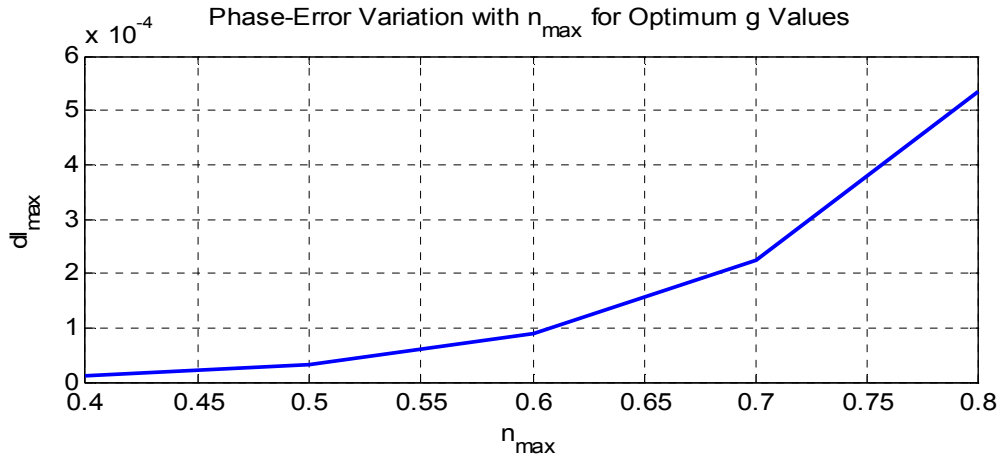


Figure 3 - 4: Phase-Error Variation with n_{max} for Optimum g

To conclude the discussion about the parameter n_{max} , effects on the lens contours are also investigated. Beam and lens contour variations with n_{max} can be observed in Figure 3 - 5. The parameter n_{max} directly affects the lens contour since it appears in the lens contour design equations (given in the previous chapter). Besides, since n_{max} does not appear in the beam contour design equations, beam contour isn't affected by the changes in n_{max} . However, since the changes in n_{max} alter the optimum g value

required to achieve minimum phase error, the beam contour is also affected in order to realize the optimum lens design.

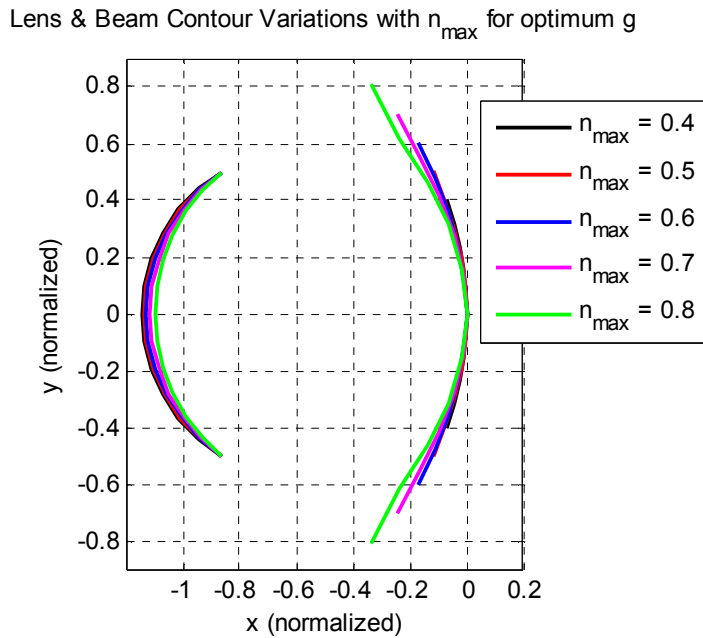


Figure 3 - 5: Lens & Beam Contour Variations with n_{\max} for optimum g

3.3 Eccentricity Parameter – e

Eccentricity parameter, e is defined in the previous chapter to illustrate how elliptic the beam contour is. By its definition, e is bounded in the interval: $0 \leq e < 1$. When e is equal to 0, the contour becomes circular and when it increases, the contour becomes more elliptical.

In the parametric study of e , the values from 0 to 0.5 are investigated and optimum g & e pair is determined for different normalized apertures (n_{\max}). Optimum g & e pair is computed to minimize the maximum path-length errors and the results for

different n_{max} are given in Table 3 - 4. In addition, “optimum g & e pair versus n_{max} ” plot is also given in Figure 3 - 6. Hence, the results can be summarized as:

- Optimum g value decreases with increasing n_{max}
- Optimum e value increases with increasing n_{max}

Table 3 - 4: Optimum g & e Pair and dl for Different “ n_{max} ”

n_{max}		0.4	0.5	0.6	0.7	0.8
Optimum	g	1.143	1.136	1.127	1.115	1.098
	e	0.06	0.08	0.09	0.11	0.15
dl_{max}		9.37 $\times 10^{-6}$	3.10 $\times 10^{-5}$	8.51 $\times 10^{-5}$	2.13 $\times 10^{-4}$	5.02 $\times 10^{-4}$

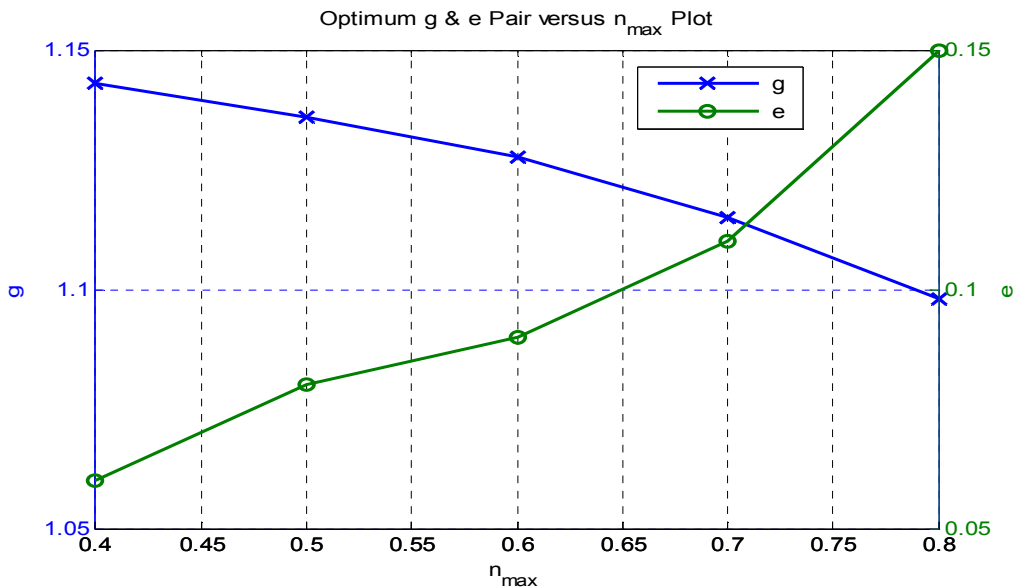


Figure 3 - 6: Optimum g & e Pair vs. n_{max} Plot

For a fixed n_{max} (0.5), maximum path-length error distribution over $g - e$ space is plotted in Figure 3 - 7, also the phase error variations with e for several g values is plotted in Figure 3 - 8. According to Figure 3 - 7, minimum path-length error occurs at a g value around optimum g calculated for $e = 0$ and in Figure 3 - 8, it is seen that optimum e is between 0 and 0.1.

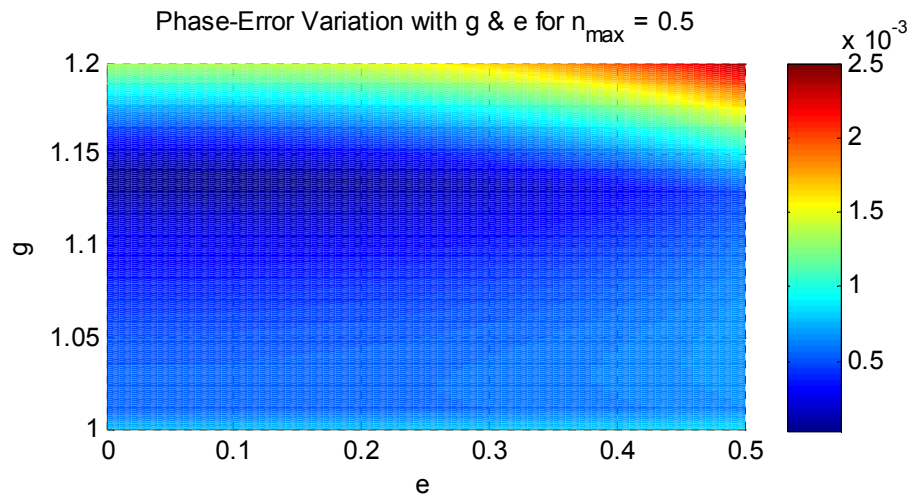


Figure 3 - 7: Phase-Error Variation with g & e for $n_{max}=0.5$

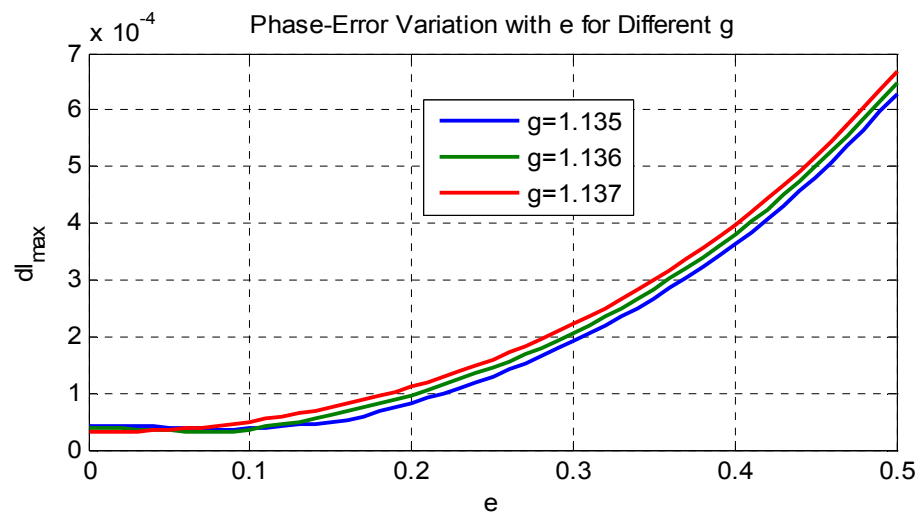


Figure 3 - 8: Phase-Error Variation with e for Different g

Considering all of the results, when searching for the optimum ϵ , scanning the values smaller than 0.2 would be sufficient. However, one should keep in mind that the circular beam contour also gives very good phase-error performance.

3.4 Relative Dielectric Constant of the Substrate – ϵ_r

Printed rotman lens design is suggested to reduce the size of the lens structure. As mentioned in the previous chapter, by using microstrip or stripline technology, the lens size can be scaled by the factor of $1/\sqrt{\epsilon_r}$.

In the parametric study of ϵ_r , 3 dielectric substrates and air-filled parallel-plate case ($\epsilon_r = 1$) are investigated. The chosen substrates are:

- Rogers RT/Duroid 5880 ($\epsilon_r = 2.2$)
- Rogers RO4003 ($\epsilon_r = 3.55$)
- FR-4 Epoxy ($\epsilon_r = 4.4$)

Given dielectric substrates are chosen since they are possible candidates for the lens manufacture. Other parameters of the substrates will be given and compared in the following chapter when explaining the material selection.

Effective dielectric constant (ϵ_{re}) of the transmission line is also used in the design equations. Therefore, in order to investigate the effects of ϵ_r , ϵ_{re} needs to be calculated. The detailed calculation procedure for ϵ_{re} is given in the appendix A. In the calculation procedure, the width of the transmission line is needed and it needs to be chosen in order to provide good impedance matching at the ports over the operating frequency bandwidth. The choice of the transmission line width will be explained in the following chapter. In this chapter, the calculation is not explained but the calculated values (Table 3 - 5) are used to calculate the optimum lens parameters and the path-length errors.

Table 3 - 5: Values of “ ϵ_r ” & “ ϵ_{re} ” for the chosen substrates

Substrate	ϵ_r	ϵ_{re}
Rogers RT/Duroid 5880	2.2	1.8637
Rogers RO4003	3.55	2.7677
FR-4 Epoxy	4.4	3.312

For a fixed n_{max} (0.5), optimum g and e values are computed and given in Table 3 - 6 together with the corresponding dl_{max} . In addition, the variation of optimum $g\&e$ pair with ϵ_r is given in Figure 3 - 9. According to the figure, it is seen that optimum g value increases with increasing ϵ_r .

Table 3 - 6: Optimum g&e Pair and dl for Different “ ϵ_r ”

ϵ_r	1	2.2	3.55	4.4
Optimum	g	1.136	1.147	1.15
	e	0.08	0.02	0.02
dl_{max}	3.10×10^{-5}	5.97×10^{-6}	2.34×10^{-6}	1.53×10^{-6}

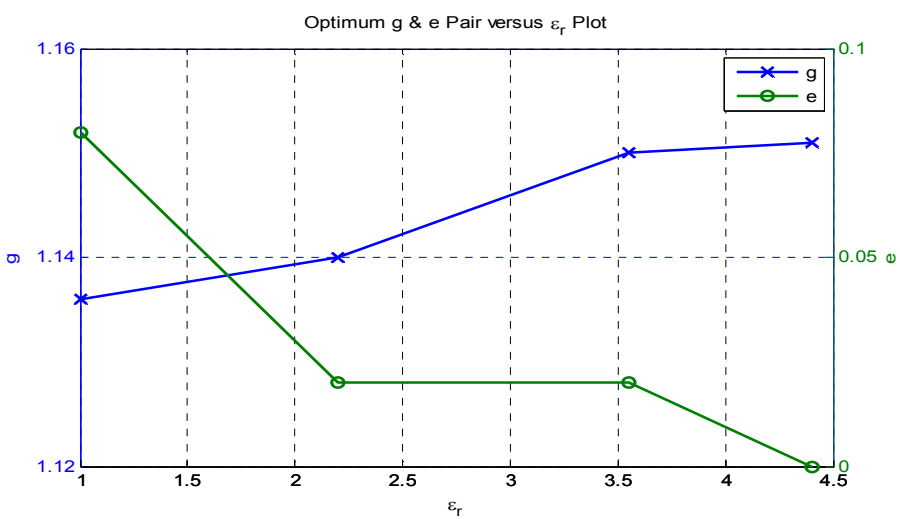


Figure 3 - 9: Optimum g & e Pair vs. ϵ_r Plot

In the view of the normalized path-length errors, from Figure 3 - 10, it can be said that dl_{max} decreases with increasing ϵ_r . Therefore, larger dielectric constants are more advantageous than smaller dielectric constants since the phase-error is reduced.

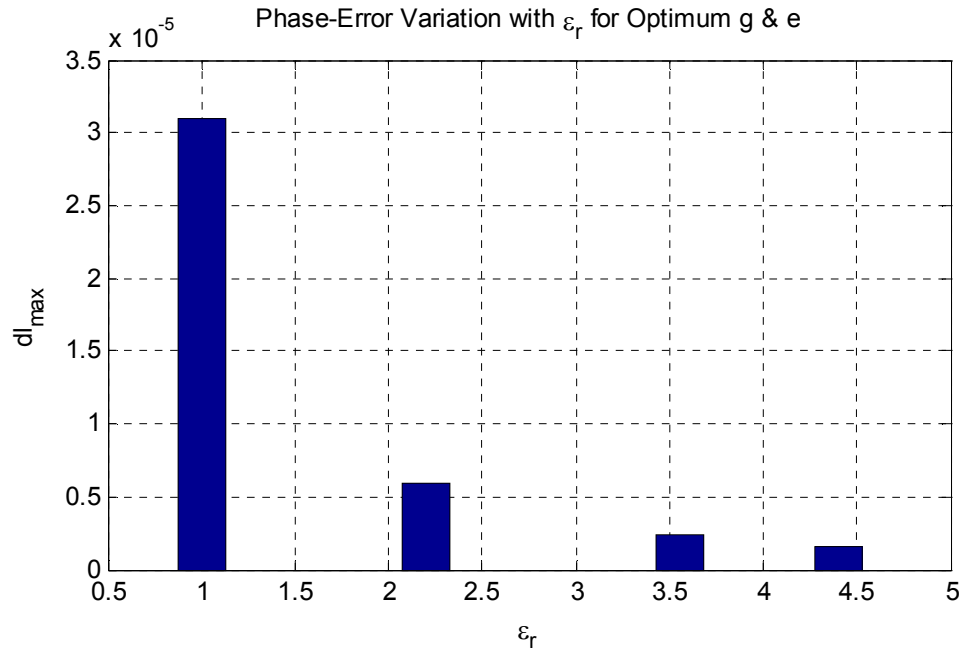


Figure 3 - 10: Phase-Error Variation with ϵ_r for Optimum g & e

To conclude the discussion about ϵ_r , effects on the lens contours are also investigated. Beam and lens contour variations with ϵ_r can be observed in Figure 3 - 11 and it is seen that ϵ_r has a scaling effect on the inner receiver (lens) contour. To be more precise, with increasing ϵ_r the lens contour shrinks.

The parameter ϵ_r directly affects the lens contour since it appears in the lens contour design equations (given in the previous chapter). Besides, since ϵ_r doesn't appear in the beam contour design equations, beam contour isn't affected by the changes in ϵ_r . However, since the optimum g and e values are changed with ϵ_r , the beam contour is also affected in order to realize the optimum lens design.

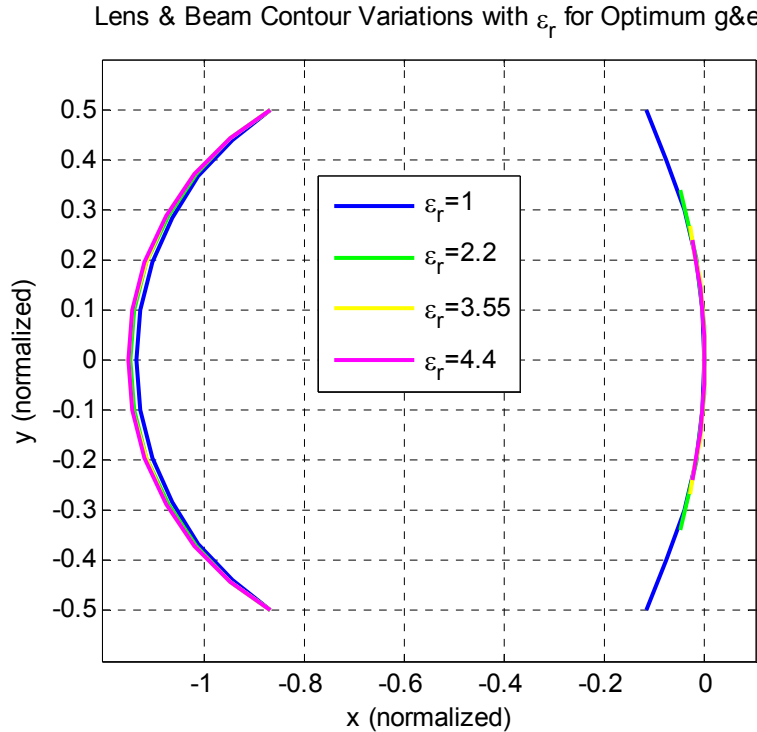


Figure 3 - 11: Lens & Beam Contour Variations with ε_r for Optimum g & e

3.5 Maximum Scan Angle (Off-Center Focal Angle) – α

Off-center focal angle, α is defined as the angle between on-axis focal point (G) and off-axis focal point (F_1 & F_2) as shown in Figure 2 - 6. In addition, since the scan angle is chosen as equal to the subtended angle of the beam contour, α also corresponds to the maximum scan angle of the lens structure.

In this parametric study, wide-angle characteristics of a Rotman lens structure is investigated for maximum scan angles from 20° to 60° for a fixed values of n_{max} (0.5) and ε_r (1).

To begin with, optimum g & e values are computed for different α and given in Table 3 - 7 together with the corresponding dl_{max} . By recalling the discussion about

the parameter g , optimum g values are also calculated from (3.1) and given in Table 3 - 8. Therefore, when the two tables are compared, theoretical “optimum g ” values are very close to real “optimum g ” values for small angles ($\alpha < 40^\circ$). However, for large angles ($\alpha \geq 40^\circ$), “optimum g ” values are found to be larger than the theoretical values and with increasing α , optimum g values diverge from the theoretical values. Thus, for large scan angles, the theoretical values cannot be used, so, the parametric study on g is essential. Besides, when e values are compared, it is observed that e values remain almost same for different values of α .

Table 3 - 7: Optimum g&e Pair and dl for Different “ α ”

α		20°	30°	40°	50°	60°
Optimum	g	1.056	1.136	1.270	1.495	1.895
	e	0.08	0.08	0.07	0.07	0.08
dl_{max}		1.14 $\times 10^{-5}$	3.10 $\times 10^{-5}$	6.18 $\times 10^{-5}$	8.75 $\times 10^{-5}$	9.39 $\times 10^{-5}$

Table 3 - 8: Optimum g Calculated from the Ruze's [5] Equation (3.1)

α	20°	30°	40°	50°	60°
Optimum “g” (calculated from (3.1))	1.061	1.137	1.244	1.381	1.548

In order to visualize the change in the optimum g values for different α , “Optimum g vs. α ” plot is given in Figure 3 - 12.

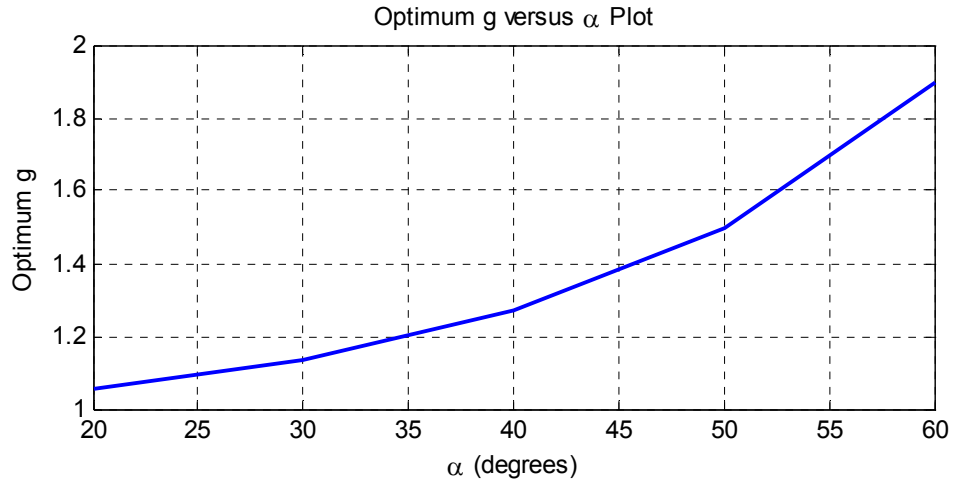


Figure 3 - 12: Optimum g vs. α Plot

To emphasize the phase-error variations for the maximum scan angle, the results are plotted in Figure 3 - 13. Thus, it can be observed that the maximum path-length error increases with increasing α . Therefore, for large angles, the conventional design approach [3] should be modified in order to improve the phase-error characteristics in wide-angle applications.

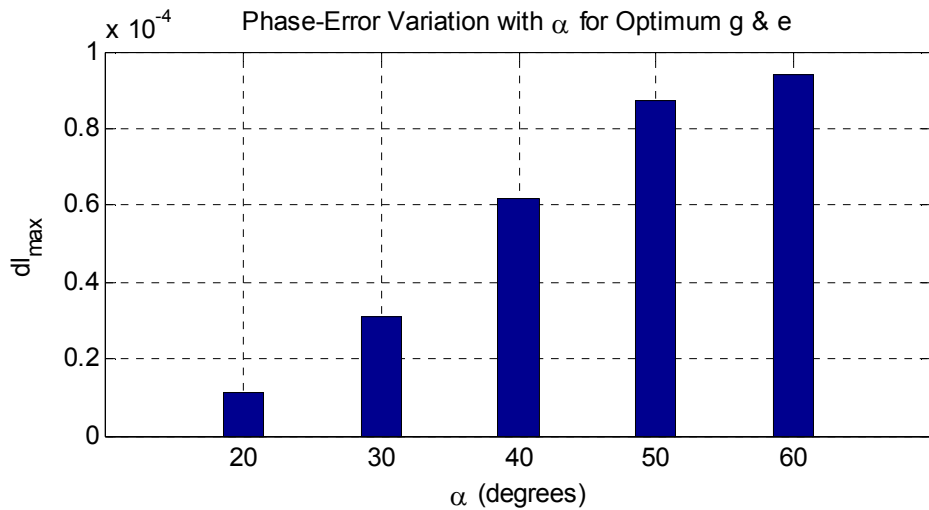


Figure 3 - 13: Phase-Error Variation with α for optimum g & e

To end the discussion about the maximum scan angle, effects on the lens contours are also investigated. Beam and lens contour variations with α can be observed in Figure 3 - 14. Thus, it is seen that the beam contour becomes extremely large for large angles compared to the inner receiver contour and the lens structure becomes infeasible to manufacture. This problem can be solved by choosing the scan angle different from the subtended angle of the beam contour and hence the beam contour can be shrunk to more feasible sizes even for large angles.

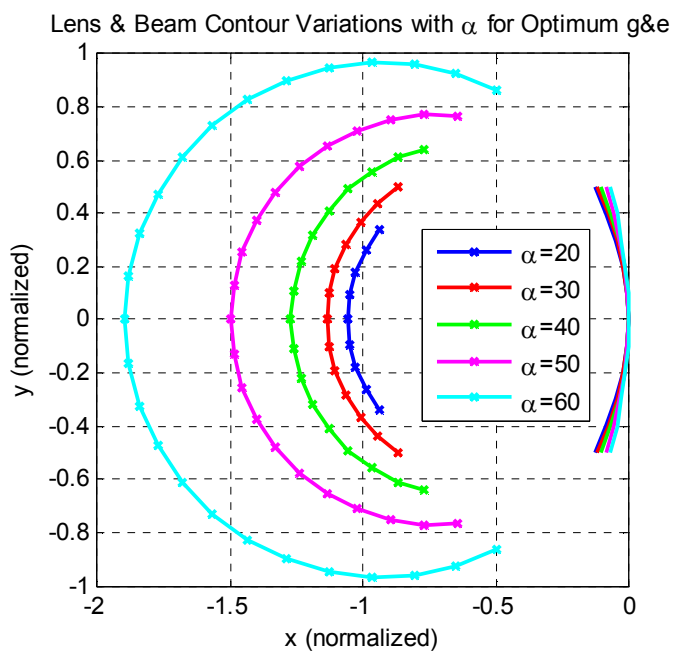


Figure 3 - 14: Lens & Beam Contour Variations with α for Optimum g & e

3.6 Off-Axis Focal Length – F

As a final discussion, the off-axis focal length is investigated. Off-axis focal length, F is the normalization factor used in the design procedure and all of the normalized coordinates are to be multiplied by F in order to get the real coordinates of the lens structure. Therefore, F is the parameter that determines the overall size of the lens.

When choosing focal length, the distance between the antenna elements should be taken into account. In the array design, the distance between antenna elements (d) is restricted by the grating lobe, namely, d is chosen in order to avoid grating lobes for all scan angles. Therefore, since the grating lobe appears at $d = \frac{\lambda}{1+\sin\theta}$, the chosen distance should be as given in (3.2) where λ_{min} is the minimum wavelength (λ at the highest frequency) and θ_{max} is the maximum scan angle.

$$d < \frac{\lambda_{min}}{1 + \sin \theta_{max}} \quad (3.2)$$

In Rotman lens design, the distance between antenna elements (d) and the other related design parameters are as sketched in Figure 3 - 15. Hence, d can be written in terms of the design parameters n_{max} , F and N , where N is defined as the number of array elements:

$$d = \frac{2 \times n_{max} \times F}{(N - 1)} \quad (3.3)$$

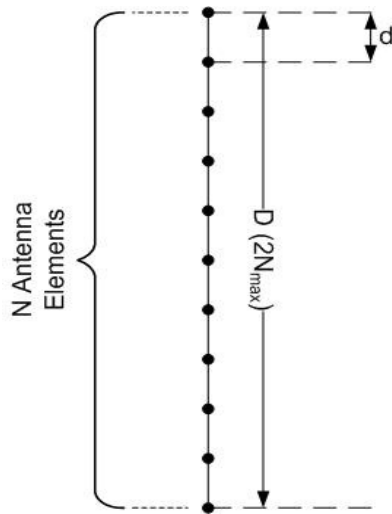


Figure 3 - 15: Sketch of the Antenna Array

By combining the equations (3.2) and (3.3), the limitation on F is obtained:

$$F < \frac{\lambda_{min}}{1 + \sin \theta_{max}} \times \frac{(N - 1)}{(2 \times n_{max})} \quad (3.4)$$

Therefore, with (3.4), an upper limit for F is introduced. For the values bigger than that upper bound value of F , grating lobes will appear in the radiation pattern of the antenna array.

There is no lower bound for F and larger F means larger lens and larger lens will cause more insertion loss. Besides, since F is the normalization factor, path-length errors will also increase for larger F . Thus, it is reasonable to choose the off-axis focal length as small as possible. However, there are practical limitations on how small F can be chosen. These practical limitations and the choice of F will be discussed in detail in the following chapter when explaining the implementation of the lens.

In conclusion, the discussion on the effects of the design parameters is completed with F . Procedures for how to choose the design parameters in order to implement a Rotman lens with specific requirements will be explained and simulation results will be given in the following chapter of the thesis.

CHAPTER 4

IMPLEMENTATION AND SIMULATION RESULTS

In order to verify the operational properties of Rotman lens, it is decided to implement a microstrip Rotman lens. The reasons for choosing the microstrip implementation are: easy and fast fabrication process compared to waveguide lens implementation, reduced size due to the permittivity of substrate (ϵ_r).

In this chapter, step-by-step implementation procedure for a microstrip Rotman lens will be explained in detail. Afterward, the simulation results of the implemented Rotman lens will be given.

4.1 Microstrip Rotman Lens Implementation

In the beginning, design requirements for the microstrip Rotman lens should be decided. In this thesis, the microstrip Rotman lens is implemented in order to satisfy the requirements given in Table 4 - 1.

Table 4 - 1: Design Requirements

Frequency Band	8 GHz – 16 GHz
Angle Scan	-30° to +30°
Number of Beam Ports	13
Number of Array Ports	11

In microstrip Rotman lens implementation procedure, first step is to select the dielectric substrate since it is directly used in the design equations. Then, after inserting the dielectric substrate properties in the design equations, design parameters are chosen so that the path-length error is minimized. Afterward, microstrip matching section connecting the transmission lines to the lens cavity should be implemented. Then, in order to reduce the reflections from the sidewalls, sidewall design should be modified properly. Finally, the transmission lines between the receivers and the array elements must be arranged so that the lengths derived from the design equations are realized.

4.1.1 Selection of the Dielectric Substrate

For the selection of the dielectric substrate, dielectric material and thickness of the substrate must be chosen. In order to decide on the material to be used, properties of the candidate materials are investigated with the advantages and disadvantages. Three different materials are compared in Table 4 - 2. From the parametric study in the previous chapter, it is known that the greater the dielectric permittivity (ϵ_r) is, the lesser the maximum path-length error becomes. Also, with greater permittivity, the lens size becomes smaller. Therefore, choosing the dielectric material with the highest permittivity is convenient. However, the material with the highest permittivity, FR-4 has unreliable permittivity value and its permittivity varies with the frequency as seen in Figure 4 - 1. Hence, as a dielectric material, the material with the second highest permittivity, Rogers RO4003 is chosen.

Table 4 - 2: Properties of Several Dielectric Materials

Material	ϵ_r	Loss Tangent	Advantage	Disadvantage
FR-4	4.4	0.02	- Easy to fabricate	- Unreliable relative permittivity - Rapidly varying permittivity with frequency (Figure 4 - 1) - High loss
Rogers RO4003	3.55	0.0027	- Easy to fabricate - Low loss compared to FR-4 - High permittivity	- High loss compared to 5880
Rogers RT/Duroid 5880	2.2	0.0009	- Low loss	- Hard to fabricate (soft material) - Low permittivity

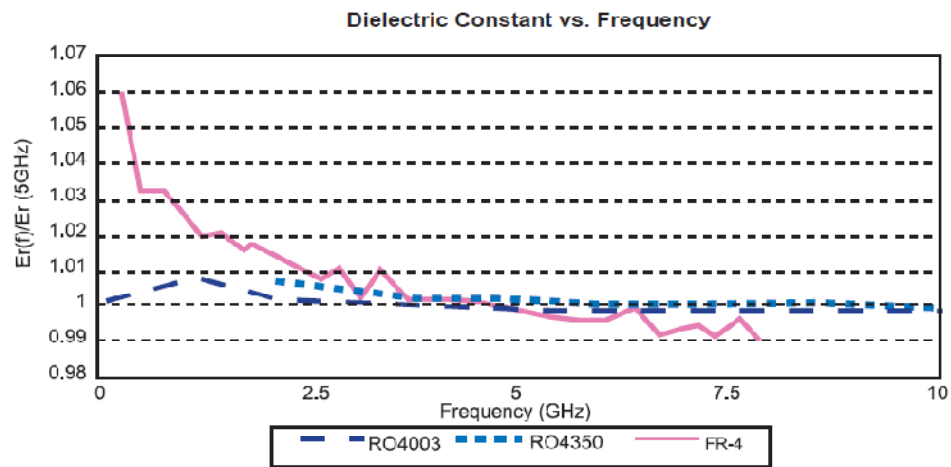


Figure 4 - 1: Frequency Response of Different Dielectric Materials (From [20])

After the material selection, substrate thickness should be decided. Dielectric substrates are manufactured in standard thicknesses: 0.008", 0.020", 0.032", and 0.060". In order to accelerate the fabrication process of the lens, available RO4003 substrate with 0.020" thickness is chosen.

4.1.2 Choice of Design Parameters

The design equations for the microstrip Rotman lens requires the design parameters α , n , ϵ_r , ϵ_{re} , g , e and F to be defined before the implementation. The focal angle, α is chosen as equal to the maximum scan angle which is 30° . Since the number of array elements is constrained by the design requirements, the locations of the array elements (n) are determined by the normalized array aperture (n_{max}). In other words, n for each array elements can be calculated from n_{max} knowing the number of array elements. Therefore, the design parameters to be chosen reduce to n_{max} , ϵ_r , ϵ_{re} , g , e and F .

The relative permittivity of the dielectric substrate (ϵ_r) is given as 3.55. However, the effective dielectric constant of the transmission lines (ϵ_{re}) needs to be calculated and for this calculation, transmission line width is needed. The line width that gives 50Ω matching at the ports is found to be 1.07 mm for the chosen dielectric substrate. Then, by using the transmission line width and the dielectric substrate properties, the effective dielectric constant (ϵ_{re}) is calculated with the method given in appendix A. Hence, the effective dielectric constant (ϵ_{re}) is found to be 2.7677.

At first, optimum $g\&e$ pairs are computed for different n_{max} and then the corresponding path-length errors are examined. Therefore, after this parametric study of g , e and n_{max} , the parameters are chosen as given in Table 4 - 3. These parameters are not frequency-dependent. However, the choice of the focal length, F depends on the operating frequency band. Therefore, in order to determine F , frequency band needs to be specified.

Table 4 - 3: Chosen Design Parameters

g	1.15
e	0.02
n_{max}	0.5
F	120 mm

The procedure for selecting appropriate F was roughly explained in the previous chapter and (4.1) is derived for the upper bound of F where N is the number of antenna elements, λ_{min} is the wavelength at the maximum operating frequency (16 GHz) and θ_{max} is the maximum scan angle. Therefore, from the requirements, θ_{max} is equal to 30° and λ_{min} is calculated as 18.75 mm. Hence, by substituting λ_{min} and θ_{max} into the formula, the maximum value of F is equal to 125 mm. In the previous chapter, it is stated that F should be chosen as small as possible. However, since the antenna connectors require a certain distance between them in order to make measurements possible, F cannot be chosen very small. The distance between the array elements is $0.1F$ due to the parameter definition in Rotman lens design procedure. Therefore, considering all of the conditions, F is chosen as 120 mm, hence the distance between the antennas becomes 12 mm.

$$F < \frac{\lambda_{min}}{1 + \sin \theta_{max}} \times \frac{(N - 1)}{(2 \times n_{max})} \quad (4.1)$$

4.1.3 Microstrip Matching

Design parameters are chosen in the previous section and by substituting the parameters into the design equations derived in Chapter 2, the locations of the beam & array ports' phase centers are found. In order to realize the lens structure, a matching section connecting the transmission lines to the lens cavity is required in order to match the lens section to 50Ω ports.

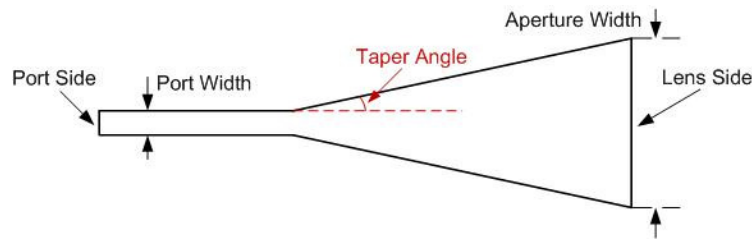


Figure 4 - 2: Matching Section with Microstrip Linear Taper

For the matching section, microstrip linear tapers are used as seen in Figure 4 - 2. Taper angle is the significant parameter in linear taper design and it is chosen in order to minimize the return loss at both ports (port & lens side) over the frequency band. In [21], it is suggested that the taper angle should be smaller than 12.5° . Therefore, it would be a good start to investigate the angles smaller than 12.5° . Thus the taper angles from 4° to 12° are examined by the parametric sweep of the taper angle. A linear matching section is modeled and simulated in the simulation program HFSS [22]. Return loss (S_{11}) variations with the taper angle over the frequency band are investigated and the maximum value of S_{11} over the whole frequency band is plotted in Figure 4 - 3. As seen in the figure, for the taper angles smaller than 6° , S_{11} values remain below -20 dB. Therefore, choosing taper angles as 4° - 5° is convenient for the matching section.

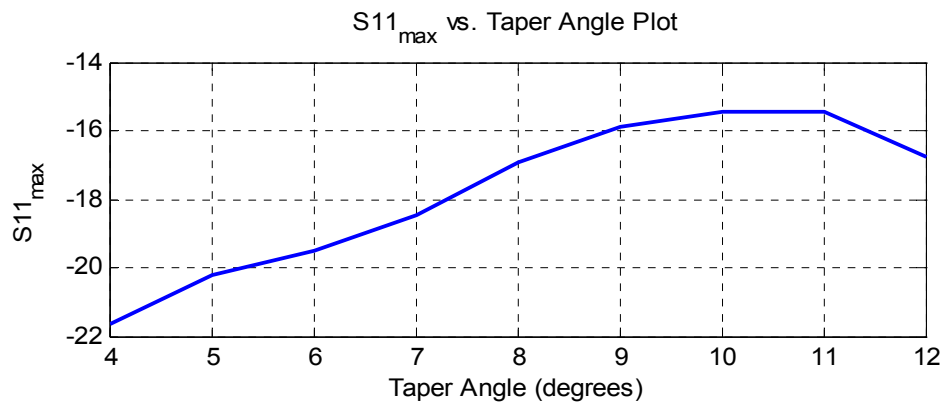


Figure 4 - 3: $S_{11\max}$ vs. Taper Angle Plot for the Microstrip Linear Taper

After determining the appropriate taper angle for the matching section, port apertures at the lens side should be specified. In Figure 4 - 4, calculated phase center locations for the beam and array ports are given. Therefore, the ports with the matching section should be placed in order to have the phase centers of the ports coincide with the calculated locations. The phase centers of the linear tapered matching section are assumed to locate in the middle of the aperture.

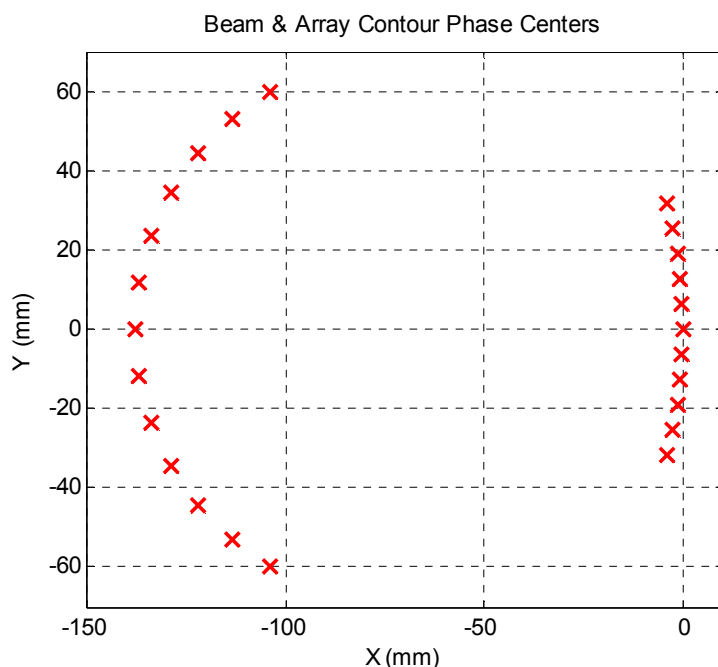


Figure 4 - 4: Locations of the Phase Centers

Before placing the ports to the specified locations, size of the apertures should be chosen so that there will be no gap between the successive ports. If there are gaps between the successive ports, there will be undesired reflections which may distort the transmission. Hence, the apertures of the beam and array ports are determined as 5.4 mm and 4.78 mm, respectively. After the aperture sizes are determined, using the taper angles 4° and 5° respectively for the beam and array ports, the design of the matching section is completed.

4.1.4 Port Pointing

The design equation gives the port phase centers' locations, however the angle at which the ports will be placed is an issue to be discussed. One approach is to place the ports normal to the contours where the contours are formed by combining the calculated phase center locations. The other approach is to place the ports at an angle so that they point to the center of the opposite contour. Both approaches are discussed in [23] and it is deduced that the center pointing is a good approximation for most practical lens designs. Therefore, in the implemented lens, the ports are placed in order to point toward the center of the opposite contour as shown in Figure 4 - 5.

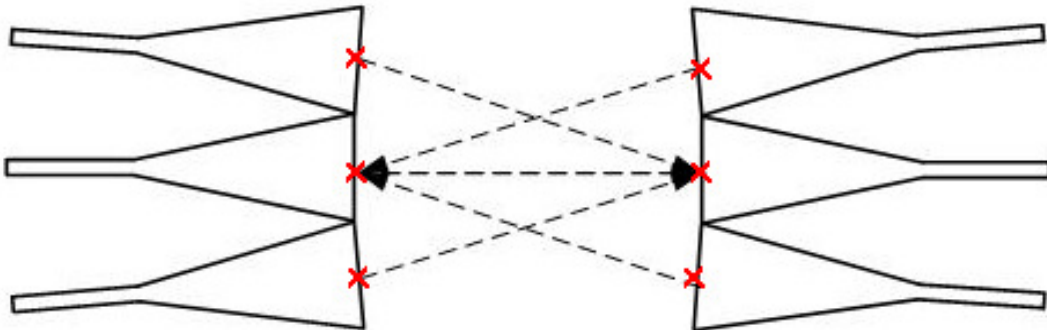


Figure 4 - 5: Beam & Array Ports' Allocation

4.1.5 Sidewall Design

In Rotman Lens design, beam and array contours are defined by the design equations. However, the sidewall connecting the contours is not defined and needs to be taken into account since it reflects the signal as a secondary path (Figure 4 - 6) which interfere the transmitted signal. In parallel-plate/waveguide Rotman lenses, standard microwave absorbent materials can be used to absorb the power at the

sidewalls. Nevertheless, in microstrip/stripline lenses, the absorbers designed for the free space is inappropriate.

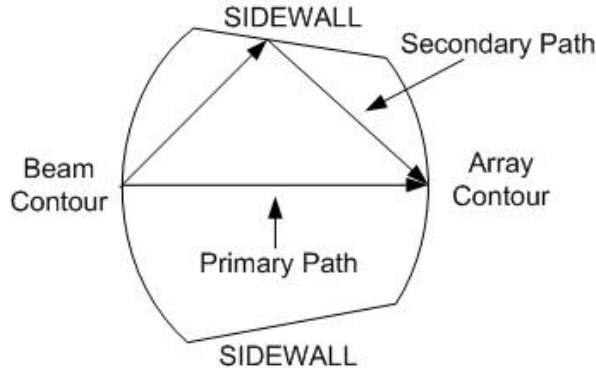


Figure 4 - 6: Sidewall Interference

In history, there were several techniques developed for the sidewall absorption of the microstrip Rotman lenses [23, 24]. The simplest approach is to use dummy ports at the sidewalls.

In this thesis, dummy port approach is used for the sidewall absorption with dummy ports pointing to the center of the opposite lens contour. In the implemented lens, 9 dummy loads are placed at each sidewall.

4.1.6 Transmission Line Length Arrangement

The lengths of the transmission lines between the receiving probes and the array elements are defined by the design equations in order to achieve the required phase distribution on the antennas. The design equations give the length difference between each line (W) and the line through the origin (W_0). Hence, the length of the transmission line at the origin should be fixed and the other lines should be arranged accordingly.

Transmission line lengths are arranged in ADS [25] software using appropriate built-in line bending sections as shown in Figure 4 - 7.

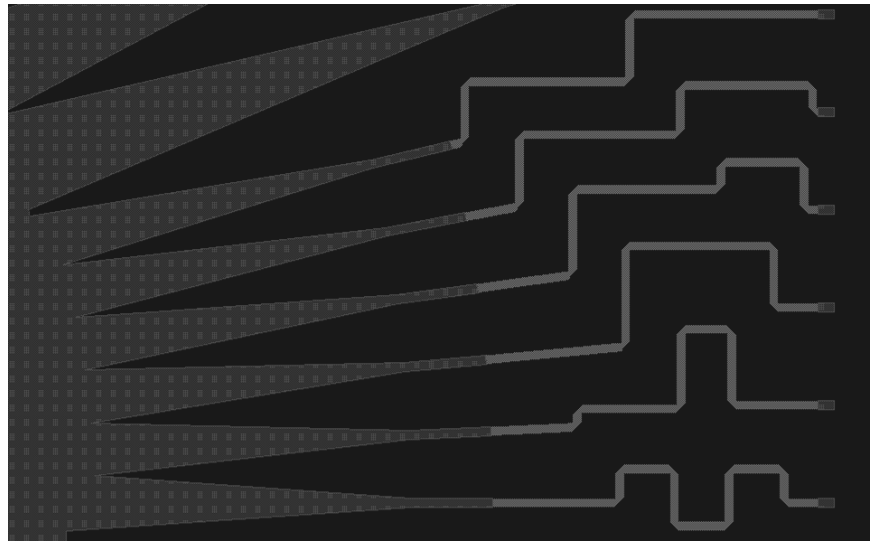


Figure 4 - 7: Line Bendings Implemented in ADS

4.1.7 Implemented Model

The implemented model for the microstrip Rotman lens is given in Figure 4 - 8. The overall size of the lens is 319 mm by 320 mm. Beam ports can be seen on the left side of the figure and the array ports can be seen on the right side. There are 13 beam ports which provide beam scanning from -30° to 30° with 5° resolution. There are 11 array ports displaced 12 mm apart from each other which makes the total array aperture 120 mm. In addition, there are 9 dummy ports on each sidewall which makes overall 18 dummy ports. Therefore, in total, there are 42 ports.

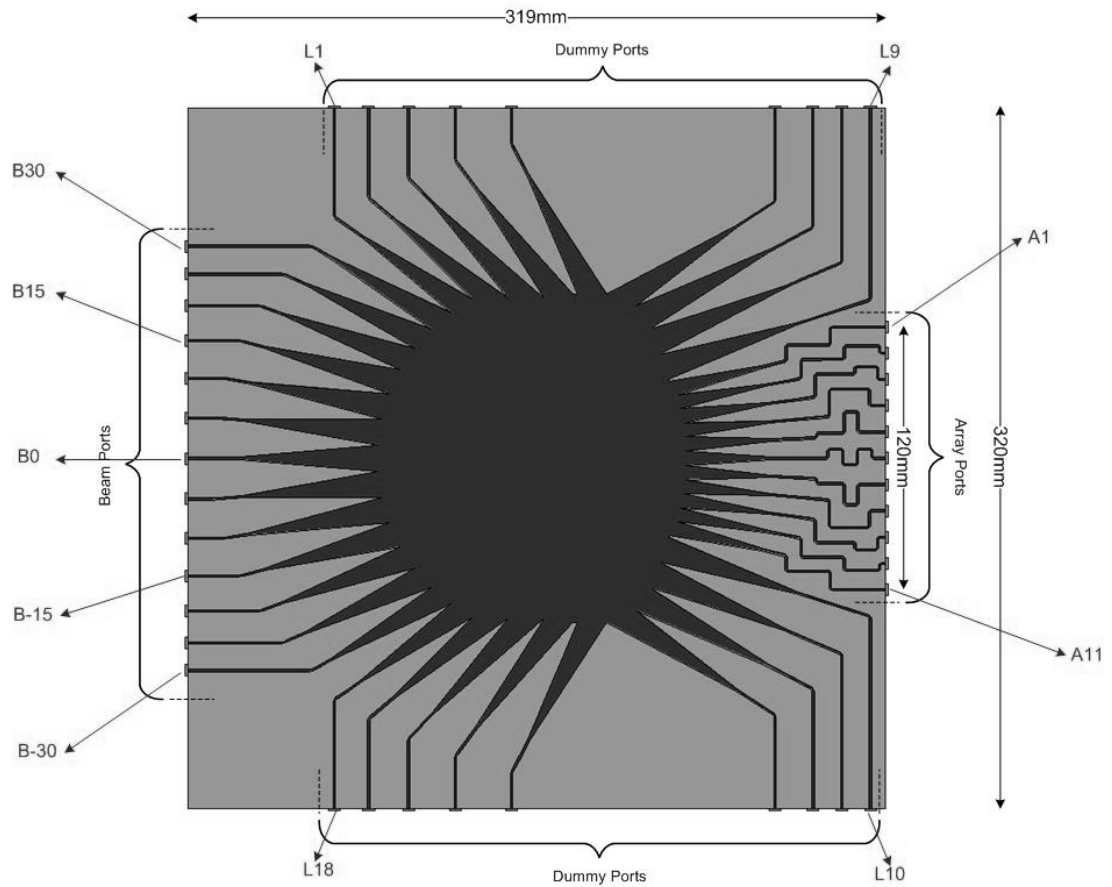


Figure 4 - 8: Implemented Microstrip Rotman Lens Model

The beam ports are numbered according to their placement angles as noted in Figure 4 - 8 while array ports and dummy ports are numbered in sequence. In the following section, the simulation results that will be given and this numbering convention will be used for the ports.

4.2 Simulation Results

The model is simulated in the electromagnetic simulation program HFSS [22] and 42 by 42 S-matrix is obtained. Significant results obtained from S-matrix will be presented in this section.

4.2.1 Return Loss Performance

Return loss performance of beam and array ports is investigated. “S11 vs. Frequency” plots of beam and array ports are given in Figure 4 - 9 and Figure 4 - 10, respectively. Hence, beam ports and array ports have S11 lower than -10 dB over the whole frequency band and these levels are acceptable for an octave band operating microstrip structure.

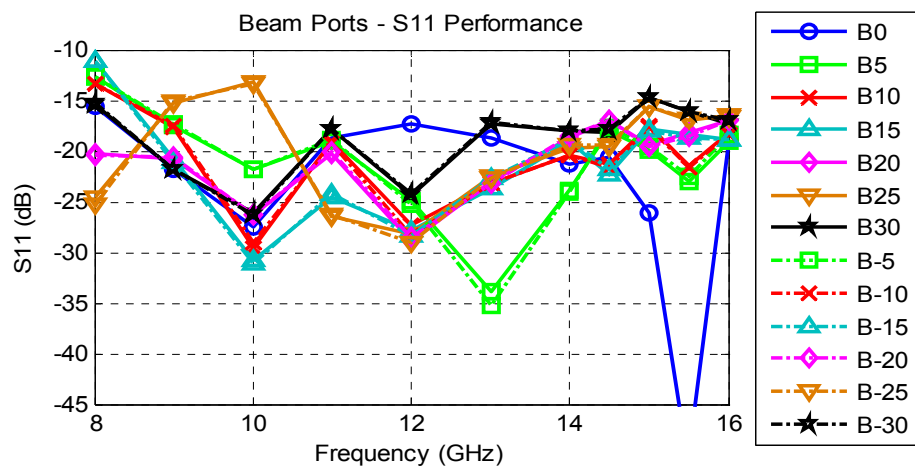


Figure 4 - 9: Return Loss of the Beam Ports

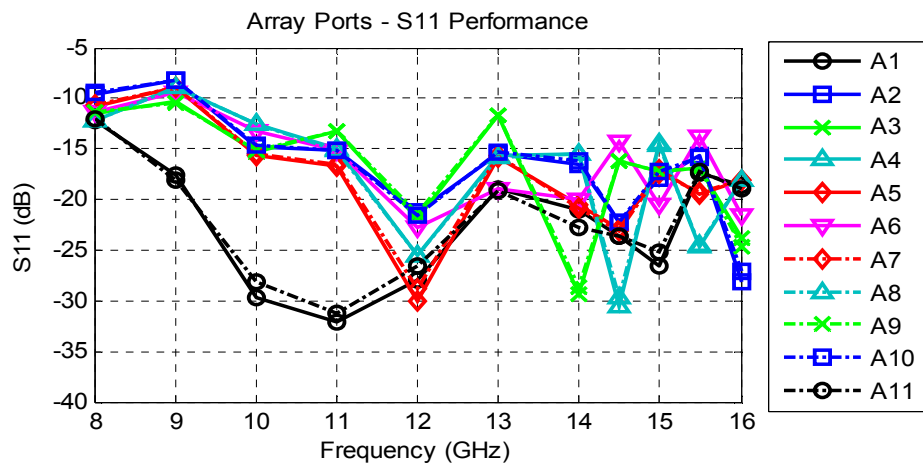


Figure 4 - 10: Return Loss of the Array Ports

4.2.2 Coupling between Ports

In microstrip structures, coupling between the lines could cause problems. Therefore, in this design since the transmission lines are implemented close to each other, coupling effects should be considered.

In order to observe the coupling effects between the beam ports, coupling between B0 and the other beam ports is plotted in Figure 4 - 11 and coupling between the two adjacent beam ports is plotted in Figure 4 - 12. Hence, at the beam contour side, the coupling levels remain below -15 dB.

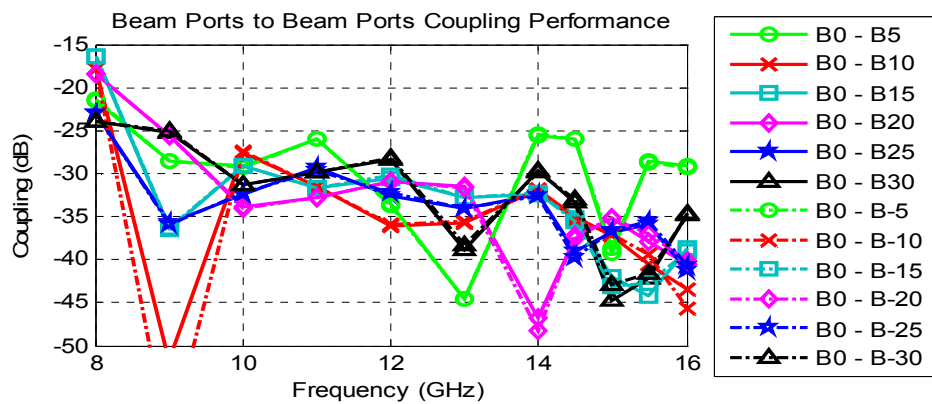


Figure 4 - 11: Coupling between the Beam Ports

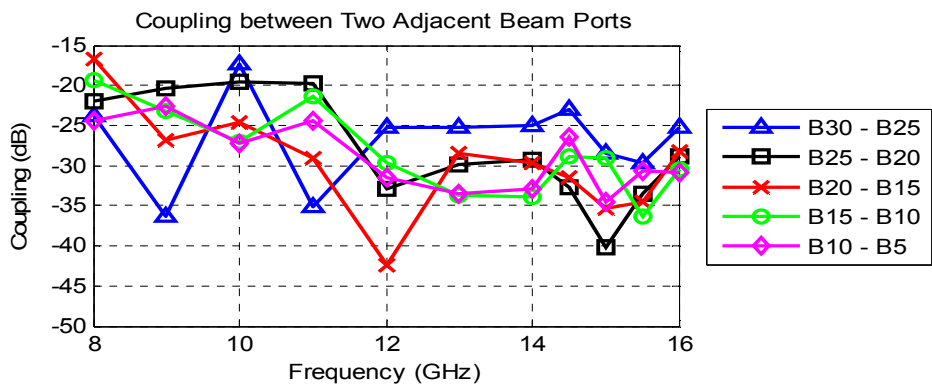


Figure 4 - 12: Coupling between the Two Adjacent Beam Ports

For the array ports, coupling effects become more important since the distances between the transmission lines connecting adjacent ports are much smaller than the beam ports' case. The coupling between A6 and the other array ports can be observed in Figure 4 - 13 and coupling between the two adjacent array ports can be observed in Figure 4 - 14. It is concluded that the coupling levels of the array ports are worse compared to the beam ports as expected since the separation between the transmission lines of array ports are much smaller than that of beam ports. However, these coupling levels remain below -10 dB and this level should be sufficient not to affect the lens performance.

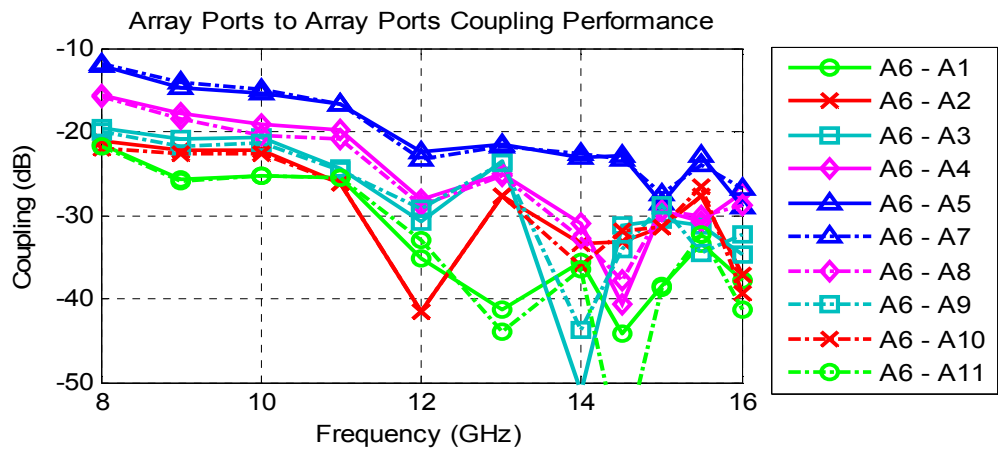


Figure 4 - 13: Coupling between the Array Ports

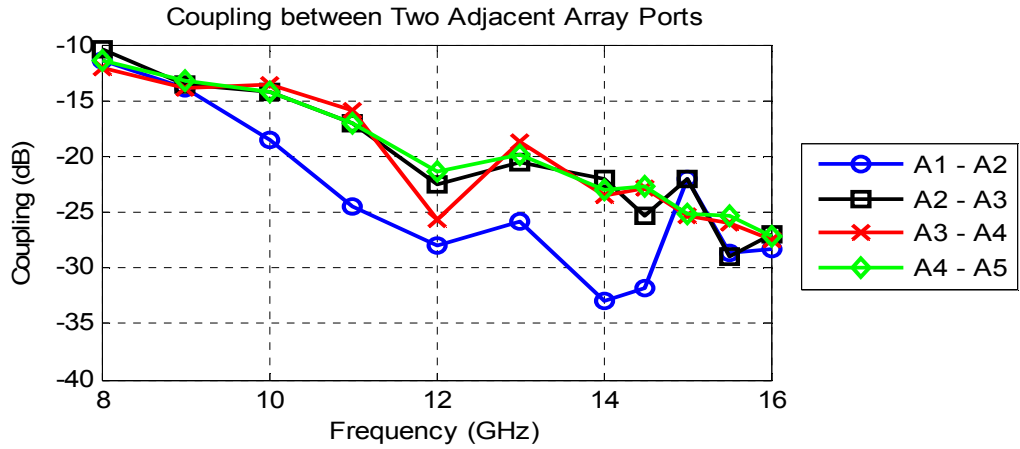


Figure 4 - 14: Coupling between the Two Adjacent Array Ports

In order to observe the lost power transmitted to the dummy ports, coupling between the dummy ports and B0 is plotted in Figure 4 - 15 and the coupling between the dummy ports and A6 is also plotted in Figure 4 - 16. Since the dummy ports, L6 to L9 are pointing to the center of the beam contour, the coupling levels between B0 and dummy ports are higher for these ports. On the contrary, since the dummy ports, L1 to L5 are pointing to the center of the array contour, the coupling levels between A6 and the dummy ports are higher for the ports L1 to L5, in this case.

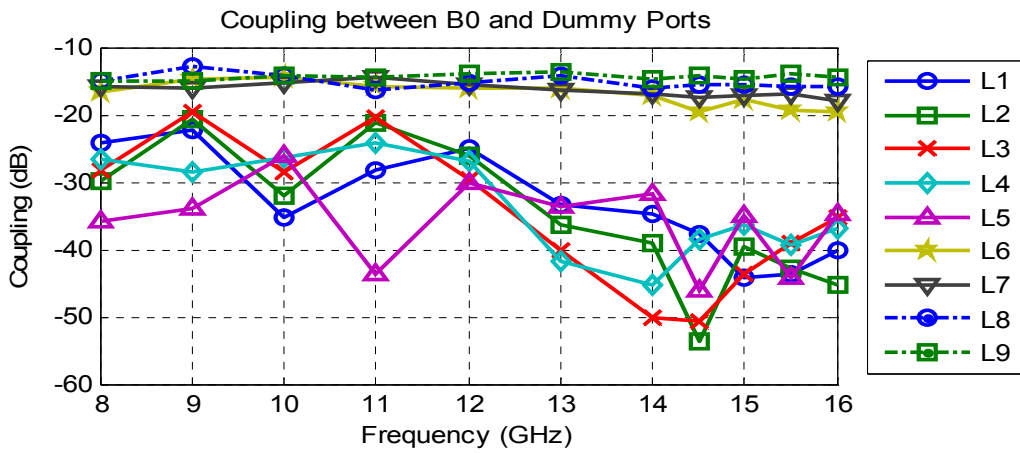


Figure 4 - 15: Coupling between B0 and the Dummy Ports

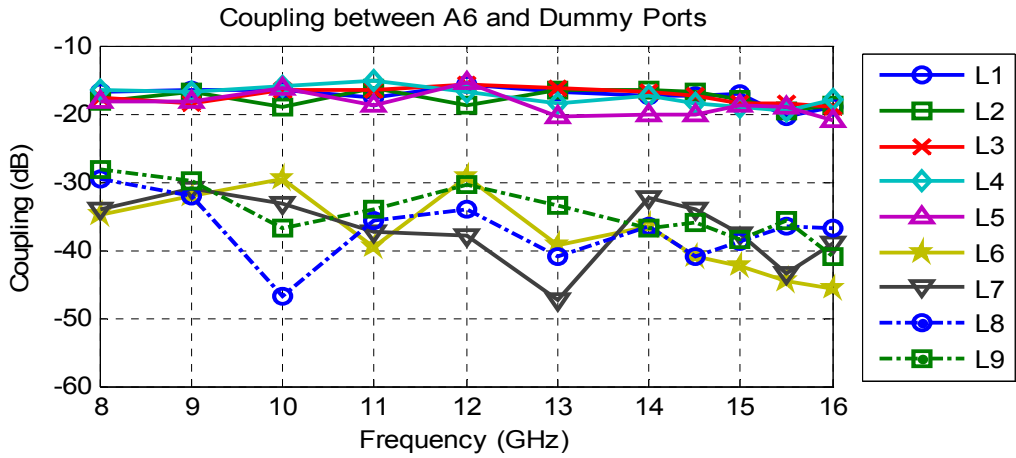


Figure 4 - 16: Coupling between A6 and the Dummy Ports

4.2.3 Amplitude and Phase Distributions over the Array Elements

In Rotman lens design, design equations are derived so that the desired phase distribution is obtained over the array elements. Amplitude distribution over the array aperture is not concerned in the design procedure. However, since deviations on the amplitude distribution could affect the sidelobe levels of the radiation pattern, amplitude distribution should be checked in order not to have high sidelobe levels.

Insertion loss from a certain beam port to the antenna elements is plotted and amplitude distribution over the array aperture is obtained. With the excitation from the beam port, B0, the amplitude distribution over antenna elements is plotted in Figure 4 - 17 for 3 different frequencies. For the excitation from B15 and B30, the amplitude distribution plots are given in Figure 4 - 18 and Figure 4 - 19, respectively. By comparing these plots, it is seen that the amplitude distributions deviate from the flat response as excitation goes from the beam port B0 to B30. However, the difference between the maximum and minimum values of S21 is at most 5 dB which does not significantly increase the sidelobe levels.

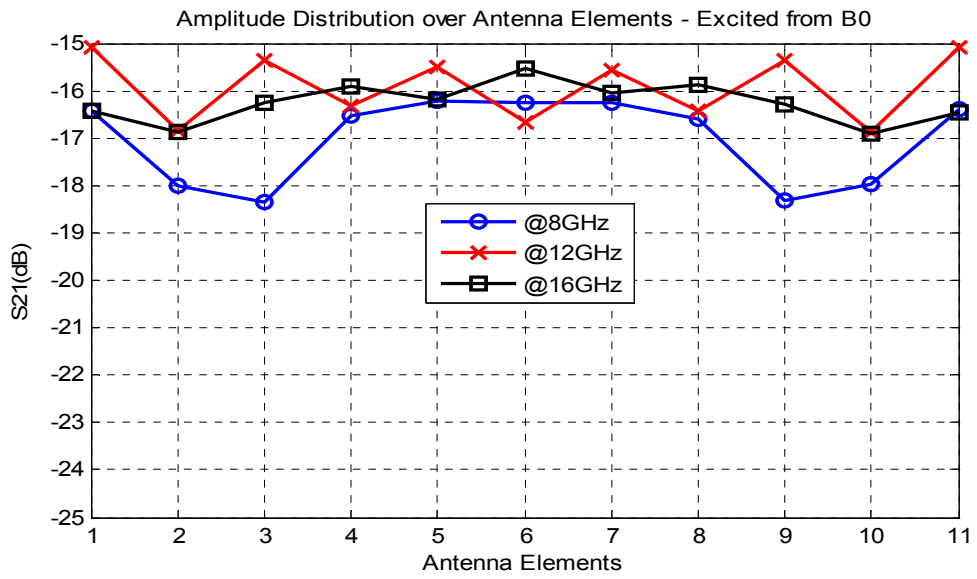


Figure 4 - 17: Amplitude Distribution over Antennas excited from B0

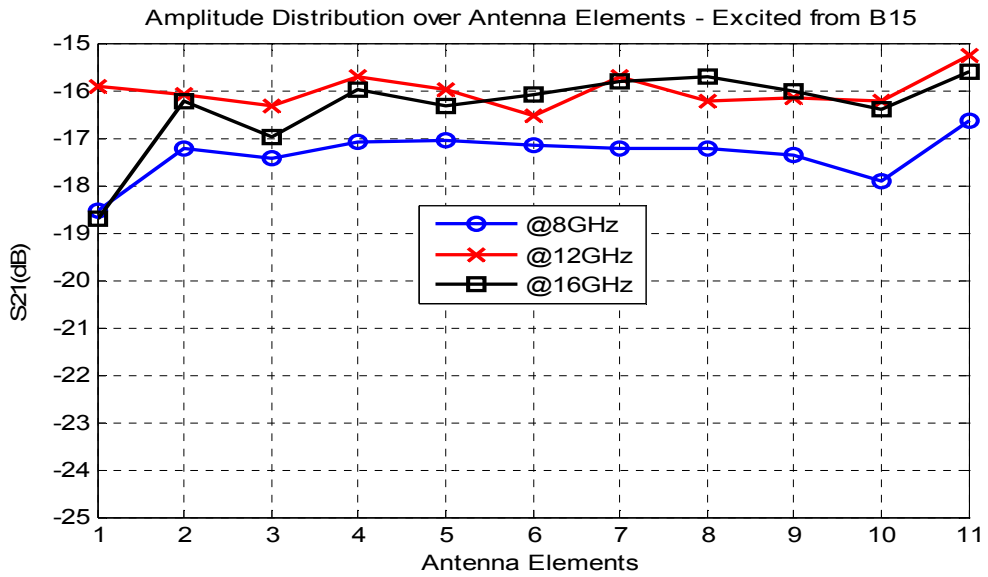


Figure 4 - 18: Amplitude Distribution over Antennas excited from B15

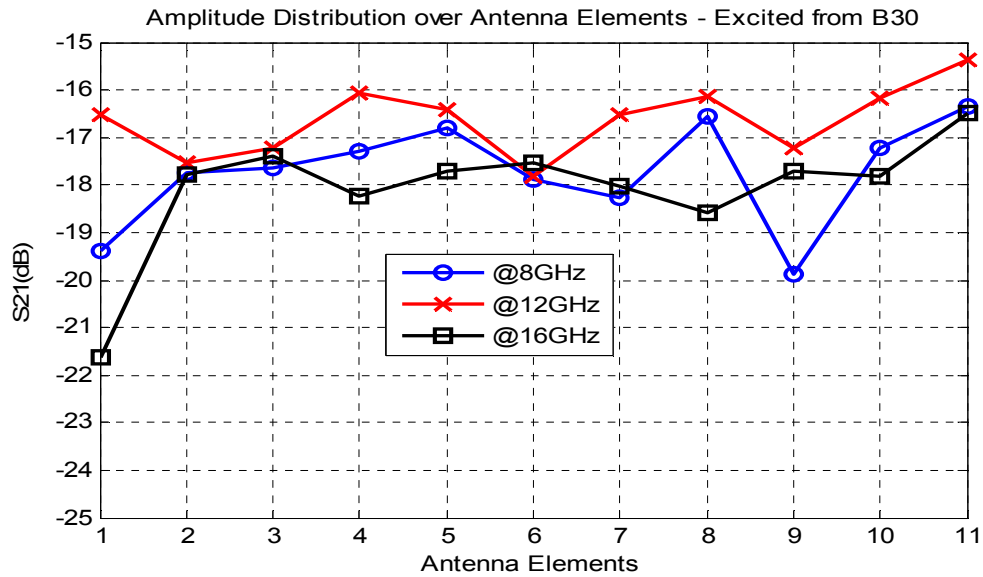


Figure 4 - 19: Amplitude Distribution over Antennas excited from B30

After the inspection of the amplitude distribution, phase distributions are also investigated. Insertion loss phases are plotted with respect to the distributed antenna elements for 3 different frequencies. The plots for the excitation from beam ports B0, B15 and B30 are given in Figure 4 - 20, Figure 4 - 21 and Figure 4 - 22, respectively. Therefore, it is observed that for all excitations, the phase distributions are very similar for all frequencies with the exception of a phase offset. When all figures are considered, it is seen that the slope of the phase distributions increases with increasing scan angle. In addition, from Figure 4 - 21 and Figure 4 - 22, it is observed that the phase slope also increases with increasing frequency for each excitation. Besides, for the excitation from the center beam, B0, it can be said that the distribution is symmetrical with respect to the center antenna element, A6.

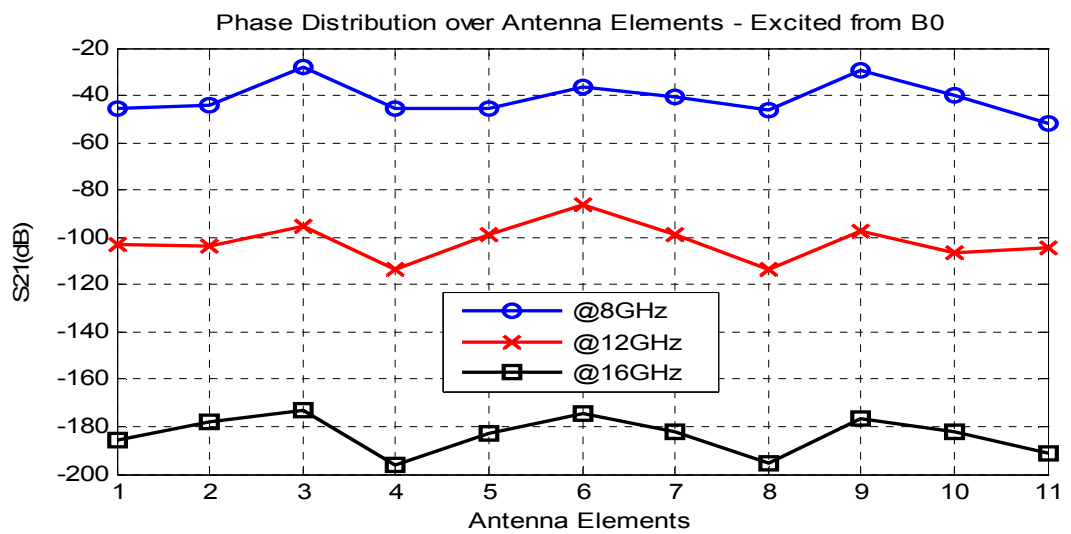


Figure 4 - 20: Phase Distribution over Antennas excited from B0

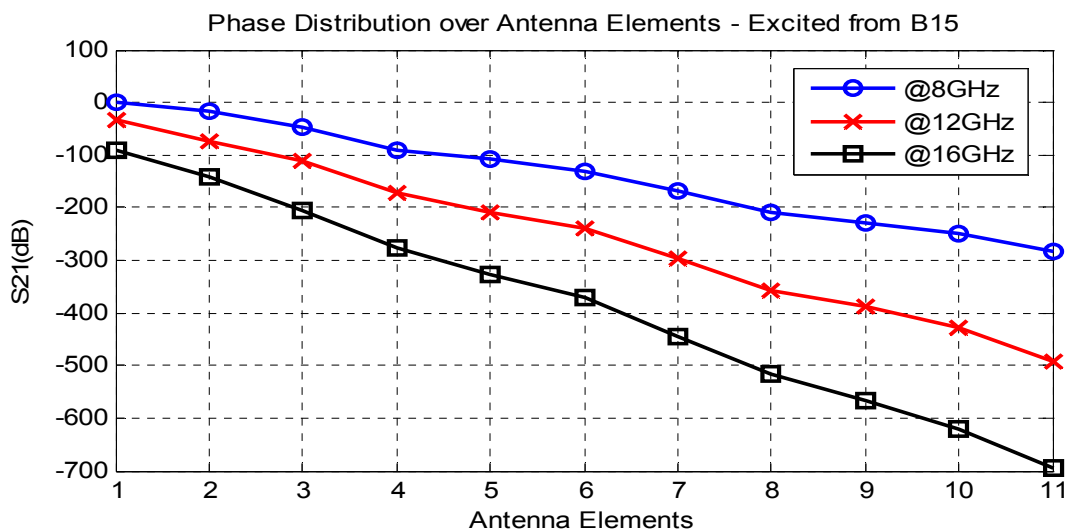


Figure 4 - 21: Phase Distribution over Antennas excited from B15

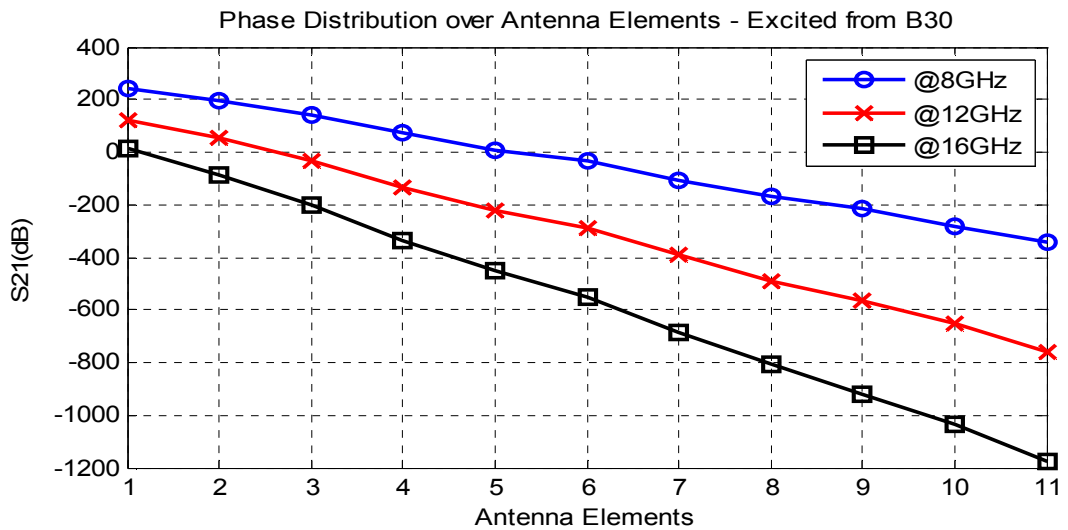


Figure 4 - 22: Phase Distribution over Antennas excited from B30

4.2.4 Array Factor Calculations

Scanning capabilities of the implemented Rotman lens are examined by calculating the array factor using the insertion losses (S21) from beam ports to the array ports. In order to calculate the array factor, array elements are placed in the coordinate systems as shown in Figure 4 - 23. Since the implemented lens provides one dimensional scan, array factor will be in terms of the azimuth angle, φ .

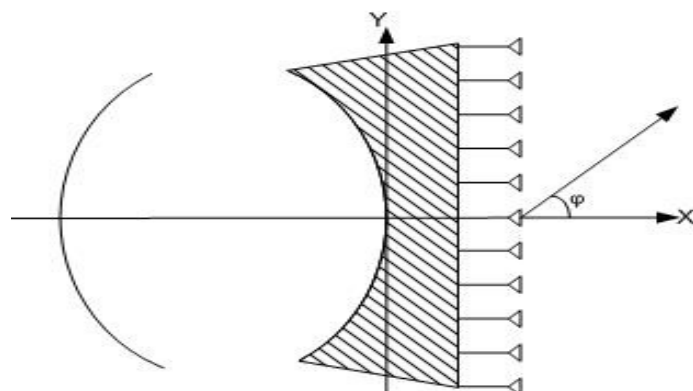


Figure 4 - 23: Array Placement According to the Coordinate Systems

For the array factor calculation, (4.2) is used where N is the number of array elements, $S21_n$ is the complex value of the insertion loss from the beam port of interest to the n^{th} array element and d_n is the distance of the n^{th} element from the x-axis.

$$AF = \sum_{n=1}^N S21_n \times e^{j \cdot \sin(\varphi) \cdot k \cdot d_n} \quad (4.2)$$

By substituting insertion losses obtained from the simulation into (4.2), the array factor is calculated for each beam port excitation. The calculated array factors of all beam ports for one frequency are plotted on the same plot with all array factors normalized with respect to the peak of the array factor corresponding to the boresight beam. Moreover, plots are given in Figure 4 - 24, Figure 4 - 25 and Figure 4 - 26 for the frequencies 8, 12 and 16 GHz, respectively. Therefore, the scanning capabilities of the implemented lens are verified. Besides, from the figures, it is observed that the peak values of the array factor decrease from the beam ports B0 to B30, in general.

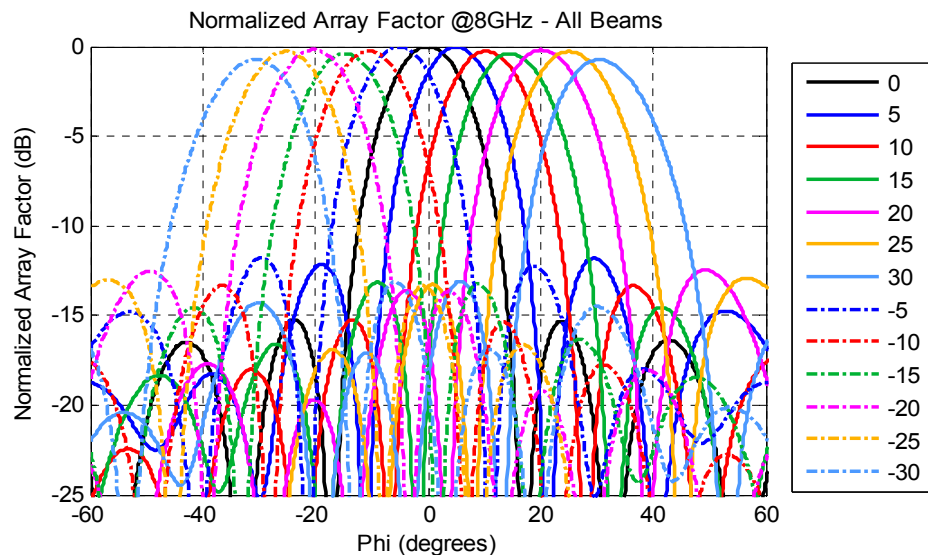


Figure 4 - 24: Normalized Array Factors of All Beams at 8 GHz

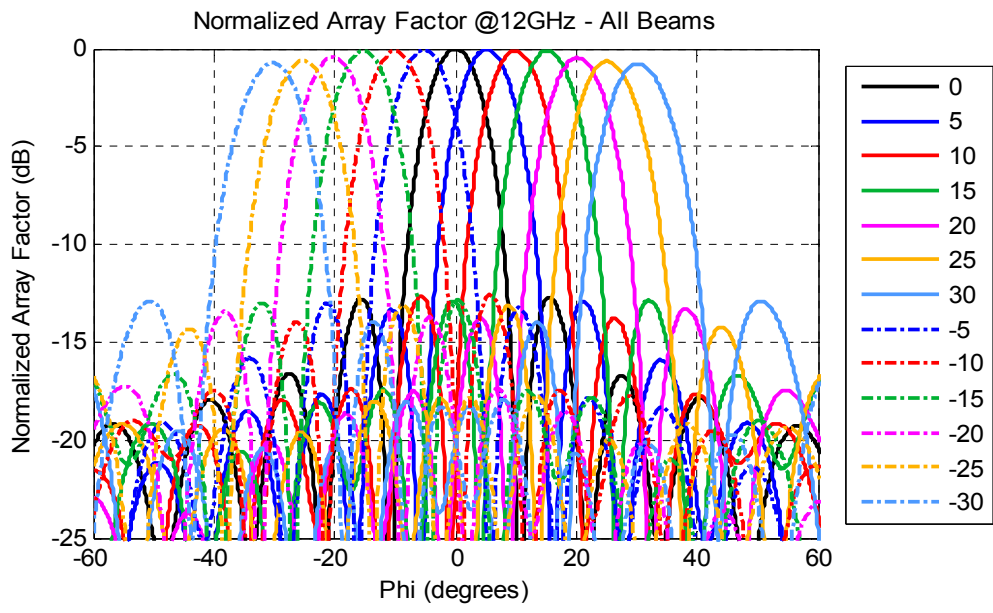


Figure 4 - 25: Normalized Array Factors of All Beams at 12 GHz

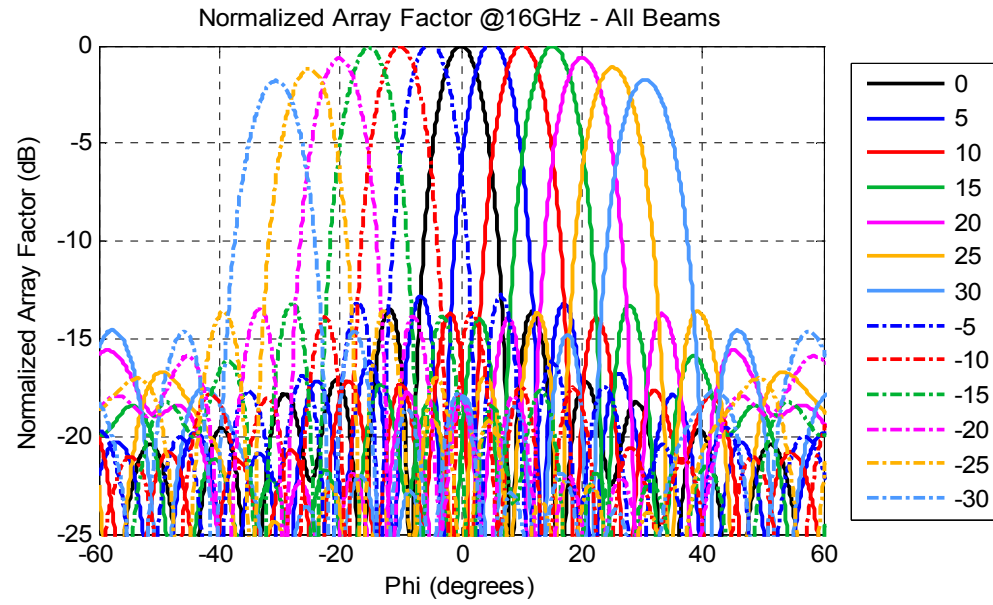


Figure 4 - 26: Normalized Array Factors of All Beams at 16 GHz

In order to investigate the beam scanning characteristics in detail; beam peak angles, 3dB beamwidths and levels of the first sidelobes are calculated for each beam port and tabulated at Table 4 - 4, Table 4 - 5 and Table 4 - 6, respectively. Hence, the maximum beam peak angle error is calculated as 0.6° . Besides, it is deduced that for a constant frequency, 3 dB beamwidths remain almost same for the different scan angles. Also, when first sidelobe levels are concerned, it is seen that the highest first sidelobe level is -11.6 dB which is acceptable for this study.

Table 4 - 4: Peak Angles of the Simulated Array Factor

		Peak Angle (degrees)								
Scan Angle (degrees) ↓	Freq. (GHz) →	8	9	10	11	12	13	14	15	16
-30	-30,5	-30,2	-30,3	-30,5	-30,2	-30,2	-30,6	-30,2	-30,6	-30,6
-25	-25,1	-25,1	-25,1	-25,2	-25,1	-25,2	-25,4	-25,2	-25,2	-25,2
-20	-20,3	-20,3	-20,3	-20,4	-20,2	-20,1	-20,2	-20,3	-20,1	-20,1
-15	-14,7	-15,2	-15,2	-15,2	-15,2	-15,1	-15,1	-15,2	-15,2	-15,2
-10	-10,4	-9,9	-10,1	-10,1	-9,9	-10,0	-9,9	-10,0	-10,1	-10,1
-5	-5,0	-5,1	-5,1	-5,2	-5,2	-5,0	-5,0	-5,1	-5,1	-5,1
0	0,0	0,0	0,0	0,0	0,0	0,0	0,0	0,0	0,0	0,0
5	5,0	5,1	5,1	5,2	5,2	5,0	5,0	5,1	5,1	5,1
10	10,4	9,9	10,1	10,1	9,9	10,0	9,9	10,0	10,1	10,1
15	14,7	15,2	15,2	15,2	15,2	15,1	15,1	15,2	15,2	15,2
20	20,3	20,4	20,4	20,4	20,2	20,1	20,2	20,3	20,1	20,1
25	25,2	25,1	25,2	25,3	25,2	25,2	25,4	25,2	25,2	25,2
30	30,5	30,2	30,3	30,5	30,3	30,2	30,6	30,2	30,6	30,6

Table 4 - 5: 3dB Beamwidths of the Simulated Array Factor

		3 dB Beamwidth (degrees)									
Scan Angle (degrees) ↓	Freq. (GHz) →	8	9	10	11	12	13	14	15	16	
-30		17,0	14,8	13,4	12,3	11,0	10,1	9,7	8,9	8,6	
-25		16,2	14,2	12,6	11,7	10,7	9,8	9,1	8,5	8,1	
-20		15,5	13,8	12,4	11,2	10,3	9,4	8,9	8,2	7,8	
-15		15,1	13,1	11,8	10,8	9,9	9,2	8,5	8,1	7,6	
-10		15,1	13,0	11,8	10,8	9,8	9,1	8,5	7,9	7,5	
-5		14,3	12,9	11,5	10,6	9,7	8,9	8,3	7,8	7,3	
0		14,6	12,6	11,4	10,6	9,6	8,8	8,3	7,8	7,4	
5		14,3	12,9	11,5	10,6	9,7	8,9	8,3	7,8	7,3	
10		15,1	13,0	11,8	10,8	9,8	9,0	8,5	7,9	7,5	
15		15,1	13,1	11,8	10,8	9,9	9,2	8,5	8,0	7,6	
20		15,5	13,9	12,4	11,2	10,4	9,5	8,9	8,3	7,8	
25		16,2	14,2	12,7	11,7	10,6	9,8	9,1	8,6	8,1	
30		17,0	14,9	13,4	12,3	11,0	10,2	9,7	8,9	8,6	

Table 4 - 6: First Sidelobe Levels of the Simulated Array Factor

		First Sidelobe Level (dBc) (Normalized to Peak)									
Scan Angle (degrees) ↓	Freq. (GHz) →	8	9	10	11	12	13	14	15	16	
-30		-15,2	-12,5	-13,0	-13,5	-12,7	-13,0	-13,4	-13,6	-13,5	
-25		-11,8	-13,1	-12,8	-12,6	-12,9	-12,8	-12,6	-13,1	-13,0	
-20		-13,1	-12,3	-13,0	-13,0	-12,5	-12,6	-13,1	-13,0	-13,6	
-15		-12,8	-12,5	-12,9	-12,9	-12,7	-12,7	-12,6	-13,1	-13,1	
-10		-12,4	-13,0	-13,0	-12,6	-13,0	-12,7	-13,2	-13,1	-12,8	
-5		-12,8	-12,5	-12,7	-12,9	-12,5	-12,8	-12,8	-13,1	-12,4	
0		-12,4	-12,9	-12,0	-12,7	-12,2	-12,5	-12,0	-11,6	-12,8	
5		-11,8	-13,1	-12,8	-12,6	-12,8	-13,0	-12,7	-13,1	-13,0	
10		-13,1	-12,2	-12,9	-13,0	-12,5	-12,7	-13,2	-13,0	-13,7	
15		-12,8	-12,4	-12,8	-12,9	-12,7	-12,7	-12,5	-13,0	-13,3	
20		-12,3	-13,0	-13,0	-12,5	-12,8	-12,6	-13,1	-13,1	-13,1	
25		-12,6	-12,5	-12,7	-12,8	-12,4	-12,9	-12,8	-13,3	-12,5	
30		-12,3	-12,8	-12,0	-12,6	-12,1	-12,4	-11,9	-11,5	-12,8	

CHAPTER 5

PRODUCTION AND MEASUREMENT RESULTS

Lens implementation procedure was explained and simulation results of the implemented lens were given in the previous chapter. The implemented structure is manufactured and several measurements are conducted. In this chapter, production process and the measurements will be explained. Besides, measurement results will be given and compared with the simulation results.

5.1 Production Process

In the previous chapter, implementation of the designed lens structure was explained in detail. The implemented lens is fabricated on a printed circuit substrate and the product is shown in Figure 5 - 1 (a). After printed circuit production, SMA connectors are installed at the port locations as shown in Figure 5 - 1 (b). Inner conductors of the SMA connectors are soldered to the line ends of the transmission lines at the ports. Soldering process needs to be done carefully since it directly affects the return loss performance of the ports.

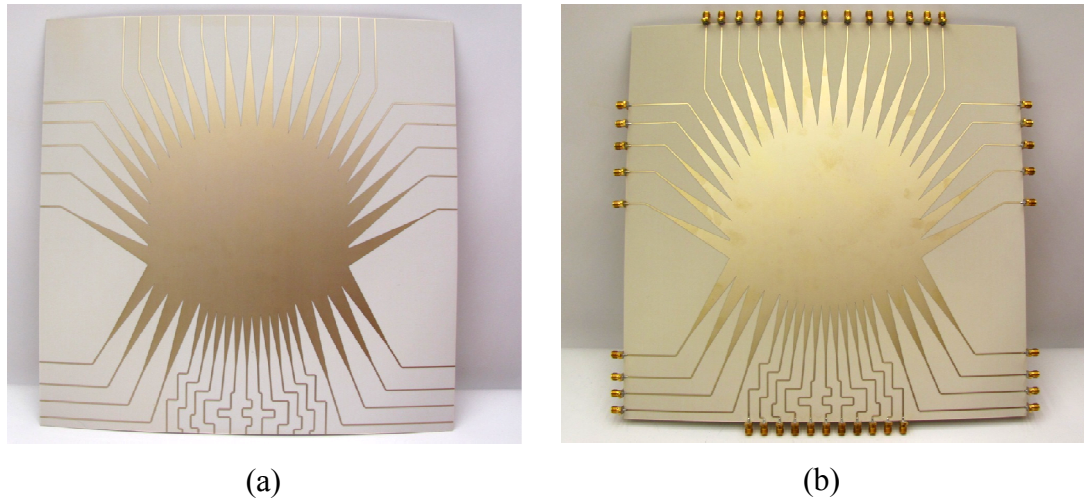


Figure 5 - 1: Fabricated Rotman lens: (a) After printed circuit production; (b) After SMA connectors are installed.

5.2 Measurements

In order to verify the performance of the fabricated lens, several measurements are carried out. At first, S-parameters of the lens are measured using a network analyzer and the results are compared with the simulation results. Then, an antenna array of 11 elements is connected to the lens output and antenna measurements are conducted.

5.2.1 Network Analyzer Measurements

S-parameters of the fabricated Rotman lens are measured using a network analyzer with the setup given in Figure 5 - 2. Port numbering convention is as defined in the previous chapter and also shown in the figure.

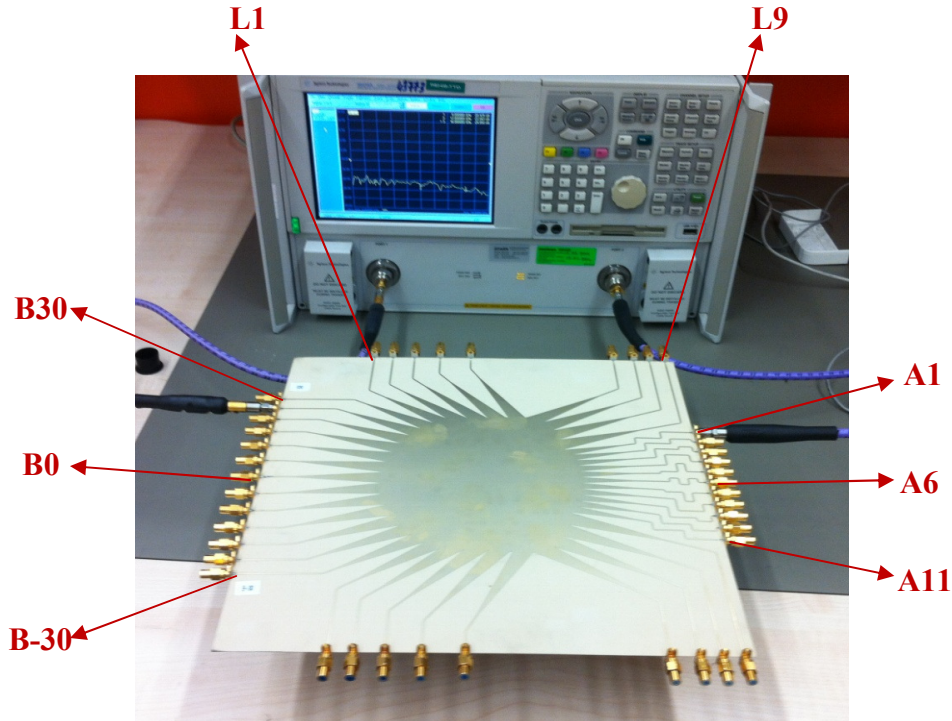


Figure 5 - 2: Network Analyzer Measurement Setup for the Rotman lens

In order to measure the phases accurately, phase-stable cables are used during the measurements. Besides, the ports other than the measured ports are terminated with 50Ω SMA loads in order to avoid undesired reflections.

Return Loss Performance

Measured return loss values of beam and array ports are given in Figure 5 - 3 and Figure 5 - 4, respectively. According to the figures, both beam and array ports' return losses are better than 10 dB over the whole frequency band. Besides, when compared to the simulation results given in the previous chapter (Figure 4 - 9 and Figure 4 - 10), it is seen that return loss performance did not change much with the installation of SMA connectors. Hence, in return loss performance point of view, measurement and simulation results seem to be compatible with each other.

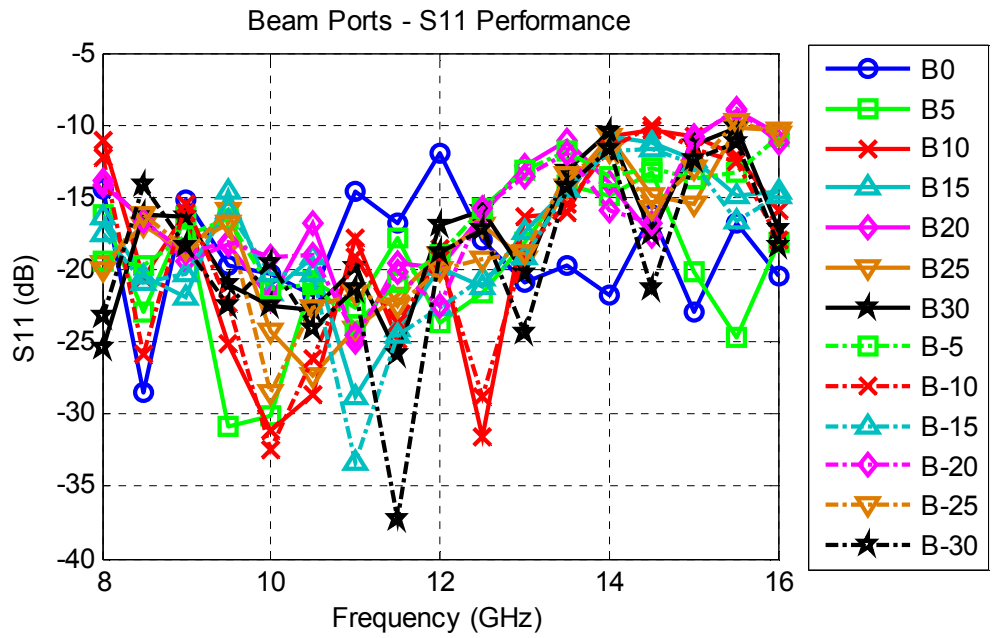


Figure 5 - 3: Measured Return Loss of the Beam Ports

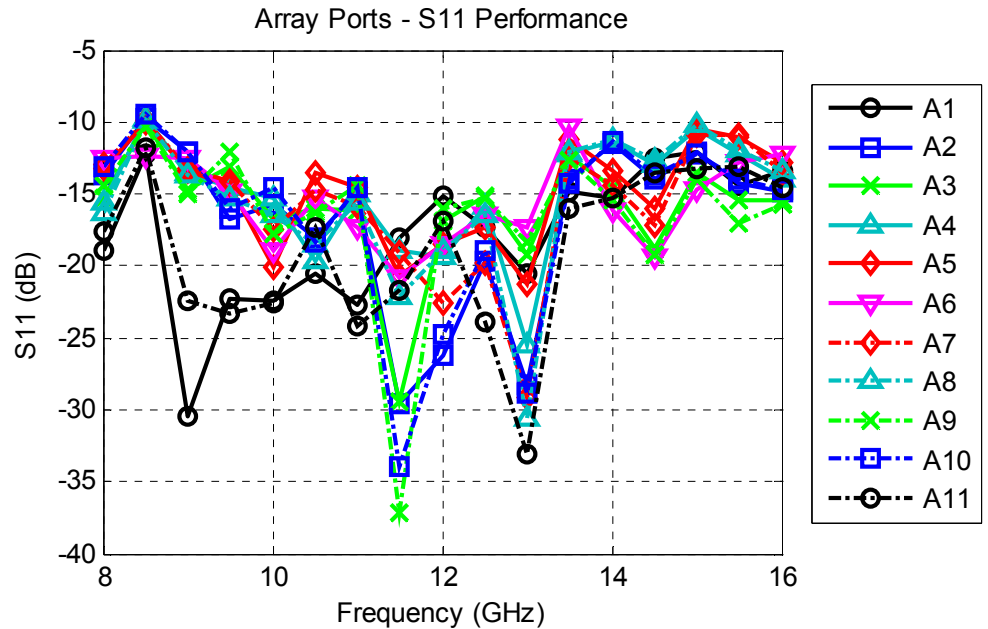


Figure 5 - 4: Measured Return Loss of the Array Ports

Coupling between Ports

Coupling effects between the ports of the microstrip structure was investigated in the previous chapter through the simulation results. In order to verify that the coupling levels of the fabricated lens do not distort the lens performance, coupling between beam ports and array ports are also measured.

The measured coupling between the center beam port, B0 and the other beam ports is plotted in Figure 5 - 5 and the coupling between the two adjacent beam ports is also plotted in Figure 5 - 6. Therefore, from the figures, it is seen that the coupling levels between the beam ports remain below -20 dB which is better than the coupling levels obtained from the simulation results (Figure 4 - 11, Figure 4 - 12).

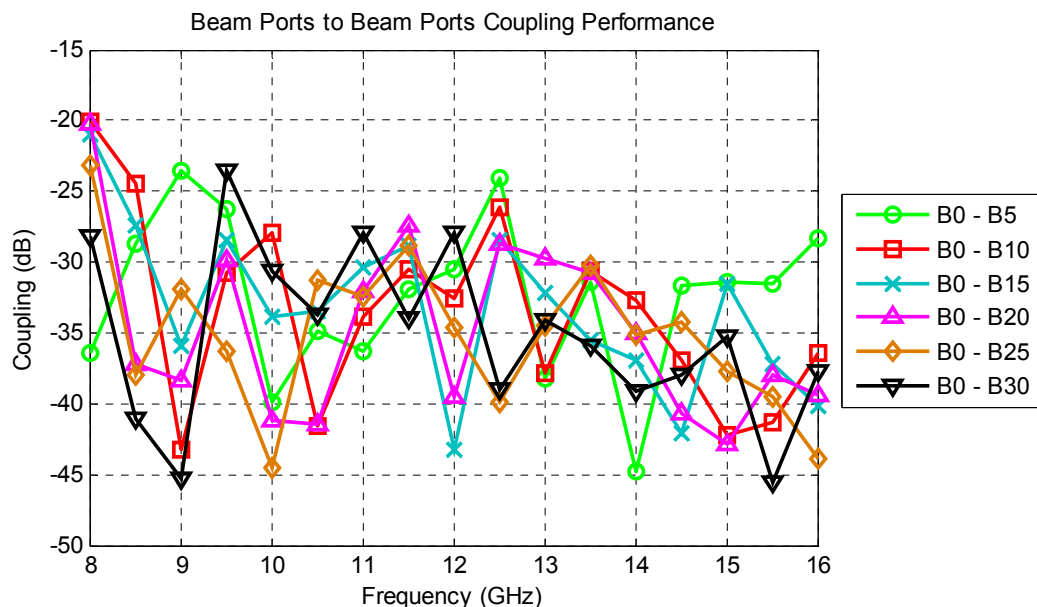


Figure 5 - 5: Measured Coupling between the Beam Ports

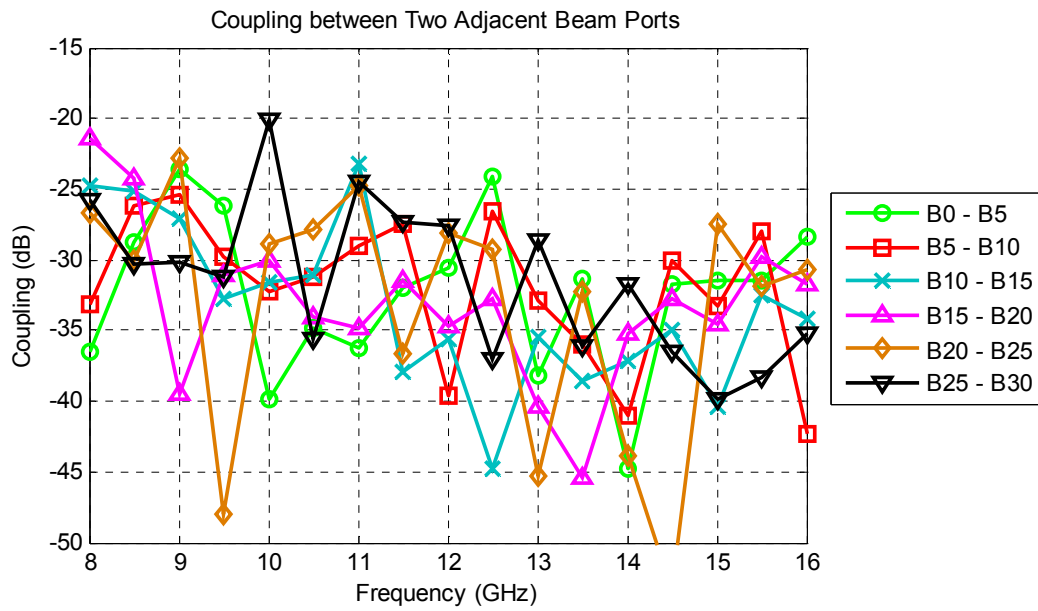


Figure 5 - 6: Measured Coupling between the Two Adjacent Beam Ports

The coupling levels are also measured for the array ports. The measured coupling between the center array port, A6 and the other array ports is plotted in Figure 5 - 7 and the coupling between the two adjacent beam ports is also plotted in Figure 5 - 8. Hence, it is observed that the coupling levels between the array ports remain below -15 dB for the measured cases which is better than the coupling levels obtained from the simulation results (Figure 4 - 13, Figure 4 - 14).

When the coupling measurements of both beam and array ports are considered together, it is seen that the coupling levels should be sufficient not to affect the lens scanning performance. Besides, the measured coupling levels seem to be improved compared to the simulation results. The reason for this improvement in coupling levels could be due to the insertion losses of the installed SMA connectors.

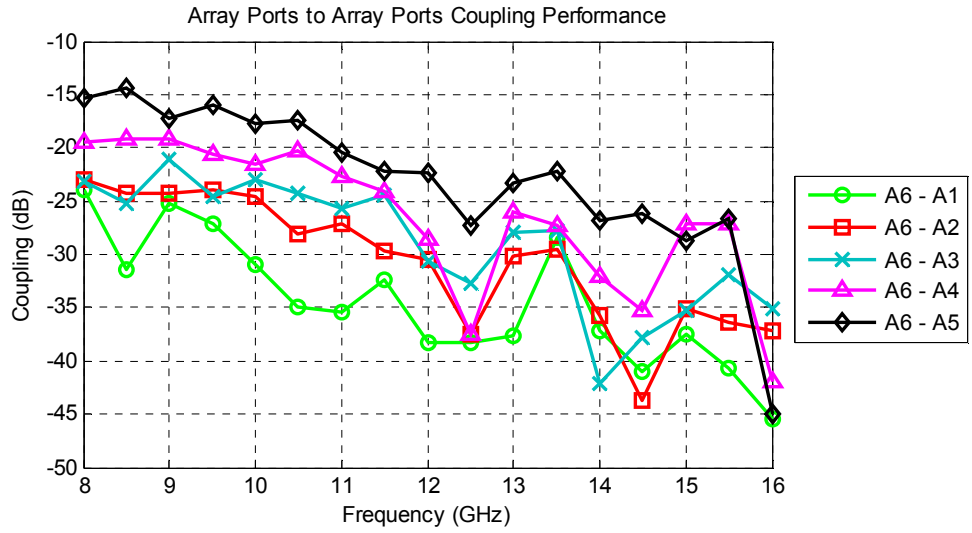


Figure 5 - 7: Measured Coupling between the Array Ports

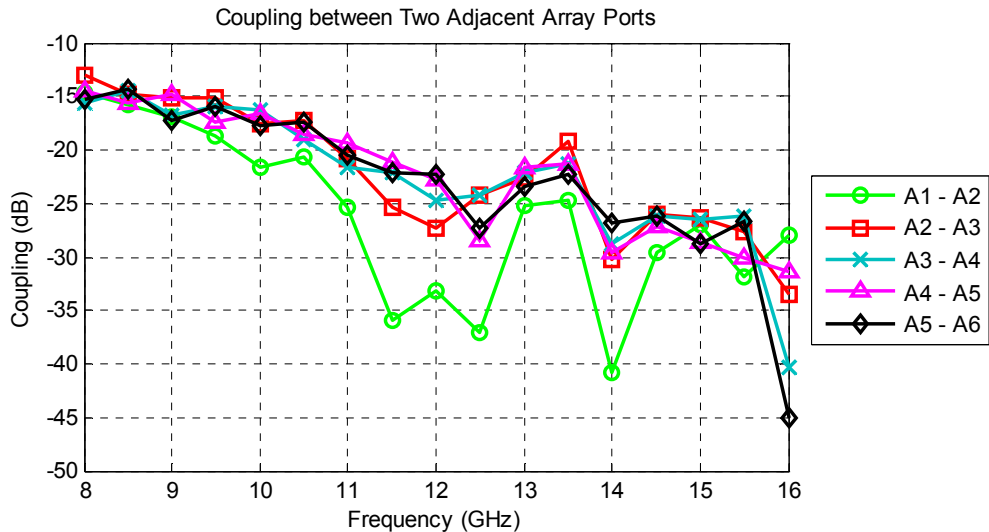


Figure 5 - 8: Measured Coupling between the Two Adjacent Array Ports

In the previous chapter, the lost power transmitted to the dummy ports was also investigated. For comparison, the power transmitted to the dummy ports is also measured. The measured coupling between the dummy ports and B0 can be observed in Figure 5 - 9 and the measured coupling between the dummy ports and

A6 can be observed in Figure 5 - 10. Similar to the previous coupling results, the lost power levels are also improved compared to the simulation results (Figure 4 - 15, Figure 4 - 16).

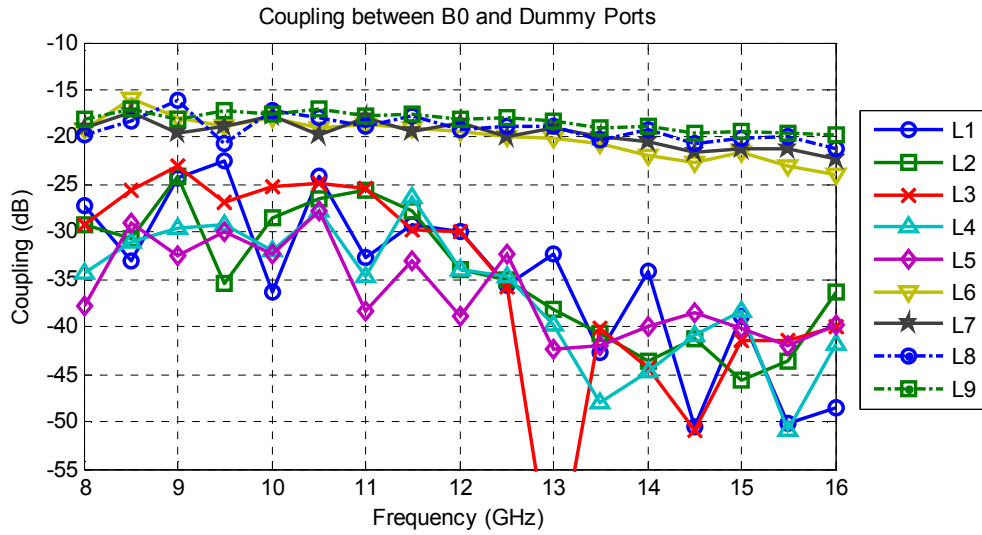


Figure 5 - 9: Measured Coupling between B0 and the Dummy Ports

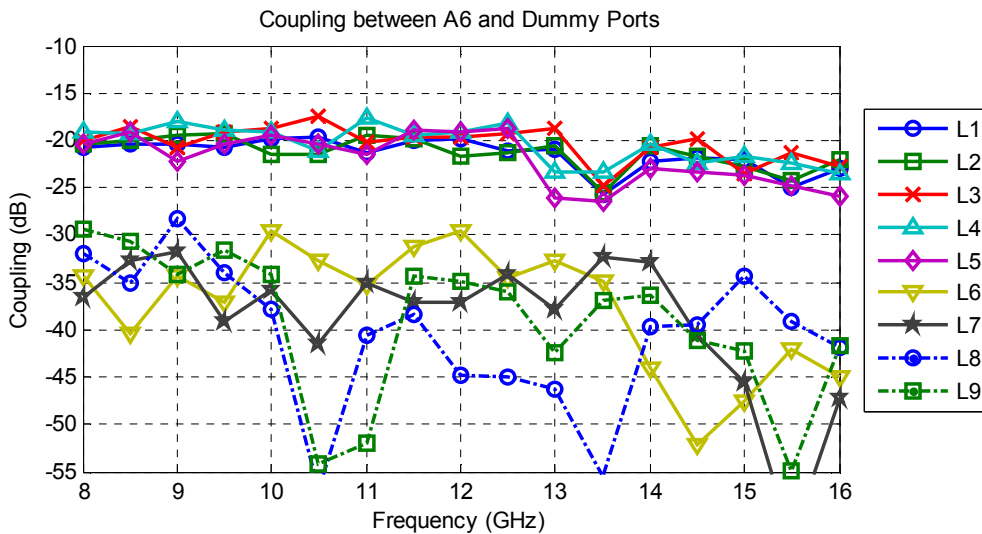


Figure 5 - 10: Measured Coupling between A6 and Dummy Ports

Considering all of the coupling results together, the measurement results seem to be very similar to the simulation results except a small amount of improvement.

Amplitude and Phase Distributions over the Array Elements

The amplitude distribution of the Rotman lens is not concerned in the design procedure. However, non-uniform and random amplitude distributions may increase the sidelobe levels of the radiation pattern. Furthermore, the amplitude distribution over the array aperture should be investigated in order not to have high sidelobe levels.

Amplitude distribution obtained from the simulation results was investigated in the previous chapter and that distribution seemed to be sufficient not to have high sidelobe levels. In this chapter, for comparison, insertion losses from a certain beam port to the antenna elements are plotted together with the simulation results given in the previous chapter. The plots of the amplitude distribution over antenna elements for the excitations from B0, B15 and B30 are given in Figure 5 - 11, Figure 5 - 12 and Figure 5 - 13, respectively. In the plots, solid lines are the measurement results and dashed lines are the simulation results. When the plots are examined, it is observed that the measured insertion loss levels are 3 – 4 dB below from the simulated levels. The possible reasons for this additional loss could be the loss due to the installed SMA connectors and/or the non-ideal loss characteristics of the used dielectric substrate. However, the behavior of the measured amplitude distribution over the antenna elements is very similar to the simulation results.

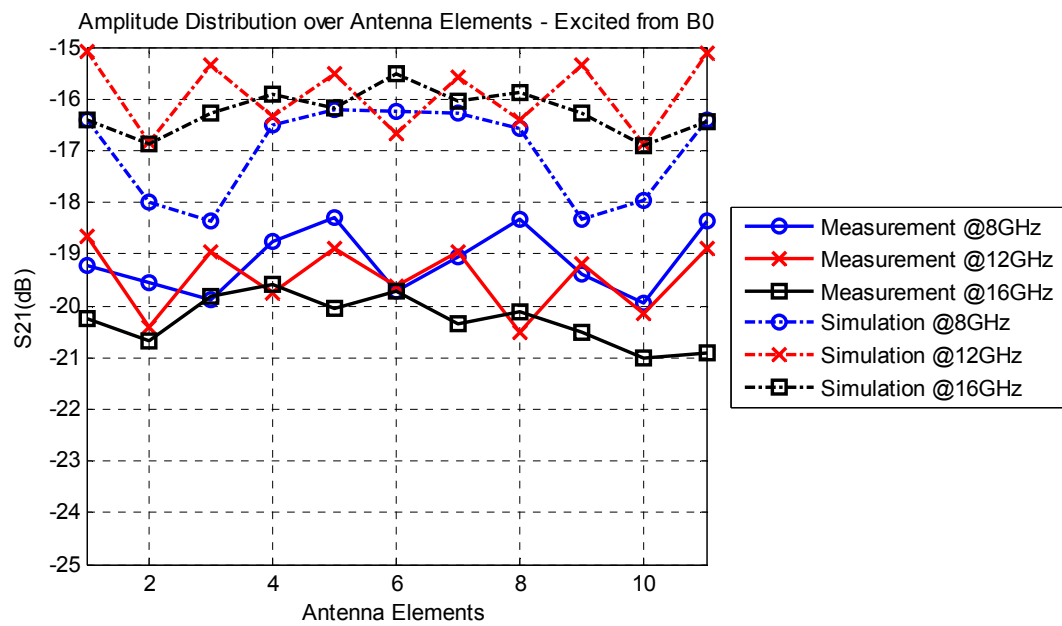


Figure 5 - 11: Amplitude Distribution over Antennas excited from B0

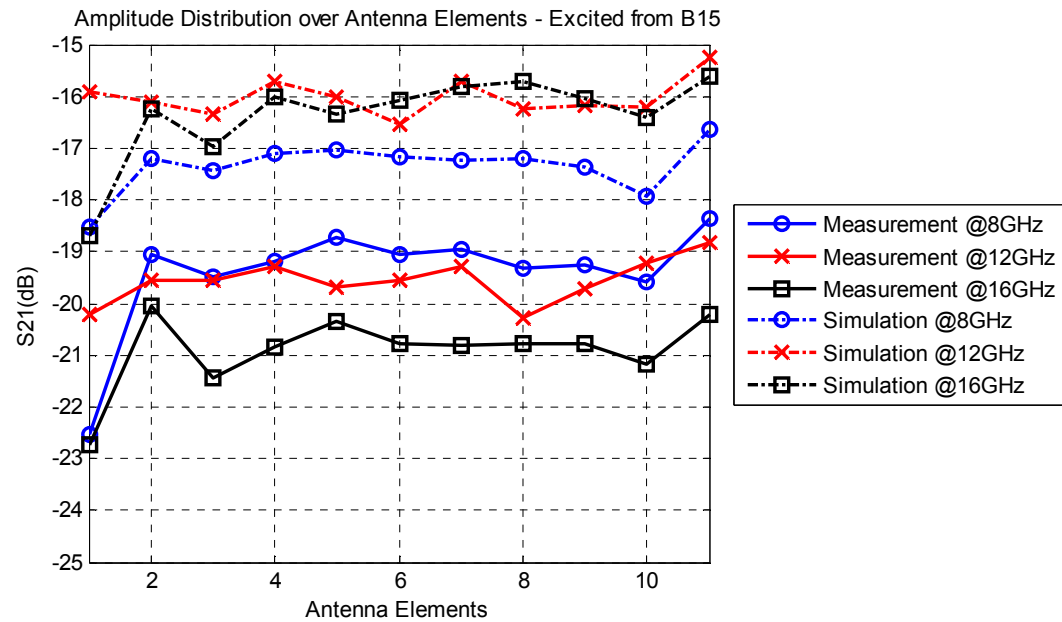


Figure 5 - 12: Amplitude Distribution over Antennas excited from B15

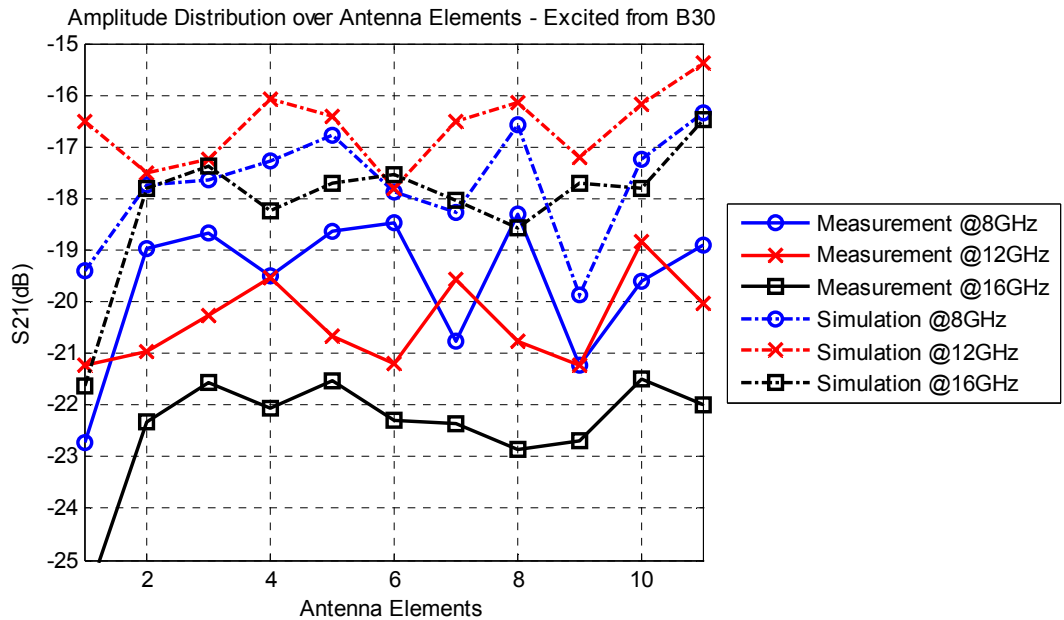


Figure 5 - 13: Amplitude Distribution over Antennas excited from B30

After the inspection of the amplitude distribution, phase distributions are also investigated. Measured insertion loss phases are plotted together with the simulation results given in the previous chapter. The plots for the excitation from beam ports B0, B15 and B30 are given in Figure 5 - 14, Figure 5 - 15 and Figure 5 - 16, respectively. In the plots, solid lines are the measurements and dashed lines are the simulations. When all plots are considered, measurement and simulation results seem to be compatible with each other, in general. For the excitation from B0, there are some differences between the phase levels of the measurement and the simulation results. However, the symmetrical phase distribution for the excitation from B0 is not distorted by these differences. Besides, for the excitations from B15 and B30, some differences are also observed. Nevertheless, the behavior of the measured and simulated phase distributions seem to be very similar.

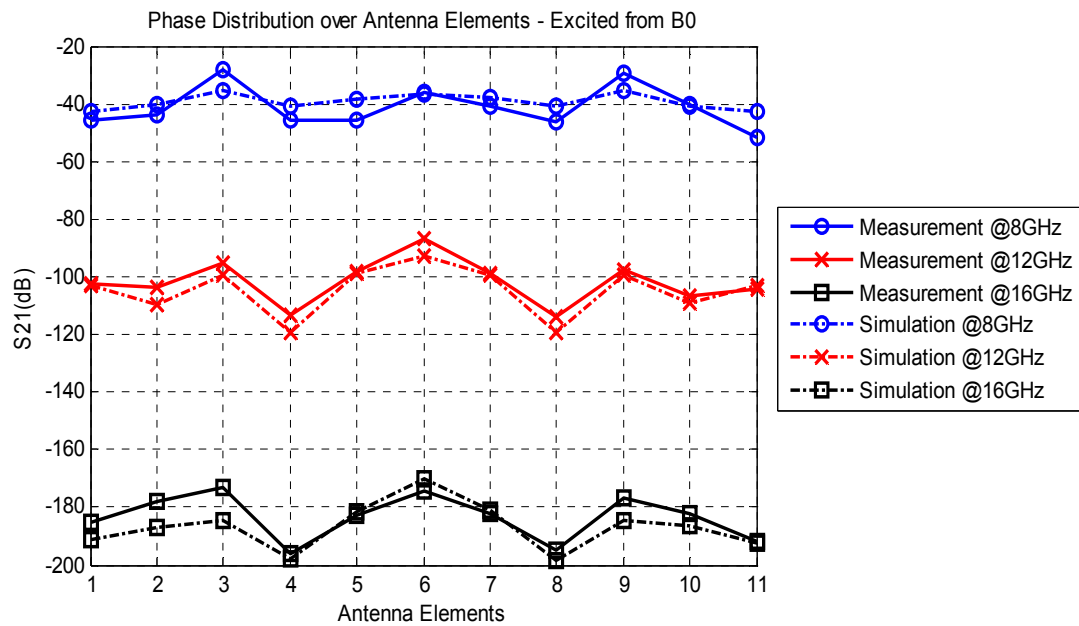


Figure 5 - 14: Phase Distribution over Antennas excited from B0

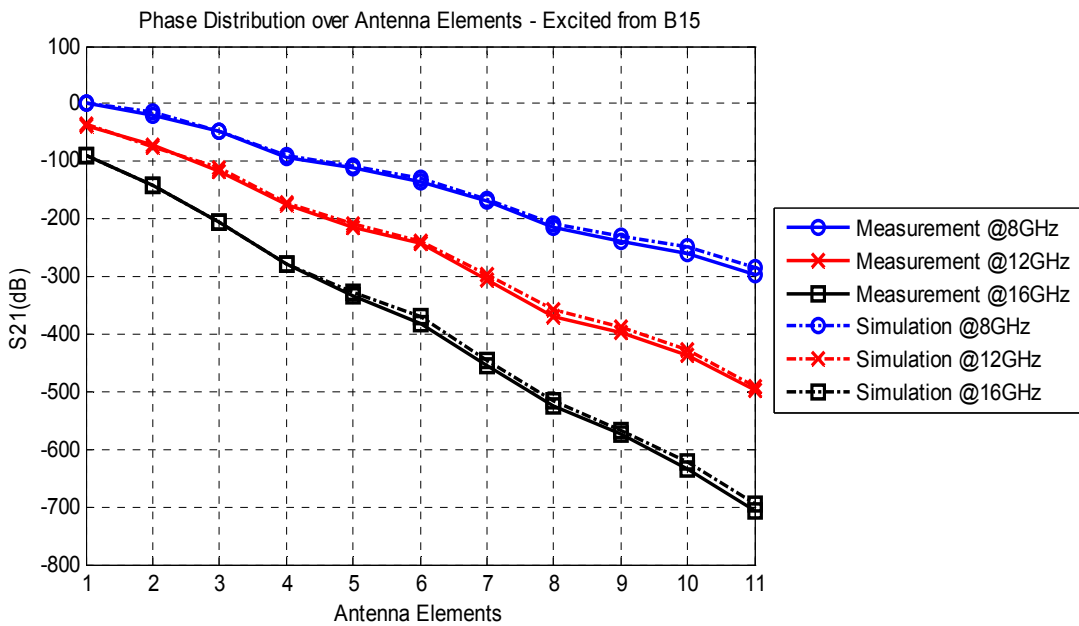


Figure 5 - 15: Phase Distribution over Antennas excited from B15

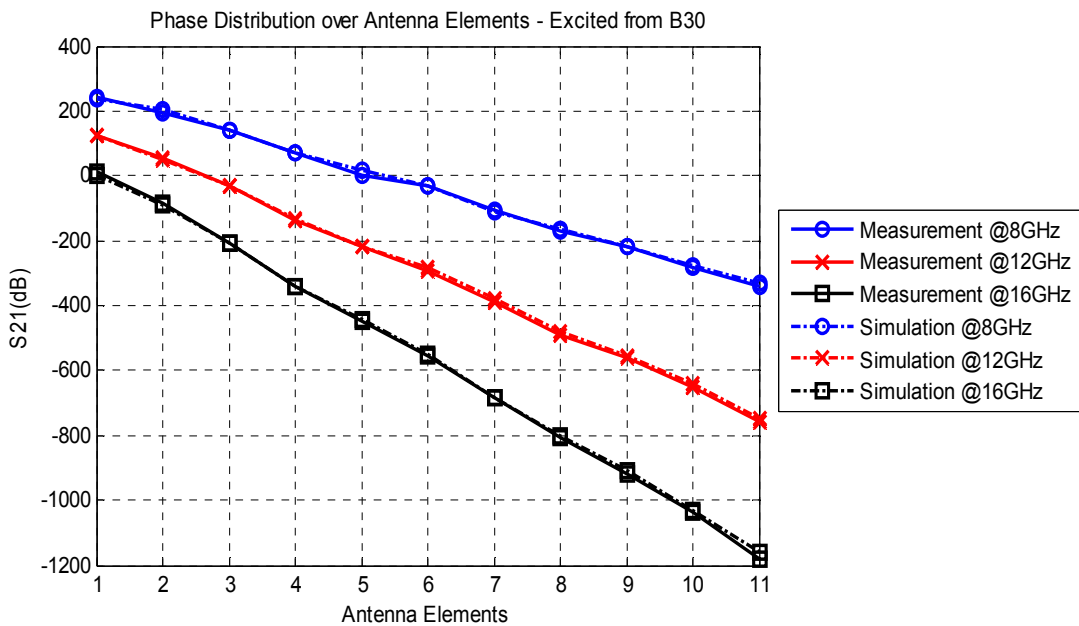


Figure 5 - 16: Phase Distribution over Antennas excited from B30

Array Factors Calculated from the Measurement Results

In the previous chapter, in order to investigate the beam scanning capabilities of the Rotman lens, array factors were calculated using the simulated insertion losses as excitation coefficients. Detailed array factor calculation procedure was also given in the previous chapter. In this chapter, measured insertion losses are used to calculate the array factors. The array factors are calculated for each beam excitation by following the procedure given in the previous chapter.

The array factors calculated using the measured S21 for all beam ports are plotted on the same plot with the array factors calculated using the simulated S21 values, for comparison. In the plots, all of the array factors are normalized with respect to the peak values of the array factors corresponding to each beam. Hence, plots are given for the frequencies 8, 12 and 16 GHz in Figure 5 - 17, Figure 5 - 18 and Figure 5 - 19, respectively. In the given plots, the solid lines are the array factors

calculated using the measured S21 and the dashed lines are the array factors calculated using the simulated S21. From the figures, it is observed that the array factors calculated with the simulation and measurement results are very similar. Therefore, the scanning capabilities of the manufactured lens are verified.

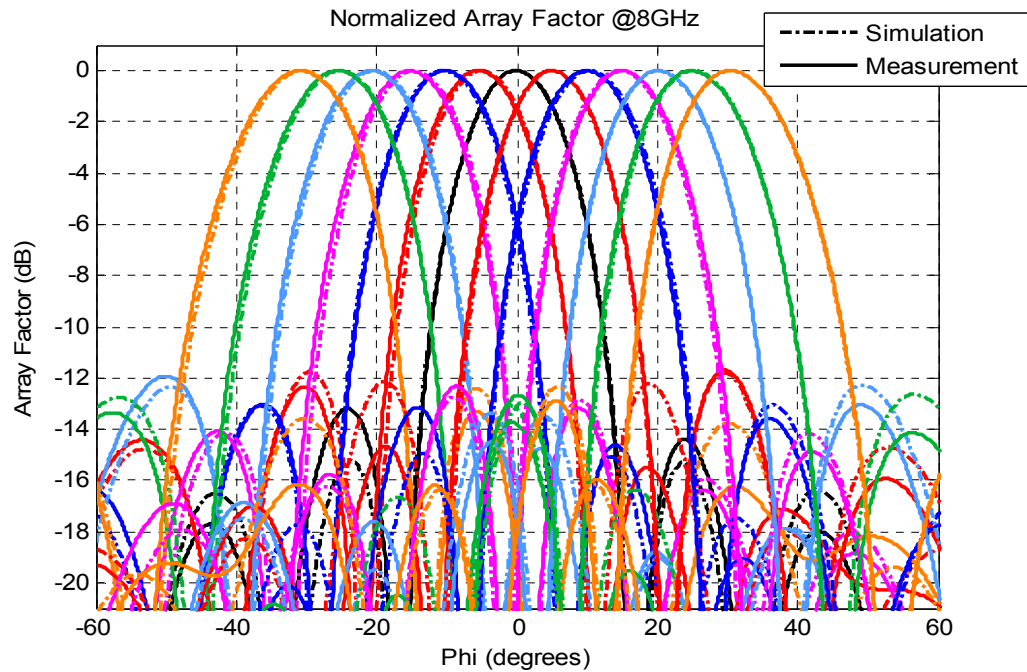


Figure 5 - 17: Measured and Simulated Array Factors of All Beams at 8 GHz

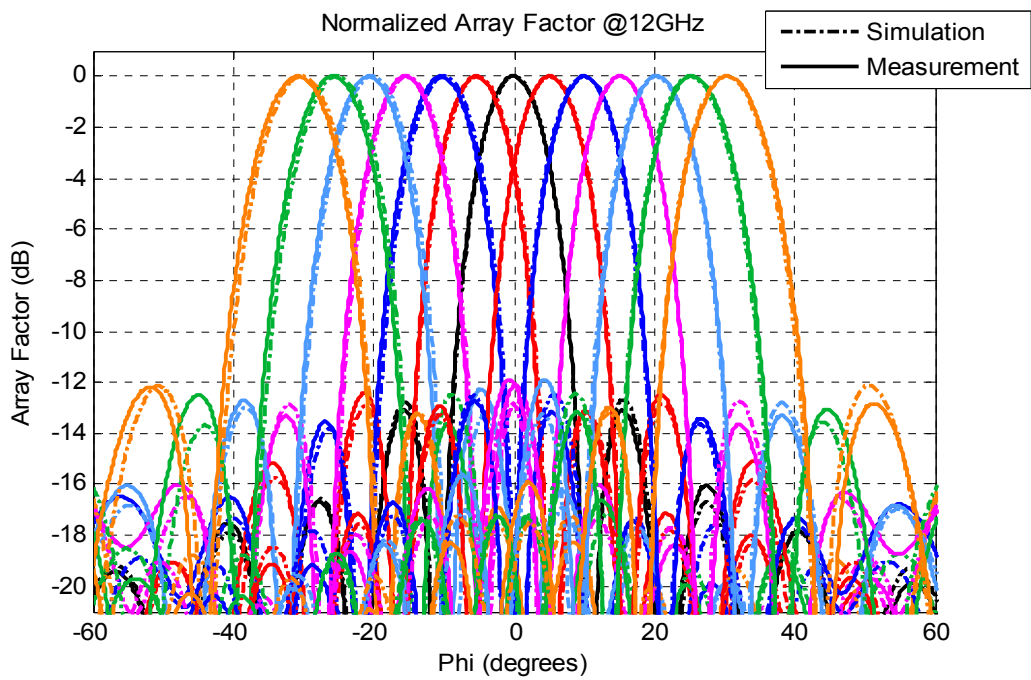


Figure 5 - 18: Measured and Simulated Array Factors of All Beams at 12 GHz

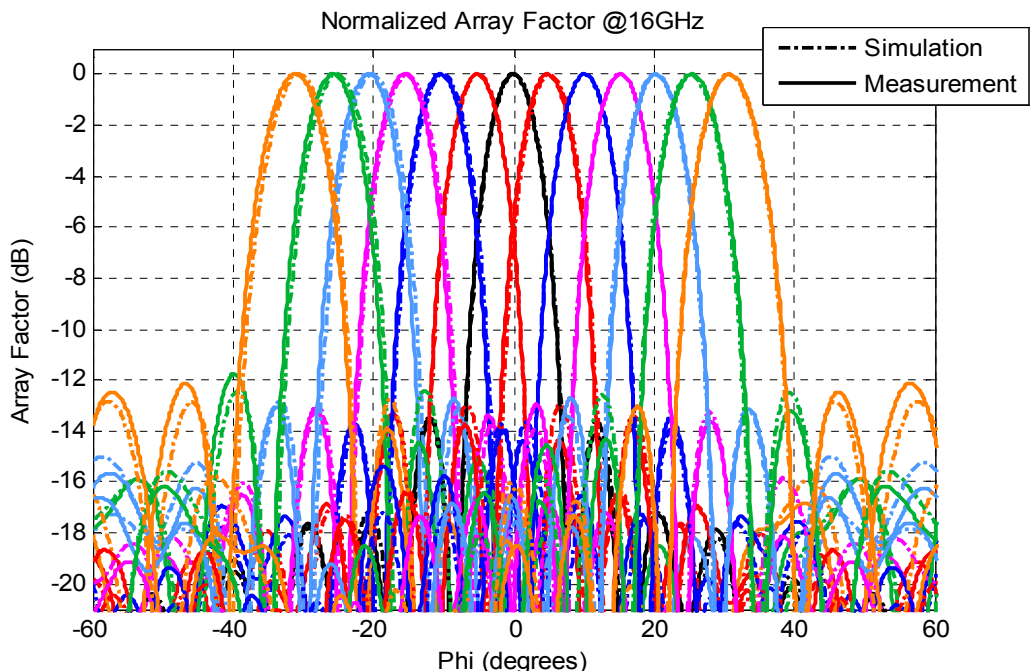


Figure 5 - 19: Measured and Simulated Array Factors of All Beams at 16 GHz

The plots are very beneficial to observe the beam scanning characteristics of the lens. However, in order to investigate the array factors in detail, for each beam port; peak angles, 3 dB beamwidths and levels of the first sidelobes are calculated and tabulated at Table 5 - 1, Table 5 - 2 and Table 5 - 3, respectively. The parameters for both the array factors calculated from the simulation and measurement results are presented in the tables. When compared, the maximum difference between the peak angles of the measurement and the simulation results is 0.7° . Also, the maximum difference between the beamwidths is 0.4° . Besides, when sidelobe levels are assessed, it is observed that the measured sidelobe levels are higher than the simulated sidelobe levels, in general.

Table 5 - 1: Peak Angles of the Simulated and Measured Array Factors

		Peak Angle (degrees)									
Scan Angle (degrees) ↓	Freq. (GHz) →	8	9	10	11	12	13	14	15	16	
-30	Sim.	-30,5	-30,2	-30,3	-30,5	-30,2	-30,2	-30,6	-30,2	-30,6	
	Meas.	-30,9	-30,5	-31,1	-31,1	-30,8	-30,9	-31,1	-30,8	-31,1	
-25	Sim.	-25,1	-25,1	-25,1	-25,2	-25,1	-25,2	-25,4	-25,2	-25,2	
	Meas.	-25,5	-25,7	-25,7	-25,8	-25,8	-25,7	-25,9	-25,7	-25,7	
-20	Sim.	-20,3	-20,3	-20,3	-20,4	-20,2	-20,1	-20,2	-20,3	-20,1	
	Meas.	-20,7	-20,5	-20,8	-20,9	-20,7	-20,6	-20,6	-20,6	-20,7	
-15	Sim.	-14,7	-15,2	-15,2	-15,2	-15,2	-15,1	-15,1	-15,2	-15,2	
	Meas.	-15,2	-15,6	-15,3	-15,3	-15,5	-15,4	-15,4	-15,5	-15,5	
-10	Sim.	-10,4	-9,9	-10,1	-10,1	-9,9	-10,0	-9,9	-10,0	-10,1	
	Meas.	-10,1	-10,1	-10,1	-10,3	-10,4	-10,4	-10,3	-10,3	-10,4	
-5	Sim.	-5,0	-5,1	-5,1	-5,2	-5,2	-5,0	-5,0	-5,1	-5,1	
	Meas.	-5,5	-5,1	-5,2	-5,4	-5,4	-5,4	-5,3	-5,3	-5,2	
0	Sim.	0,0	0,0	0,0	0,0	0,0	0,0	0,0	0,0	0,0	
	Meas.	-0,1	-0,2	0,1	0,1	-0,1	-0,1	-0,2	-0,2	-0,1	
5	Sim.	5,0	5,1	5,1	5,2	5,2	5,0	5,0	5,1	5,1	
	Meas.	5,0	4,8	4,9	5,1	5,1	5,0	4,9	4,9	4,8	
10	Sim.	10,4	9,9	10,1	10,1	9,9	10,0	9,9	10,0	10,1	
	Meas.	10,0	9,9	10,0	10,1	10,1	10,1	9,9	9,9	10,1	
15	Sim.	14,7	15,2	15,2	15,2	15,2	15,1	15,1	15,2	15,2	
	Meas.	15,0	15,2	15,0	15,0	15,1	15,1	15,1	15,1	15,2	
20	Sim.	20,3	20,4	20,4	20,4	20,2	20,1	20,2	20,3	20,1	
	Meas.	20,2	20,1	20,3	20,5	20,4	20,2	20,3	20,3	20,3	
25	Sim.	25,2	25,1	25,2	25,3	25,2	25,2	25,4	25,2	25,2	
	Meas.	24,9	25,3	25,3	25,4	25,4	25,4	25,6	25,3	25,4	
30	Sim.	30,5	30,2	30,3	30,5	30,3	30,2	30,6	30,2	30,6	
	Meas.	30,5	30,1	30,6	30,6	30,4	30,5	30,7	30,5	30,7	

Table 5 - 2: 3 dB Beamwidths of the Simulated and Measured Array Factors

		3 dB Beamwidth (degrees)									
Scan Angle (degrees) ↓	Freq. (GHz) →	8	9	10	11	12	13	14	15	16	
-30	Sim.	17,0	14,8	13,4	12,3	11,0	10,1	9,7	8,9	8,6	
	Meas.	17,4	14,9	13,2	12,4	11,3	10,3	9,8	9	8,7	
-25	Sim.	16,2	14,2	12,6	11,7	10,7	9,8	9,1	8,5	8,1	
	Meas.	16,5	14,5	12,8	11,7	10,7	9,9	9,2	8,5	8	
-20	Sim.	15,5	13,8	12,4	11,2	10,3	9,4	8,9	8,2	7,8	
	Meas.	15,7	13,6	12,2	11,1	10,2	9,4	8,8	8,2	7,8	
-15	Sim.	15,1	13,1	11,8	10,8	9,9	9,2	8,5	8,1	7,6	
	Meas.	15,4	13,3	11,8	10,8	9,9	9,2	8,5	8	7,5	
-10	Sim.	15,1	13,0	11,8	10,8	9,8	9,1	8,5	7,9	7,5	
	Meas.	15,1	12,8	11,6	10,6	9,8	9,1	8,4	7,8	7,5	
-5	Sim.	14,3	12,9	11,5	10,6	9,7	8,9	8,3	7,8	7,3	
	Meas.	14,7	12,9	11,5	10,4	9,6	8,9	8,3	7,8	7,4	
0	Sim.	14,6	12,6	11,4	10,6	9,6	8,8	8,3	7,8	7,4	
	Meas.	14,5	12,7	11,4	10,3	9,6	9	8,3	7,7	7,4	
5	Sim.	14,3	12,9	11,5	10,6	9,7	8,9	8,3	7,8	7,3	
	Meas.	14,6	12,9	11,5	10,6	9,6	8,9	8,4	7,8	7,3	
10	Sim.	15,1	13,0	11,8	10,8	9,8	9,0	8,5	7,9	7,5	
	Meas.	15	12,7	11,7	10,6	9,9	8,9	8,3	7,8	7,4	
15	Sim.	15,1	13,1	11,8	10,8	9,9	9,2	8,5	8,0	7,6	
	Meas.	15,2	13,2	11,8	10,8	10	9,2	8,5	7,9	7,6	
20	Sim.	15,5	13,9	12,4	11,2	10,4	9,5	8,9	8,3	7,8	
	Meas.	15,6	13,7	12,3	11,1	10,2	9,3	8,6	8,1	7,7	
25	Sim.	16,2	14,2	12,7	11,7	10,6	9,8	9,1	8,6	8,1	
	Meas.	16,4	14,4	12,9	11,7	10,7	9,8	9,1	8,6	8,1	
30	Sim.	17,0	14,9	13,4	12,3	11,0	10,2	9,7	8,9	8,6	
	Meas.	17,2	14,8	13,2	12,4	11,2	10,2	9,7	8,9	8,6	

Table 5 - 3: First Sidelobe Levels of the Simulated and Measured Array Factors

		First Sidelobe Level (dBc) (Normalized to Peak)									
Scan Angle (degrees) ↓	Freq. (GHz) →	8	9	10	11	12	13	14	15	16	
-30	Sim.	-15,2	-12,5	-13,0	-13,5	-12,7	-13,0	-13,4	-13,6	-13,5	
	Meas.	-12,1	-12,5	-10,6	-11,3	-11,8	-12,5	-14,5	-13,1	-13,8	
-25	Sim.	-11,8	-13,1	-12,8	-12,6	-12,9	-12,8	-12,6	-13,1	-13,0	
	Meas.	-12,1	-12,7	-12,0	-11,2	-11,9	-12,0	-13,6	-13,1	-13,6	
-20	Sim.	-13,1	-12,3	-13,0	-13,0	-12,5	-12,6	-13,1	-13,0	-13,6	
	Meas.	-10,8	-11,4	-11,2	-11,4	-11,4	-11,7	-11,7	-12,1	-13,7	
-15	Sim.	-12,8	-12,5	-12,9	-12,9	-12,7	-12,7	-12,6	-13,1	-13,1	
	Meas.	-11,7	-11,7	-11,1	-11,1	-10,9	-11,1	-13,1	-12,2	-13,3	
-10	Sim.	-12,4	-13,0	-13,0	-12,6	-13,0	-12,7	-13,2	-13,1	-12,8	
	Meas.	-11,7	-11,1	-10,7	-11,8	-12,1	-12,0	-12,9	-12,6	-13,6	
-5	Sim.	-12,8	-12,5	-12,7	-12,9	-12,5	-12,8	-12,8	-13,1	-12,4	
	Meas.	-10,8	-11,5	-11,0	-10,3	-10,8	-11,4	-12,8	-12,5	-13,0	
0	Sim.	-12,4	-12,9	-12,0	-12,7	-12,2	-12,5	-12,0	-11,6	-12,8	
	Meas.	-11,5	-11,0	-10,9	-11,0	-11,8	-11,6	-11,9	-12,5	-13,0	
5	Sim.	-11,8	-13,1	-12,8	-12,6	-12,8	-13,0	-12,7	-13,1	-13,0	
	Meas.	-10,0	-11,1	-11,2	-10,7	-10,8	-11,0	-12,0	-12,2	-13,8	
10	Sim.	-13,1	-12,2	-12,9	-13,0	-12,5	-12,7	-13,2	-13,0	-13,7	
	Meas.	-11,7	-10,9	-10,8	-11,2	-11,6	-11,1	-11,8	-12,1	-13,3	
15	Sim.	-12,8	-12,4	-12,8	-12,9	-12,7	-12,7	-12,5	-13,0	-13,3	
	Meas.	-10,9	-11,8	-11,0	-11,1	-10,8	-10,9	-12,4	-11,5	-12,9	
20	Sim.	-12,3	-13,0	-13,0	-12,5	-12,8	-12,6	-13,1	-13,1	-13,1	
	Meas.	-11,8	-11,3	-11,7	-11,0	-11,0	-10,8	-10,9	-12,0	-13,5	
25	Sim.	-12,6	-12,5	-12,7	-12,8	-12,4	-12,9	-12,8	-13,3	-12,5	
	Meas.	-11,4	-12,0	-12,1	-11,7	-12,7	-11,8	-13,2	-13,3	-14,9	
30	Sim.	-12,3	-12,8	-12,0	-12,6	-12,1	-12,4	-11,9	-11,5	-12,8	
	Meas.	-11,6	-12,1	-11,2	-12,5	-12,8	-12,4	-14,3	-13,8	-14,4	

5.2.2 Antenna Measurements

With the network analyzer measurements, significant S parameters of the manufactured lens have been measured and compared with the simulation results. Hence, it is observed that the lens is individually capable of directing the beam to the pre-defined angles at the desired frequencies.

So far, the lens operation has been inspected with the assumption of the perfectly matched isotropic antenna elements are connected to the output ports. However, in real world applications, directive antennas with non-ideal matching are used and the beamformer performance could be affected by the non-idealities caused by the antennas. Therefore, in order to investigate the lens performance when connected to an antenna array, antenna measurements are conducted with an antenna array of 11 elements.

A probe-fed microstrip patch array is designed with the purpose of investigating the lens performance when connected to an antenna array. A probe-fed microstrip patch is chosen as an array element because the design and manufacturing process of a probe-fed microstrip patch is easy and fast compared to the other alternatives (Vivaldi antennas, slot coupled patches, horns, etc.). However, since patch antennas are resonant antennas, only a small portion of the lens' operating frequency band can be tested with the patch array. Hence, the patch array is designed so that it operates at the center frequency which is 12 GHz.

First, a single probe-fed patch is designed. Patch size and probe location are optimized in HFSS® [22] in order to provide that the patch radiates at 12 GHz. Then, an array of 11 elements is constructed by placing the designed patches at a certain distance (12 mm). The distance between the antenna elements is determined by the lens design equations and the design parameters as explained in the previous chapter. Afterward, the array is simulated again in order to include the coupling effects that may occur due to the array construction. Moreover, the patch size and

probe location are optimized again in order to have proper radiation at 12 GHz. Hence, the array shown in Figure 5 - 20 is implemented and manufactured. Then, SMA connectors are soldered to the patches and the front and back view of the final antenna array after the connectors installed are given in Figure 5 - 21.

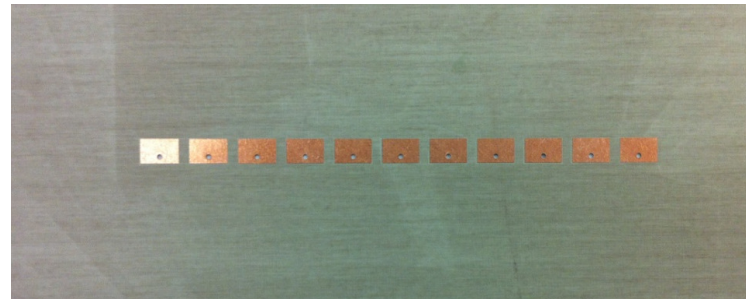


Figure 5 - 20: Printed Circuit Product of the Implemented Patch Array

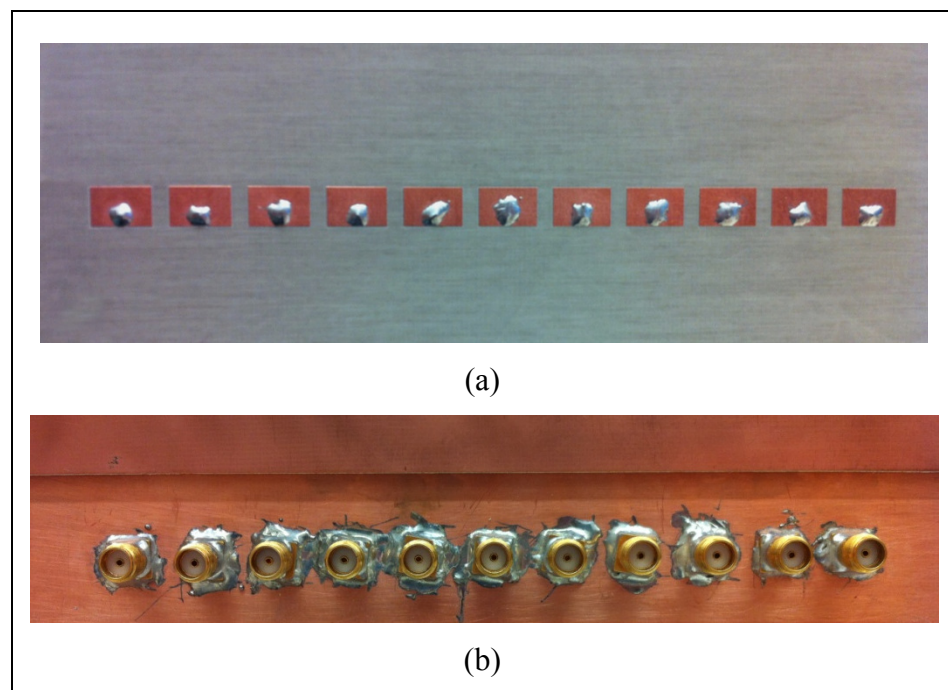


Figure 5 - 21: The Probe-Fed Patch Array after Connecter Installation: (a) Front View, (b) Back View

After the antenna array is manufactured, the only remaining problem is the connection between lens and antenna since the connection should not alter the phase distribution at the lens output. Furthermore, the utilized cables should insert the same phases for all ports. In order to match the phases of the coaxial cables, many cables of same length are measured in the network analyzer and the ones that have very close insertion phases are chosen. Along the chosen 11 cables, there exist at most $\pm 3^\circ$ phase differences between the cables. Hence, the array elements are connected to the lens output ports via the measured phase-matched coaxial cables. Besides, in order to provide an isolation between the antenna ports and the lens output ports, 6-dB coaxial attenuators are inserted between the antenna ports and the cables as shown in Figure 5 - 22.

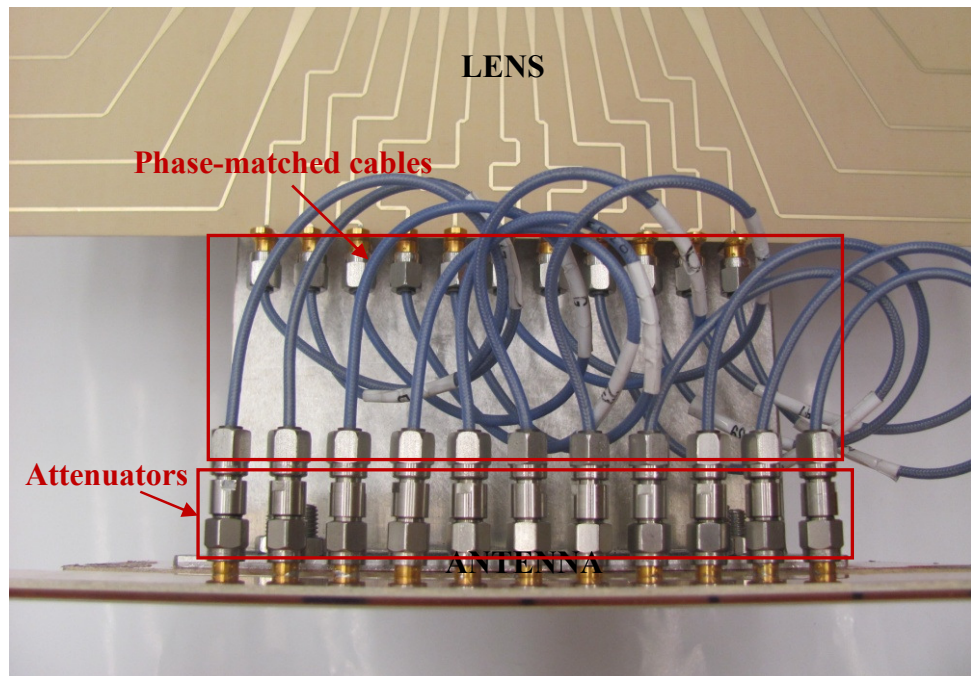


Figure 5 - 22: The Cable Connection between the Antenna and the Lens

For antenna measurements, planar near field antenna range is used. In this measurement system, a waveguide probe of the interested frequency scans a plane perpendicular to the boresight of the antenna at a distance which remains in the near field range of the antenna to be measured. Hence, the electric field at the near field zone of the antenna is obtained. Then, with necessary transformations, far-field radiation pattern is acquired.

The assembly of the antenna array and the lens is mounted on a mast as shown in Figure 5 - 23 and the near-field probe is aligned with respect to the center of the antenna array so that the boresight of the probe and the antenna coincide.

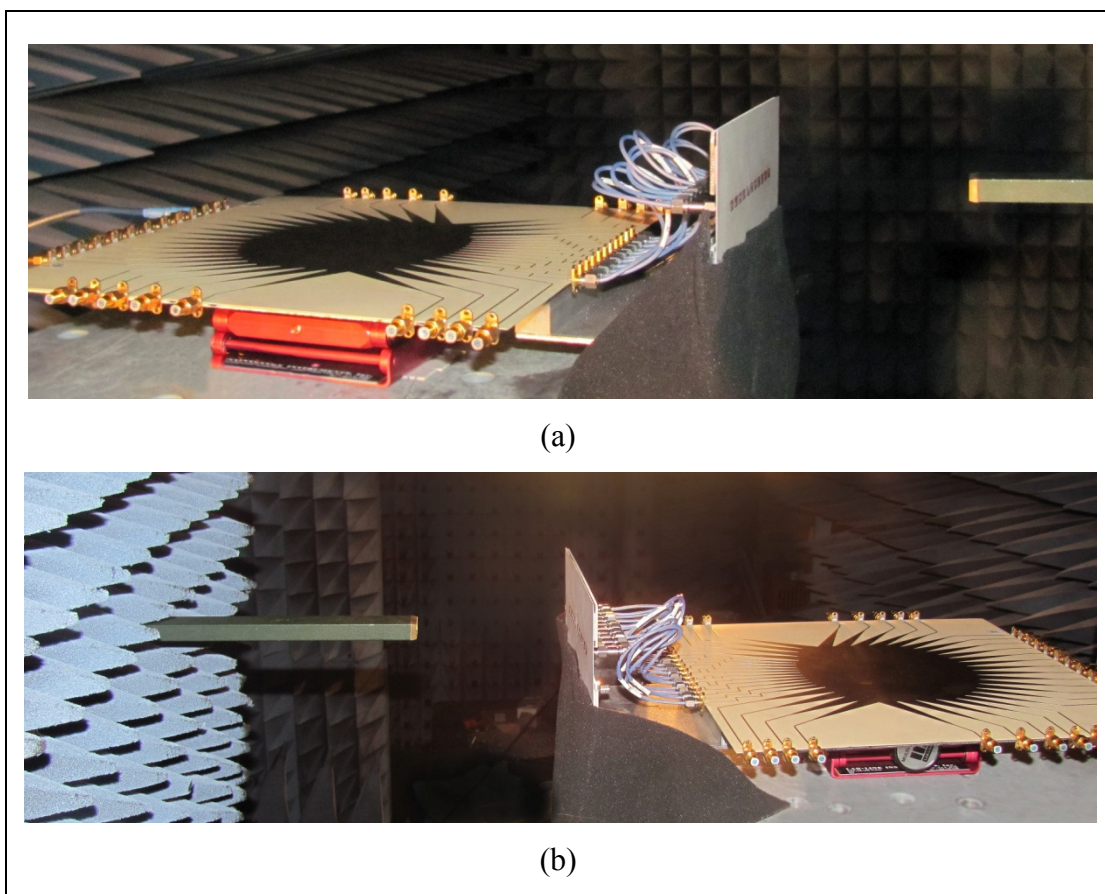


Figure 5 - 23: Setup for Antenna Measurements: (a) Right View, (b) Left View

In order to prevent the leakage radiation from the lens to affect the radiation pattern, the lens is enclosed by RF absorbing material as shown in Figure 5 - 24. Therefore, the coupling between the lens and the antenna is minimized as possible. Furthermore, during the measurements for all beam ports, this setup (Figure 5 - 24) is used.

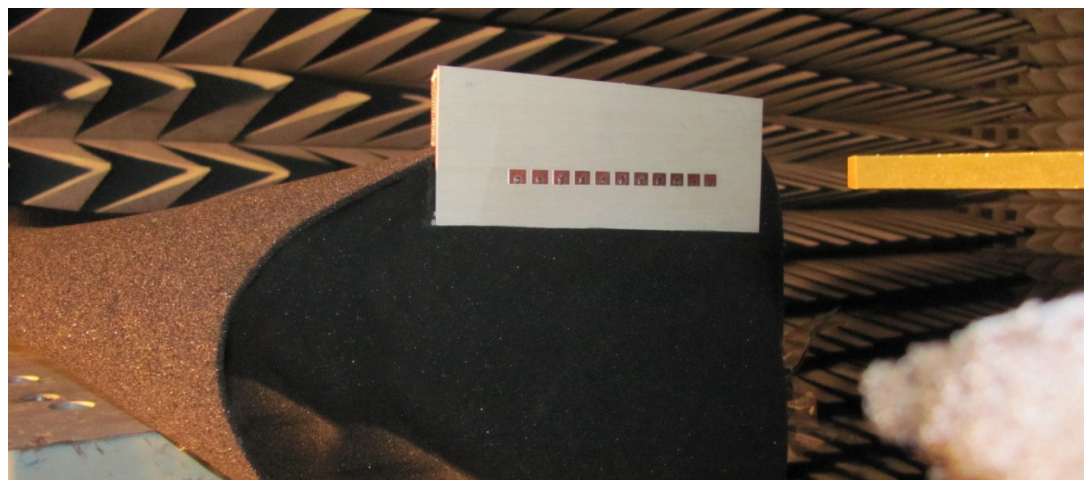


Figure 5 - 24: Final Setup used in Antenna Measurements

The radiation pattern is measured for all beam ports at the resonant frequency of the antenna array which is 12 GHz. Moreover, the results are compared with the pattern obtained from the multiplication of the array factor calculated using the network analyzer measurements and the simulated active radiation patterns of the array elements. Then, the compared results for all beam ports are plotted in Figure 5 - 25 where all of the patterns corresponding to each beam are normalized with respect to their peak values. Furthermore, from the comparison of the measured and simulated patterns in Figure 5 - 25, beam scanning capabilities of the lens when integrated with an antenna array are observed.

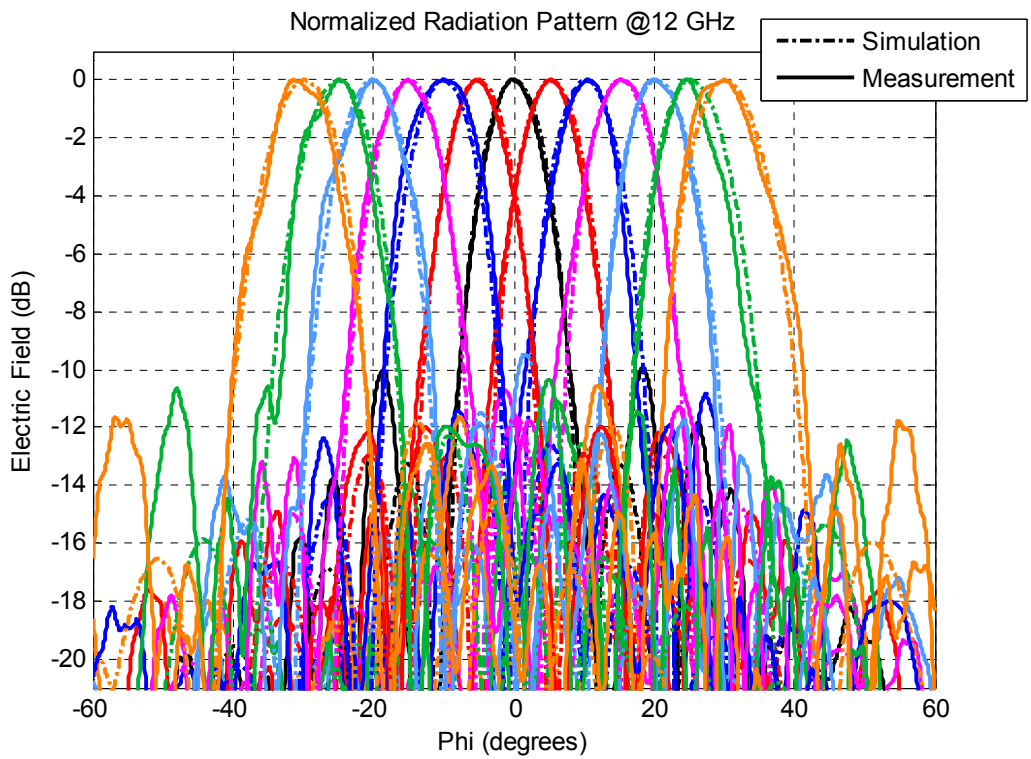


Figure 5 - 25: Measured Radiation Patterns for all Beam Ports at 12 GHz

The plot of the simulated and measured radiation patterns is very beneficial to observe the beam scanning characteristics of the lens. However, in order to investigate and compare the patterns in detail, for each beam port; peak angles, 3 dB beamwidths and levels of the first sidelobes are calculated and tabulated at Table 5 - 4, Table 5 - 5 and Table 5 - 6, respectively. For all of the tables, the presented results at the simulation column are calculated from the multiplication of the array factor calculated using the network analyzer measurements and the simulated pattern of the antenna array. Then, only the non-ideal effects of the connection between lens and antenna and the effects due to the production of the antenna are excluded in the simulation results. Hence, the difference between the simulation and measurement results is due to the non-ideal connection effects and the non-idealities in antenna production. When the results are compared, the maximum difference between the

peak angles of the measurement and simulation results is 0.7° . Also, the maximum difference between the beamwidths is 1.7° . Besides, when sidelobe levels are assessed, it is observed that the measured sidelobe levels are higher than the simulated sidelobe levels, in general. Furthermore, when the tables are studied thoroughly in the symmetry perspective, it is seen that the patterns are not symmetrical for the beam ports corresponding to the angles of equal absolute values. This asymmetry may be caused by the non-idealities in the antenna connector installation and/or the asymmetrical phase and amplitude variations between the phase-matched cables and the attenuators and/or the varying coupling between the array elements due to the non-ideal and non-identical soldering of the connectors.

Table 5 - 4: Peak Angles of the Simulated and Measured Patterns

Scan Angle (degrees) ↓	Peak Angle (degrees)	
	Simulation	Measurement
-30	-29,7	-31,4
-25	-24,9	-24,7
-20	-20,1	-19,9
-15	-14,9	-15,1
-10	-10	-10
-5	-5	-5,2
0	0,1	-0,1
5	5,4	5,2
10	10,3	10,6
15	15,3	15,4
20	20,4	20
25	25,3	24,7
30	30,1	30,2

Table 5 - 5: 3 dB Beamwidths of the Simulated and Measured Patterns

	3 dB Beamwidth (degrees)	
Scan Angle (degrees) ↓	Simulation	Measurement
-30	10,8	9,5
-25	10,4	10
-20	10	9,8
-15	9,7	10
-10	9,5	11,2
-5	9,3	8,7
0	9,2	8,7
5	9,3	8,8
10	9,6	8,6
15	9,6	9,8
20	9,9	9,3
25	10,4	8,7
30	10,9	10,7

Table 5 - 6: First Sidelobe Levels of the Simulated and Measured Patterns

	First Sidelobe Level (dBc) (Normalized to Peak)	
Scan Angle (degrees) ↓	Simulation	Measurement
-30	-11,8	-12,6
-25	-12,3	-10,6
-20	-11,5	-11,9
-15	-11,6	-11,8
-10	-12,6	-12,4
-5	-12,9	-12,0
0	-13,3	-9,9
5	-12,9	-12,0
10	-13,0	-10,8
15	-11,8	-10,7
20	-11,8	-9,5
25	-12,6	-11,1
30	-12,0	-10,5

CHAPTER 6

CONCLUSIONS

This thesis covers the design procedures and implementation of a wideband Rotman lens. First, different beamformer types were investigated and the importance of microwave lens beamformers was emphasized. Then, the Rotman lens concept was introduced together with the historical developments and several application areas. Afterwards, different design approaches were presented and the conventional design approach was chosen. The design procedure was explained step-by-step accompanied with the derivation of the design equations. The design equations for a parallel-plate/waveguide Rotman lens were derived first. Then, the design equations for a microstrip/stripline Rotman lens were obtained. After the derivation of the design equations, design parameters have been investigated in order to see how they affect the lens shape and performance. These parametric analyses were performed in MATLAB[®] [28].

The detailed procedure to implement the microstrip Rotman lens was explained step-by-step. The microstrip Rotman lens operating in 8 GHz – 16 GHz was implemented and the implemented structure was simulated using HFSS[®] [22]. From the simulations, S-parameters of the lens were obtained and the results were presented. Moreover, the implemented lens has been manufactured and the manufactured lens has been measured using a network analyzer. With these measurements, S-parameters of the manufactured lens were acquired and the results

were presented by comparing them with the simulation results. Following the network analyzer measurements, the lens was connected to an antenna array and antenna pattern measurements have been conducted. Finally, with a comparison of all results, the study was concluded.

From the comparison of all results, scanning capabilities and overall performance of the manufactured lens were observed to be consistent with the simulation results. However, when the lens is used to feed an antenna array, it was observed that there were unexpected differences between the simulation and measurement results. Therefore, it was concluded that to be able to use the lens as a beamformer, lens-antenna interactions should be investigated carefully and necessary modifications should be applied to the overall system.

The lens manufactured in this thesis is a microstrip Rotman lens and though the microstrip structure is not used to radiate, there is some leakage radiation from the lens. Hence, this leakage may give rise to unexpected losses. In order to reduce the losses due to the microstrip structure, the lens can be implemented in stripline structure.

In the future, the studies on Rotman lens will be continued to improve the lens performance. As a first step, the lens design is thought to be implemented with stripline technology in order to reduce the losses due to the microstrip structure. In addition, the beam contour shape optimization will be performed.

REFERENCES

- [1] R.C. Hansen, “Phased Array Antennas”, New York: John Wiley and Sons, 1998.
- [2] S.S.D. Jones, H. Gent and A.A.L. Browne, “Improvements in or Relating to Electromagnetic-Wave Lens and Mirror Systems”, British Provisional Patent Specification No. 25926/56, August 1956.
- [3] W. Rotman and R.F. Turner, “Wide-Angle Microwave Lens for Line Source Applications”, IEEE Transactions on Antennas and Propagation, vol. 11, pp. 623-632, Nov. 1963.
- [4] G.L. Leonakis, “Correction to Wide-Angle Microwave Lens for Line Source Applications”, IEEE Transactions on Antennas and Propagation, vol. 36, no. 8, p. 1067, August 1986.
- [5] J. Ruze, “Wide-Angle Metal-Plate Optics”, Proc. IRE, vol. 38, p. 6, January 1950.
- [6] D.H. Archer and M.J. Maybell, “Rotman Lens Development History at Raytheon Electronic Warfare Systems 1967–1995”, Antennas and Propagation Society International Symposium, IEEE, 2005, pp. 31-34, vol. 2B.
- [7] D.H. Archer, R.J. Prickett and C.P. Hartwig, “Multi-Beam Array Antenna”, U.S. Patent 3761936, September 1973.

- [8] K.K. Chan, “A Feed Network for Multibeam Triangular Grid and Hexagonal Shape Planar Array Antennas”, IEEE Transactions on Antennas and Propagation, 1999, pp. 80-83, vol. 1.
- [9] R. P. O. Resource, “<http://www.raytheon.com/>”.
- [10] H. Steyskal, C. Cox and E. Ackerman, “Digital and Optical Beamforming Techniques”, Phased Array Systems and Technology International Symposium, IEEE, 2003, p. 616.
- [11] S. Clark, C. Martin, V. Kolinko, J. Lovberg and P.J. Costianes, “A Real-time Wide Field of View Passive Millimeter-wave Imaging Camera”, Proc. Of the 32nd Applied Imagery Pattern Recognition Workshop (AIPR’03), 2003, pp. 250-254.
- [12] L. Hall, H. Hansen and D. Abbott, “Rotman Lens for mm-Wavelengths”, Proc. SPIE, 2002, vol. 4935, pp. 215-221.
- [13] J. Dong and A.I. Zahghloul, “Extremely High-Frequency Beam Steerable Lens-Fed Antenna for Vehicular Sensor Applications”, IET Microwaves, Antennas & Propagation, 2009.
- [14] J. Toon, “Rotman Lens Offers Inexpensive, Electronically Scanned Antenna”, “<http://gtresearchnews.gatech.edu/reshor/rh-sf96/rotman.htm>”.
- [15] J.P. Shelton, “Focusing Characteristics of Symmetrically Configured Bootlace Lenses”, IEEE Transactions on Antennas and Propagation, 1978, vol. ap-26, no. 4.
- [16] T. Katagi, S. Mano and S.I. Sato, “An Improved Design Method of Rotman Lens Antennas”, IEEE Transactions on Antennas and Propagation, 1984, vol. ap-32, no. 5, pp. 524-527.

- [17] D.R. Gagnon, “Procedure for Correct Refocusing of the Rotman Lens According to Snell’s Law”, IEEE Transactions on Antennas and Propagation, 1989, vol. 37, no. 3, pp. 390-392.
- [18] R.C. Hansen, “Design Trades for Rotman Lenses”, IEEE Transactions on Antennas and Propagation, 1991, vol. 39, no. 4, pp. 464-472.
- [19] J. Kim and F. S. Barnes, “Scaling and Focusing of the Rotman Lens”, Antennas and Propagation Society International Symposium, IEEE, 2001, vol. 2, pp. 773-776.
- [20] Rogers Corporation Advanced Circuit Materials Division, Data Sheet RO1.4000, Revised 2002, Publication #92-004, “RO4000® Series High Frequency Circuit Materials”, [“\[http://www.apcircuits.com/resources/information/ro4000ds_4.pdf\]\(http://www.apcircuits.com/resources/information/ro4000ds_4.pdf\)”](http://www.apcircuits.com/resources/information/ro4000ds_4.pdf).
- [21] L. Hall, H. Hansen and D. Abbott, “Rotman Lens for mm-Wavelengths”, Proc. SPIE, vol. 4935, pp. 215-221, 2002.
- [22] Ansoft HFSS®, “<http://www.ansoft.com/products/hf/hfss/>”.
- [23] L. Musa and M.S. Smith, “Microstrip Port Design and Sidewall Absorption for Printed Rotman Lenses”, IEE Proc., vol. 136, Pt. H., No. 1, pp. 53-58, February 1989.
- [24] E.O. Rausch and A.F. Peterson, “Rotman Lens Design Issues”, Antennas and Propagation Society International Symposium, IEEE, 2005, vol. 2B, pp. 35-38.
- [25] Agilent ADS®, [“<http://www.home.agilent.com/agilent/product.jspx?cc=TR&lc=eng&ckey=1297113&nid=-34346.0.00&id=1297113>”](http://www.home.agilent.com/agilent/product.jspx?cc=TR&lc=eng&ckey=1297113&nid=-34346.0.00&id=1297113).
- [26] E.O. Hammerstad, “Equations for Microstrip Circuit Design”, Proc. European Microwave Conf., 1975, pp. 268-272.

[27] M.V. Schneider, “Microstrip Lines for Microwave Integrated Circuits”, Bell System Technical Journal, vol. 48, 1969, pp. 1422-1444.

[28] Mathworks MATLAB[®], “<http://www.mathworks.com/products/matlab/>”.

APPENDIX A

CALCULATION OF THE EFFECTIVE DIELECTRIC CONSTANT OF A MICROSTRIP TRANSMISSION LINE

In the design of a microstrip/stripline Rotman lenses, effective dielectric constant of transmission lines is needed in order to calculate the contour coordinates. In this appendix, the calculation procedure for the effective dielectric constant will be presented.

By definition [26], the effective dielectric constant, $\epsilon_{r,eff}$ is defined as a ratio of the impedance of the dielectric substrate (Z_0) and the impedance of the microstrip line (Z) as given in (A.1).

$$\epsilon_{r,eff} = \left(\frac{Z_0}{Z} \right)^2 \quad (\text{A.1})$$

Schneider [27] derived a generalized equation (A.2) for $\epsilon_{r,eff}$ where F is a function of the substrate thickness (h) and the transmission line width (w). The parameters are shown in Figure A - 1.

$$\epsilon_{r,eff} = \frac{\epsilon_r + 1}{2} + \frac{\epsilon_r - 1}{2} \times F \left(\frac{w}{h} \right) \quad (\text{A.2})$$

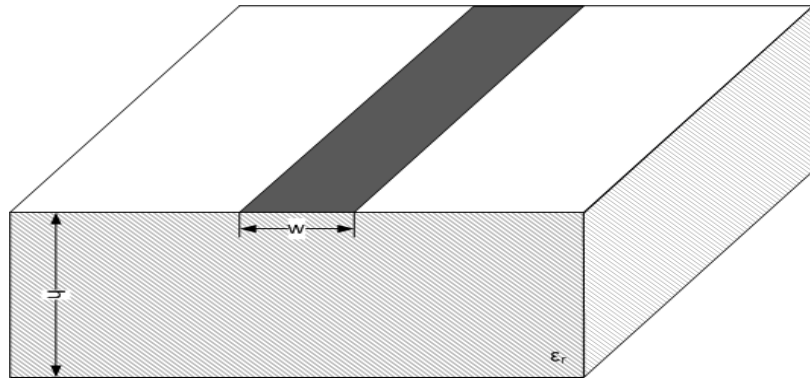


Figure A - 1: Schematic for a Microstrip Transmission Line

Hammerstad [26] derived an expression given in (A.3) for the calculation of F for different conditions of w/h .

$$F = \begin{cases} \left(1 + 12 \times \left(\frac{h}{w}\right)\right)^{-\frac{1}{2}} + 0.04 \times \left(1 - \frac{w}{h}\right)^2 & , \frac{w}{h} \leq 1 \\ \left(1 + 12 \times \left(\frac{h}{w}\right)\right)^{-\frac{1}{2}} & , \frac{w}{h} \geq 1 \end{cases} \quad (\text{A.3})$$

The transmission line width is usually bigger than the substrate thickness. Therefore, in order to calculate the effective dielectric constant, $\epsilon_{r,\text{eff}}$ for $w/h \geq 1$, (A.4) should be used.

$$\epsilon_{r,\text{eff}} = \frac{\epsilon_r + 1}{2} + \frac{\epsilon_r - 1}{2} \times \left(1 + 12 \times \left(\frac{h}{w}\right)\right)^{-\frac{1}{2}} \quad (\text{A.4})$$